Design of the Synthetic Aperture Microwave Imager-2 for measurement of the edge current density on MAST-U

Joe O. Allen

Doctor of Philosophy

University of York
Physics

April 2021

Abstract

The Synthetic Aperture Microwave Imager-2 (SAMI-2) is a 2D Doppler backscattering (DBS) diagnostic designed for multiple high quality simultaneous measurements of the edge pitch angle on the Mega-Ampere Spherical Tokamak Upgrade (MAST-U). The specification, design and testing of the SAMI-2 microwave front end, predominantly antennas and mixer circuitry, are described in this thesis. Dual-polarisation sinuous antennas are designed and shown to fulfil their performance criteria over the 20-40 GHz range. A four-channel microwave in-phase and quadrature (IQ) down-converter is designed to mix the radio frequency (RF) signals from each antenna in the SAMI-2 phased array to a lower frequency, for digitisation. The down-converter is tested and found to achieve its performance specifications over the entire frequency range of the antennas.

The 2D DBS technique was demonstrated by Synthetic Aperture Microwave Imager (SAMI) on the Mega-Ampere Spherical Tokamak (MAST) to measure the edge magnetic pitch angle. A radial profile of the edge pitch angle enables calculation of the edge current density, a difficult quantity to measure, which is valuable for the validation of models and understanding of pedestal dynamics and edge plasma instabilities, e.g. ELMs. In active probing mode, the SAMI-2 diagnostic is designed to make the first measurements of the edge current density by a DBS diagnostic. In passive mode, SAMI-2 will measure Bernstein wave mode conversion, to inform spherical tokamak microwave heating systems.

Contents

List of Figures

Acknowledgments

This thesis would not have been possible without the unwavering support of my family who kept me going, mostly from afar but with bonus parts of a strange year together! (I won't mind if you stop reading here.) I don't know where I would be without the great company of and well targeted encouragement from Caroline, which kept me entertained and motivated.

I am very grateful to my supervisor, Roddy Vann, who has been an invaluable source of energy and ideas, and who together with Simon Bale, Charlie Vincent and myself formed the principle members of the SAMI-2 team. I hope we carry on working together on the diagnostic's exploitation on MAST-U. Many thanks to Phil for some helpful proofreading and for bearing with me! My thanks to all the skilled and knowledgeable technicians in the Physics and Electronics departments at the University of York who helped me with some sticky soldering. I am indebted to EPSRC for funding my generous studentship through the Fusion CDT (if only I'd plowed it all into Bitcoin!). Furthermore, the rapid guarantee of funded extensions to those who needed them was incredibly welcome in those uncertain times. This project was funded through EPSRC grants for studentship, EP/L01663X/1, and SAMI-2, EP/S018867/1. Open source software is a key pillar supporting this work and I would like to thank the developers of Python, KiCad, Overleaf and Inkscape, and many more besides.

I would like to express my profound thanks to the 2016 Fusion CDT intake for the good times shared and those still to be shared, may the carnage continue forever. Hopefully we can showcase sock wrestling at graduation. The staff and students of York Plasma Institute were a constant source of fun and support, thanks for all the great socials and wacky lunch time discussions. I am very appreciative to the Takase-Ejiri group at the University of Tokyo for welcoming and hosting me.

Honourable mentions to my Tang Town housemates keeping it lit and lively, and to Ben Woods for mixtapes and this great thesis template. 2020/1 was both the best and worst time in which to write a thesis - at least it was easier to be a writing recluse because there was no other option.

"How the hell did I *do* that?"

Kilgore Trout, Timequake

Declaration

The work presented in this thesis is original to the best knowledge of the author and has not been submitted anywhere for any other award. All sources are acknowledged as references. Research contained in this thesis has been published in the following journal articles and conference proceedings:

- J.O. Allen, C.H. Vincent, and R.G.L. Vann. "Design of the Synthetic Aperture Microwave Imager Upgrade for measurement of the edge current density on MAST-U". ed. by E. Poli, H. Laqua, and J. Oosterbeek. Vol. 203. EDP Sciences, 2019, p. 03004. DOI: 10.1051/epjconf/201920303004
- J.O. Allen et al. "Dual-polarisation broadband sinuous antenna and microstrip power design for the Synthetic Aperture Microwave Imager-2 diagnostic". *Proceedings of the 14th International Reflectometry Workshop - IRW14* (Ecole Polytechnique Federale de Lausanne). Ed. by G.D. Conway (IPP Garching). Lausanne, Switzerland, 2019. URL: http://www.aug.ipp.mpg.de/IRW/IRW14/proceedings.html

Chapter 1

Introduction and background

1.1 The SAMI-2 diagnostic

The Synthetic Aperture Microwave Imager-2 (SAMI-2) is a second generation diagnostic which exploits the 2D Doppler backscattering (DBS) technique, shown to be feasible by the original SAMI. SAMI made the first microwave measurements of the magnetic pitch angle (described in section 1.11) and obtained the first images of Bernstein wave mode conversion. SAMI-2 is designed from the ground-up to significantly extend these capabilities, primarily by having nearly four times as many antennas as the original. This increase in performance must fit in a similar spatial volume to SAMI and come at minimal additional cost. Consequently, we revamp the design methodology to deliver this improvement.

To write the design specification of this microwave diagnostic, we need to know about spherical tokamaks, the behaviour and uses of microwaves in tokamaks, relevant plasma instabilities, phased arrays and related diagnostic techniques. Then, to design, build and test this diagnostic, we bring together microwave printed circuit board (PCB) design techniques, high frequency simulation efforts, antenna design and experimental techniques. This chapter provides the background describing the components required to develop the SAMI-2 specification.

1.2 Fusion energy

The objective of this thesis is the development of a microwave diagnostic to advance the international fusion programme. Nuclear fusion has the potential to provide a clean and sustainable energy source using widely available fuel found in the Earth's crust and in seawater, with extant supplies for millions of years of global energy production [3]. All countries have access to these fuels, deuterium from seawater and tritium made from lithium, making fusion an equitable energy source. There are two main pathways to achieving a terrestrial fusion reactor: Inertial Confinement Fusion (ICF), where a small fuel pellet is ablatively compressed, most commonly by lasers, to reach conditions where the fuel undergoes fusion on a very rapid timescale; and Magnetic Confinement Fusion (MCF), in which a fusing plasma is confined with magnetic fields and energy may be extracted in a more continuous manner. All the fusion experiments described in this thesis are MCF experiments. Rapid early development of magnetic fusion schemes in the 1950s and 60s understandably led to the expectation of its commercial deployment before the turn of the century. From a technical per-

spective, the turbulent transport in increasingly high performance fusion plasmas is one of the main factors in fusion's continually delayed realisation. The main reason from a non-technical perspective is funding: the cost of fusion experiments has increased with size, which itself has increased to reach greater fusion performance. The two major branches of MCF experiments are toroidal in geometry: the tokamak has an axisymmetric magnetic field, mainly composed of a number of identical coils around the small circumference of the torus, while the poloidal field is largely produced by current driven in the plasma; and the stellarator, which creates poloidal confinement with a more complicated arrangement of coils, negating the need for any, or a substantial, plasma current. Only fusion experiments in tokamaks are considered hereafter.

ITER is a next generation fusion experiment backed by governments representing over half the world's population. It will have approximately eight times the plasma volume of the Joint European Torus (JET), the current world leader in fusion performance which has run shots with $Q \sim 0.7$ [4], where Q is the ratio of fusion power output to power input. ITER aims to sustain plasmas for several minutes at $Q \sim 10$, with the development of these high-performance scenarios beginning in 2035 [5]. In the EUROfusion roadmap [6] to fusion energy ITER will be followed by DEMO, a fusion reactor demonstrating commercial viability. These machines are so called 'conventional' aspect ratio machines. Aspect ratio is the ratio of major radius to minor radius. Spherical Tokamaks (STs), characterised by lower aspect ratios (closer to unity) than conventional tokamaks, have been developed in parallel and potentially offer a more compact, and consequently lower cost, route to the realisation of commercial fusion energy.

1.3 Spherical Tokamaks

The research and development in this thesis is targeted for use on spherical tokamaks, specifically the Mega-Ampere Spherical Tokamak Upgrade (MAST-U) experiment in the UK [7], though it is applicable to conventional aspect ratio tokamaks. Spherical tokamaks are a type of tokamak characterised by a lower aspect ratio. This has the effect of making the cross section more compact and the torus profile more spherical, enabling operation at higher plasma β [8], the ratio of plasma pressure, p, to magnetic pressure

$$\beta = \frac{2\mu_0 p}{B^2}, \tag{1.1}$$

where μ_0 is the permeability of free space. For fusion in tokamaks p is kept high to improve the frequency of fusion reactions, while magnetic field strength, B, is usually kept low, as toroidal magnets usually dominate the cost of a tokamak, making high β operation preferable. The β ratio of a machine can be roughly thought of as its efficiency in converting magnetic energy into plasma thermal energy. Spherical tokamaks have been operated at values of $\beta \geq 30\%$ [9]. Recently, the spherical tokamak has gained popularity as a compact route to commercial fusion energy: see the UKAEA's STEP project [10]. Machine parameters of MAST-U and its predecessor the Mega-Ampere Spherical Tokamak (MAST) are compared in Table 1.1. Following the rough tradition in experimental fusion nomenclature, MAST-U is a mostly new machine rather than a direct upgrade of MAST.

Parameter	MAST	MAST-Upgrade
Major radius [m]	0.85	0.85
Minor radius [m]	0.65	0.65
Plasma current [MA]	1.3	2.0
Core density [m^{-3}]	5×10^{19}	1×10^{20}
Magnetic field at plasma centre [T]	0.52	0.75
Pulse length [s]	0.6	5

Table 1.1: A comparison of machine parameters from MAST [11] and MAST-Upgrade [7].

1.4 The plasma edge and Hmode

SAMI-2 is a diagnostic which, as we will see, probes the tokamak plasma edge. Due to the high temperature required to sustain fusion reactions, tokamaks contain some extreme gradients. The tokamaks in Table 1.1 have poloidal radii on the order of one metre and their plasmas are surrounded effectively by a vacuum. Over this length the temperature falls from approximately ten million kelvin to roughly zero, and the plasma density also drops to zero from $1 \times 10^{20}\,\mathrm{m}^{-3}$ at the centre. Steep gradients such as these are ideal for driving instabilities and turbulence, which degrade performance.

The high-confinement mode (Hmode) of tokamak operation was discovered in the 1980s [12], whereby a transport barrier is formed at the edge upon sufficient heating of the plasma. This improves performance by increasing energy and particle confinement. The central plasma density and temperature profiles are elevated by a steep edge pedestal with a narrow width usually between 1-2 cm [13, 14]. The formation of this transport barrier is considered to be due to poloidal sheared flows in the plasma edge [15, 16]. Transition from the baseline low-confinement mode (Lmode) to Hmode mainly depends upon heating power surpassing a threshold; density must also be above a certain level [15].

The steep edge gradients in Hmode produce a class of instability known as edge-localised modes (ELMs) [17]. In future tokamaks, such as ITER, the energy released by the largest ELMs would melt critical components in the first wall and divertor [18, 19]; therefore, understanding the ELM mechanism is likely to be necessary for the commercial realisation of magnetic fusion energy. The largest ELMs are the result of coupling between a pressure gradient driven mode and an edge current density driven mode, the peeling-ballooning mode [20]. The stability of an H-mode plasma to ELMs is therefore dependent on the edge pressure gradient and the edge current density. A simplified diagram of the stable and unstable regions against the pressure gradient and current density is shown in figure 1.1. The largest ELMs are typically triggered after both quantities build up (solid arrow) and breach the stable region, causing a relaxation in these parameters, shown by the dotted arrow.

High-resolution Thomson scattering is widely used to make measurements of the edge pressure gradient [21–24], while the edge current density is under-diagnosed. It is a difficult measurement to make due to the transient, narrow edge pedestal region in Hmode where ELMs occur. Some diagnostic methods have been employed to measure the edge current density, described in section 1.11.4, but each has its limitations. In the model of the peeling-ballooning mode [25] the edge current density is partly calculated from the edge pressure gradient. To strengthen the understanding of ELM

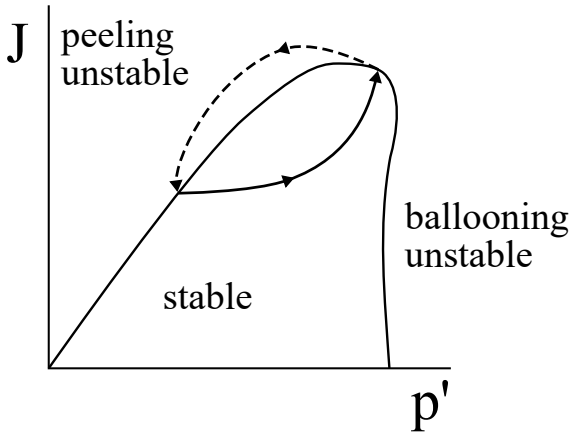

Figure 1.1: Cartoon schematic diagram of peeling and ballooning stability region over edge density gradient-edge current density space. A typical ELM cycle is shown by the arrows.

physics by further constraining the coupled peeling-ballooning model, independent measurements of the edge current density are needed.

1.5 Microwaves in tokamaks

Radiation in the microwave frequency range is used by SAMI-2 to probe the plasma, both actively and passively. Microwaves see many uses in tokamak experiments, from other diagnostics [26] to heating and current drive [27] (including instability control [28]). Tokamak magnetic field profiles generally lead to density cut-offs in the microwave frequency range, allowing probing with microwaves by measurement of reflected beams (reflectometry) and backscattered beams (DBS). Density measurements using interferometry can be performed with a frequency above cut-off. Passive measurement of electron cyclotron emission (ECE), plasma thermal emission, or its harmonics, affords data from which the plasma electron temperature can be calculated. Microwave diagnostic front-ends may be made of the same materials as the vessel wall, making them resistant to neutron damage. Their sensitive electronics may be placed far from the plasma, connected to their launcher via waveguides. These characteristics make microwave diagnostics suitable for use in reactors [29, 30], where they will be able to survive the high neutron flux.

High power microwave beams can be used for heating and current drive through interaction of the wave with the electron cyclotron resonance. Electron cyclotron (EC) waves propagate in vacuum, efficiently couple at the plasma edge and may be transmitted in a narrow beam. As a result, the EC launcher may be situated far from the plasma and is protected. Waveguides used to transmit the beams to the vessel encompass small solid angles and may be made from materials resistant to neutron damage. Beam steering, to alter deposition location, can be achieved using mechanical components far from the plasma and protected from high neutron fluxes. The gyrotron power supplies can also be safely located a long way from the torus. These factors are valuable for heating systems used in future reactors [31]. Neutral beam injection (NBI) for heating and current drive is a good but short term solution to reach a unity Q value. Due to its size, power requirements and need to be located near the vessel, NBI cannot scale to a reactor. Similarly, the long term utility of ion cyclotron resonance heating (ICRH) is limited by its low plasma coupling

efficiency and dependence on large antennas situated close to the plasma (so the waves can tunnel through the vacuum).

1.6 Propagation of electromagnetic waves in a plasma

In order to understand the active and passive microwave signals measured by SAMI-2, we need to understand how they behave in magnetised plasmas. Many waves can exist and propagate in a plasma, with different classifications depending on various conditions such as temperature, density, magnetic field strength and frequency. Those pertinent to this thesis are electromagnetic (EM) waves propagating in a magnetised plasma, for which different subclasses arise depending on the interaction between the background magnetic field and the wave. A summary of these follows, beginning with the derivation of the cold plasma dispersion relation and its form for propagation perpendicular to the magnetic field, before the more broadly applicable case for an arbitrary angle of propagation. For a complete treatment of the physical background, assumptions and mathematical derivations described here, see either of these superlative textbooks [32, 33].

We begin by treating a plasma as a quasi-neutral ionised gas, where ions are assumed to be stationary relative to electrons and the plasma is cold. It turns out that O- and X-mode propagation (away from cut-offs and resonances) are well modelled by the cold plasma dispersion relation. This means that the plasma response to the wave is well described by the conductivity tensor in equation 1.10. The incident wave's wavelength is much smaller than spatial variation of the bulk plasma parameters and its time period is much faster than any temporal variation of those parameters: i.e. the zeroth order quantities are homogeneous and static. Following these assumptions we take Ampère's law,

$$\nabla \times \mathbf{B} = \frac{4\pi \mathbf{J}}{c} + \frac{1}{c}\frac{\partial \mathbf{E}}{\partial t} = \frac{1}{c}\frac{\partial \mathbf{D}}{\partial t} \tag{1.2}$$

and find solutions for the first order quantities of the form $\exp i(\mathbf{k}\cdot\mathbf{r} - \omega t)$, where $\mathbf{k}$ is the EM wavevector. To enable this we find the plasma current density $\mathbf{J}$ in terms of the electric field $\mathbf{E}$, by considering the plasma as a dielectric medium containing current $\mathbf{J}$. We linearise (1.2) (using the exponential form of solutions above) to find an expression for the electric displacement $\mathbf{D}$,

$$\mathbf{D} = \overline{\overline{\epsilon}} \cdot \mathbf{E} = \mathbf{E} + \frac{4\pi i}{\omega}\mathbf{J}, \tag{1.3}$$

where $\overline{\overline{\epsilon}}$ is the dielectric tensor. We then neglect the ion velocity and adopt the cold plasma model, in which the plasma particles all have the same velocity at each point in space, which allows us to write

$$\mathbf{J} = -n_{\mathrm{e}}\mathrm{e}\mathbf{v}_{\mathrm{e}} = \overline{\overline{\sigma}} \cdot \mathbf{E}, \tag{1.4}$$

where n_{e} is the electron number density, e is the absolute value of the electron charge, $\mathbf{v}_{\mathrm{e}}$ is the electron velocity and $\overline{\overline{\sigma}}$ is the conductivity tensor. It is this tensor we seek, to calculate the perturbations in the plasma caused by the EM wave in three dimensions.

In this homogeneous plasma we consider a static, uniform magnetic field oriented along the z-axis (without loss of generality), making $\mathbf{B} = B_0\hat{\mathbf{z}}$, and we aim for plane wave solutions. When making the cold plasma approximation, we assume $k_\perp \rho \ll 1$, that particle gyroradii are much

smaller than the EM wavelength. Taking the Lorentz force equation,

$$m\frac{d\mathbf{v}}{dt} = q(\mathbf{E} + \mathbf{v} \times \mathbf{B}), \tag{1.5}$$

and assuming exponential first order perturbations of the form above, we reach the parallel and perpendicular (in relation to the magnetic field) perturbed velocity components:

$$\tilde{v}_{\parallel} = \tilde{v}_{\mathrm{z}} = \frac{-i\mathrm{e}}{m\omega}\tilde{E}_{\mathrm{z}}, \tag{1.6}$$

$$\tilde{v}_{\perp} = \tilde{v}_{\mathrm{x,y}} = \frac{i\mathrm{e}}{\mathrm{m}\omega}[\tilde{E}_{\mathrm{x,y}} \pm i\frac{\omega_{\mathrm{c}}}{\omega}\tilde{E}_{\mathrm{y,x}}] \Big/ \left(1 - \frac{\omega_{\mathrm{c}}^2}{\omega^2}\right). \tag{1.7}$$

To save ink in further steps we define X to be the dimensionless squared plasma frequency,

$$\omega_{\mathrm{pe}}^2 = \frac{n_{\mathrm{e}}e^2}{\epsilon_0 m_{\mathrm{e}}}, \qquad X = \frac{\omega_{\mathrm{pe}}^2}{\omega^2}, \tag{1.8}$$

which is proportional to density and Y the dimensionless electron cyclotron frequency,

$$\omega_{\mathrm{ce}} = \frac{\mathrm{e}B}{m_{\mathrm{e}}}, \qquad Y = \frac{\omega_{\mathrm{ce}}}{\omega}, \tag{1.9}$$

proportional to the magnetic field, where ω is the frequency of the incident EM wave. Using these shorthand forms and putting (1.6) and (1.7) into (1.4) we find

$$\overline{\overline{\sigma}} = \frac{-i\epsilon_0\omega_{\mathrm{p}}^2}{\omega}\left(\frac{1}{1-Y^2}\right)\begin{bmatrix} 1 & iY & 0 \\ -iY & 1 & 0 \\ 0 & 0 & 1-Y^2 \end{bmatrix}, \tag{1.10}$$

which may then be used to calculate the dielectric tensor. Here we define the refractive index $\mathbf{n} = c\mathbf{k}/\omega$ (the dimensionless wavevector), the magnitude of which is the ratio of the vacuum speed of light to the wave phase velocity. Maxwell's wave equation can then be written as

$$\mathbf{n} \times (\mathbf{n} \times \mathbf{E}) + \overline{\overline{\epsilon}} \cdot \mathbf{E} = 0, \tag{1.11}$$

where $\overline{\overline{\epsilon}} = \epsilon_0\left(\overline{\overline{\mathrm{I}}} + \frac{i}{\omega\epsilon_0}\overline{\overline{\sigma}}\right)$ where $\overline{\overline{\mathrm{I}}}$ is the identity matrix. Upon inserting (1.10) into this relation we can write

$$\overline{\overline{\epsilon}} = \begin{bmatrix} \epsilon_{\perp} & -i\epsilon_{\mathrm{xy}} & 0 \\ i\epsilon_{\mathrm{xy}} & \epsilon_{\perp} & 0 \\ 0 & 0 & \epsilon_{\parallel} \end{bmatrix}, \tag{1.12}$$

where $\epsilon_{\perp} = 1 - \frac{X}{1-Y^2}$, $\epsilon_{\mathrm{xy}} = \frac{XY}{1-Y^2}$ and $\epsilon_{\parallel} = 1 - X$.

As we are interested in the propagation angle relative to the magnetic field direction, labelled θ, we define projections $N_{\parallel} = N\cos\theta$ and $N_{\perp} = N\sin\theta$ and, without loss of generality, align the

wavevector $\mathbf{k}$ in the (x, z) plane. Manipulating (1.11) we find

$$\left\{\mathbf{nn} - n^2\bar{\bar{\mathrm{I}}} + \bar{\bar{\epsilon}}\right\} \cdot \mathbf{E} = \left\{ \begin{pmatrix} n\sin\theta \\ 0 \\ n\cos\theta \end{pmatrix} \begin{pmatrix} n\sin\theta \\ 0 \\ n\cos\theta \end{pmatrix} - n^2\bar{\bar{\mathrm{I}}} + \bar{\bar{\epsilon}} \right\} \cdot \mathbf{E} = 0, \tag{1.13}$$

which combines to become

$$\bar{\bar{\kappa}} \cdot \mathbf{E} = \begin{bmatrix} \epsilon_\perp - n^2\cos^2\theta & -i\epsilon_{\mathrm{xy}} & n^2\sin\theta\cos\theta \\ i\epsilon_{\mathrm{xy}} & \epsilon_\perp - n^2 & 0 \\ n^2\cos\theta\sin\theta & 0 & \epsilon_\parallel - n^2\sin^2\theta \end{bmatrix} \cdot \mathbf{E} = 0. \tag{1.14}$$

Non-trivial solutions are found when $\det\bar{\bar{\kappa}} = 0$ which leads to

$$\begin{aligned} &An^4 - Bn^2 + C = 0, \quad \text{where} \\ &A = \epsilon_\perp \sin^2\theta + \epsilon_\parallel \cos^2\theta \\ &B = (\epsilon_\perp^2 + \epsilon_{\mathrm{xy}}^2)\sin^2\theta + \epsilon_\perp\epsilon_{\mathrm{xy}}(1 + \cos^2\theta) \\ &C = \epsilon_\perp^2 + \epsilon_{\mathrm{xy}}^2. \end{aligned} \tag{1.15}$$

Solving for n^2 we reach

$$n^2 = \frac{B \pm D}{2A} \tag{1.16}$$

where $D^2 = (\epsilon_\perp^2 + \epsilon_{\mathrm{xy}}^2 - \epsilon_\perp\epsilon_\parallel)^2\sin^4\theta + 4\epsilon_\parallel^2\epsilon_{\mathrm{xy}}^2\cos^2\theta$. This result shows that generally there are two different propagating modes with different n values and, consequently, different phase speeds. We will now examine these modes in propagation parallel and perpendicular to the magnetic field, before giving a more general result for propagation at an arbitrary angle.

1.6.1 Parallel propagation

For incident waves travelling parallel to the magnetic field, i.e. $\theta = 0$ in (1.16), we find that the dispersion relation is

$$n_\parallel^2 = 1 - \frac{X}{1 \pm Y}. \tag{1.17}$$

To analyse the behaviour of these modes we look at limits of n^2. When $n^2 \to \infty$ $\lambda \to 0$, as $\mathbf{n} = c\mathbf{k}/\omega$, corresponding to a resonance at which the wave energy is absorbed by the plasma which occurs at the cyclotron frequency $\omega = \omega_{\mathrm{c}}$. Conversely, if $n^2 \to 0$ this occurs when $\lambda \to \infty$, meaning that the wave is reflected at this cut-off location. Solving to find these cut-off frequencies gives $\omega_{1,2} = \pm\omega_{\mathrm{c}}/2 + \sqrt{\omega_{\mathrm{c}}^2/4 + \omega_{\mathrm{p}}^2}$, the upper and lower density cut-offs. These two modes are right and left circularly polarised waves, named the R and L modes. Finally, if $n^2 < 0$ this denotes an evanescent region in which the modes cannot freely propagate, but may tunnel through in certain circumstances.

1.6.2 Perpendicular propagation

To ascertain the two dispersion relations for waves propagating perpendicular to the magnetic field we set $\theta = \pi/2$ in (1.16) and reach the O- and X-mode dispersion relations for the positive and

negative solutions, respectively:

$$n_\perp^2 = 1 - X \tag{1.18}$$

$$n_\perp^2 = \frac{(\omega^2 - \omega_1^2)(\omega^2 - \omega_2^2)}{\omega^4 - \omega^2(\omega_c^2 + \omega_p^2)^{1/2}}. \tag{1.19}$$

The Ordinary mode (O-mode) is linearly polarised with its electric field aligned to the magnetic field direction, meaning it undergoes no interaction with the B-field (in this cold plasma approximation) and behaves the same as it would in an unmagnetised plasma. This mode has the same behaviour as waves propagating in the parallel direction with no external magnetic field, i.e. when $Y \to 0$, leading to one cut-off at the plasma frequency. The eXtraordinary mode (X-mode) is elliptically polarised with $\mathbf{E} \perp \mathbf{B}_0$ and a component of the E-field parallel to the wavevector $\mathbf{k}$, making it partly transverse and partly longitudinal. X-mode waves have the same cut-offs as R and L waves, at $\omega_{1,2}$, and a resonance at $\omega = \omega_{UH} = (\omega_c^2 + \omega_p^2)^{1/2}$, known as the upper hybrid frequency.

1.6.3 Arbitrary angle of propagation

More generally electromagnetic waves will travel at some angle relative to the magnetic field, with a dispersion relation known as the Appleton-Hartree relation [32, 34]. To reach this result, (1.16) is expanded to

$$n^2 = 1 - \frac{2(A - B + C)}{2A - B \pm D} \tag{1.20}$$

and the verbose expressions for A, B, C and D substituted in, which can be simplified to

$$n^2 = 1 - \frac{2X(1 - X)}{2(1 - X) - Y^2 \sin^2\theta \pm \Delta} \tag{1.21}$$

where

$$\Delta = \sqrt{Y^4 \sin^4\theta + 4(1 - X)^2 Y^2 \cos^2\theta}.$$

As the angle of propagation varies, the mode of the wave continuously changes. An initially pure O-mode beam changes continuously to L-wave as its angle, relative to the magnetic field, moves from perpendicular to parallel. Similarly, X-mode can continuously morph into an R-wave, and vice versa.

1.6.4 Waves in a hot plasma

So far we have only considered EM waves in a cold plasma, with no distribution of particle velocity about the averaged velocity. Now we will briefly discuss the consequences of introducing a distribution of particle velocities, making the plasma "hot". For the mathematical derivation of the electron Bernstein wave (EBW) dispersion relation, see [33, 35] which are verbally summarised here.

When a wave approaches a cut-off its refractive index goes to zero, meaning its wavelength is no longer negligible relative to plasma parameter scale lengths. Alternately, when a wave reaches a resonance the refractive index tends to infinity, breaking down the cold plasma approximation when the wavelength becomes smaller than the electron gyroradius. Therefore, in the hot plasma approximation electrons have finite gyroradii. This introduces temperature and the wave vector

as new variables in the dielectric tensor and thus in the solutions of the dispersion relation. As a result, electrostatic modes are found in these new solutions, named after Ira Bernstein, the author of the formative paper on their theory [36].

EBWs are longitudinal waves formed by periodic grouping of charge due to electron gyration, with wavelengths on the order of four times the electron gyroradius. Perpendicularly propagating EBWs are heavily damped near each electron cyclotron harmonic and do not experience a cut-off density limit, meaning they can propagate into regions of arbitrarily high density. At the upper hybrid resonance the EBW mode converts into an X-wave with longitudinal polarisation, which transfers toward transverse polarisation as the X-wave moves away from the UHR.

The EBW dispersion relation is decoupled from that of the previously discussed X-mode in the hot plasma dispersion relation by assuming a short wavelength or large electron gyroradius. In the reverse process the X-wave's phase velocity drops to around the plasma thermal velocity, reducing its wavelength to the order of the electron gyroradius which excites an EBW.

1.7 Edge turbulence

This section seeks to explain why radiation in the microwave frequency range is well suited to diagnosing the edge region of tokamak plasmas. Turbulence in the tokamak edge exists over a broad correlation length scale of roughly 1-100 mm perpendicular to the magnetic field direction [37], corresponding to microwave wavelengths between 3-300 GHz. Turbulent perturbations extend for many metres in the direction of the magnetic field making the turbulence approximately two-dimensional. There are a variety of unstable modes which form in toroidal plasmas which are driven by density and temperature gradients to produce broadband turbulence [38]. The kinetic energy of two-dimensional turbulence is constrained and undergoes bidirectional energy transfer over the wavenumber k range. This results in a power spectra [39] where the turbulence amplitude decreases with increasing wavenumber as a power law [40].

The main instabilities which drive turbulence are the Ion Temperature Gradient (ITG) and Trapped Electron Mode (TEM)[1]. Both of these modes extend over lengths of the order of the ion Larmor radius, ρ_i, which is usually between 1-10 mm [41] and was around 5 mm in the MAST edge [42]. The electron gyroradius is much smaller than the microwave wavelengths of interest here, those used by backscattering diagnostics, so the instability they produce, the electron-temperature gradient mode, is ignored.

Internal transport barriers often form in spherical tokamak plasmas and suppress low-k turbulence, with longer length scales around $k_\perp \rho_\mathrm{i} \leq 1$ [43]. Scattering diagnostics are employed to measure turbulent variations on shorter length scales, $k_\perp \rho_\mathrm{i} \sim 10$ [44]. DBS has been used to measure the turbulence scales between these extrema, depending on the plasma scenario this middling range of turbulence can be the dominant factor in transport [42]. Backscattering efficiency scales with k^{-2} [45], so probing signal wavelengths are chosen to maximise this efficiency.

[1]Not to be confused with Transverse Electro-Magnetic (TEM) modes mentioned in chapter 3.

1.8 Plasma microwave emission

SAMI-2 is able to operate passively, measuring microwaves emitted spontaneously from the plasma. High β plasmas in spherical tokamaks restrict plasma thermal emission from lower electron cyclotron harmonics due to their high density and relatively low magnetic field. High plasma density means that the plasma frequency ω_{pe}, (1.8), is large relative to the electron cyclotron frequency ω_{ce}, (1.9), across the bulk of the plasma (only the electron plasma frequency is of interest here as the ion plasma frequency is roughly two orders of magnitude lower). Consequently, any electron cyclotron emission produced in the plasma is absorbed at the plasma frequency cut-off and cannot be observed directly without. The first five electron cyclotron harmonics were cut off in this way on MAST [46] and on NSTX [47]. Conveniently, an alternative can be found in EBWs, which are thermally born quasi-electrostatic waves [36]. While EBWs cannot propagate in free space, they can undergo mode conversion to EM waves which can then be detected outside the plasma. The B-X-O double mode conversion pathway is most commonly considered, whereby the Bernstein wave converts to X-mode at the upper-hybrid resonance (UHR) layer, before converting to O-mode at the plasma density cut-off [48]. This O-mode wave can then escape the plasma.

EBWs can be excited in the plasma via the reverse process, and the conversion efficiency can be close to 100% depending on certain parameters. The mode conversion process in influenced by the incident angle of the O-mode beam, for which there is an optimal value for conversion to X-mode [49]. At other angles a proportion of the power may tunnel through the resulting evanescent region, depending on the region's width relative to the wavelength and the density gradient.

In its passive operating mode, SAMI-2 will measure the location and angle of spontaneous O-mode emission due to B-X-O mode conversion in the plasma. EBWs are created at cyclotron harmonics and are characterised by the toroidal pitch angle and plasma temperature at that particular point on the harmonic surface. Plasma temperature at the birth location of an EBW is convolved with the mode conversion efficiency in producing the escaping O-wave.

As a result there are three unknowns: pitch angle and temperature at the birth location and the mode conversion efficiency. By ray-tracing back along the path of the measured O-wave we can find the birth temperature from another diagnostic, for example Thomson Scattering. However, the pitch angle and mode conversion efficiency are still intertwined. An approach could be to first measure the pitch angle at the cyclotron harmonic using SAMI-2's active probing, then switch the diagnostic to passive operation to measure the mode converted O-mode emission. This could be done over multiple shots with matching plasma parameters, or within the same shot if SAMI-2 can switch between its acquisition modes on a fast enough timescale.

EBW may be the only viable microwave heating and current drive (H&CD) method for a ST reactor, given that the electron cyclotron harmonics used in conventional aspect ratio devices are unsuitable for H&CD. An EBW H&CD system produces heating and drives current at a similar or even greater level to an equivalent ECRH system [35, 50].

EBWs have been deployed for H&CD on several experiments, including COMPASS-D [51], the WEGA stellarator [52] and QUEST [53]. In addition, EBW assisted plasma start-up has been performed on MAST [54]. A 2 MW EBW system is being designed for Stage-2 of the MAST-U experimental plan.

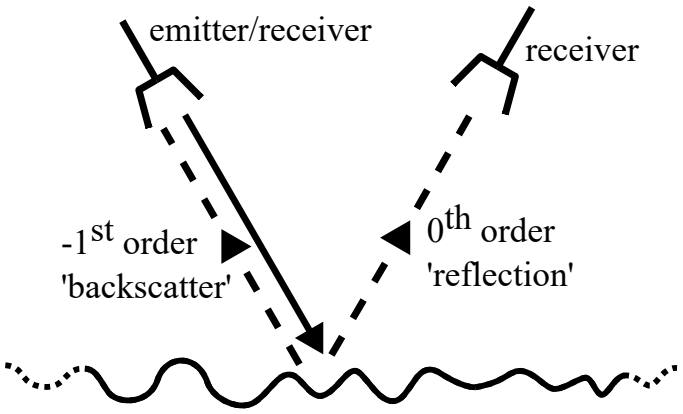

Figure 1.2: Cartoon diagram of the antenna set up for both reflectometry and DBS experiments. In both cases the left hand antenna emits a beam at an angle towards the plasma edge, the plasma surface and its density fluctuations are represented by the wiggly line. For reflectometry a receiving antenna is oriented to receive the zeroth order reflection. For DBS a receiving antenna is positioned close to the emitter to receive the $(-)1^{st}$ reflection - when the beam backscatters.

1.9 Microwave diagnostic techniques

Here we discuss some tokamak microwave diagnostic techniques and implementations relevant to SAMI-2.

1.9.1 Reflectometry

Reflectometry is a radar method which is widely deployed in tokamak research for calculating the electron density, by measuring a beam reflected at the plasma density cut-off. For a detailed review of reflectometry theory, analysis, implementation and key results, see [29]. Figure 1.2 shows the diagrammatic set up of a reflectometry experiment: the left hand antenna emits a beam at an angle to the plasma density cut-off, a second antenna (right) is placed to receive the zeroth order reflection back from the cut-off. The electron density at the cut-off is then inferred from the phase delay of the reflected wave. Turbulent density fluctuations are another key measurement that can be made with reflectometry. The spectrum of the reflected wave is broadened by the presence of turbulence close to the cut-off location, the power spectrum of the resulting phase fluctuations in the reflected beam provides information about the local density fluctuations [55].

1.9.1.1 State of the art reflectometry diagnostics

The Microwave Imaging Reflectometry (MIR) diagnostic employed on the DIII-D tokamak has 12 poloidal channels and four radial channels, using four simultaneous probing frequencies, independently tuneable between 56-74 GHz [56]. This system makes unmatched electron density measurements and can image magnetohydrodynamic modes and turbulence in two-dimensions, measuring characteristics such as poloidal and radial correlation lengths and rotation velocity. Focusing lenses are used to ensure optimal coupling of the probing beam to the plasma. Received signals are focused onto a curved detector array, designed to compensate for the spherical aberration between

central and edge detector channels, as well as the curvature of the cut-off surface. Future upgrades to the MIR system will include an increase up to between 8-16 simultaneous frequency channels and removal of the large aperture lenses, when they are replaced by digital beam forming. A dual-frequency, 16-channel MIR diagnostic based on the same methodology is in use on KSTAR [57].

1.9.2 Doppler backscattering

DBS is used on many tokamaks to record characteristics such as plasma density and turbulent structure velocity [42], turbulence amplitude [58] and of geodesic acoustic modes [59, 60]. DBS diagnostics launch a beam at an oblique angle to the normal incidence cut-off surface and perpendicular to the magnetic field. Probing beam wavenumber k decreases as the beam propagates into regions of higher density while the E-field of the beam increases, localising the scattering region to the location with minimum k [61, 62]. Corrugations on the plasma surface, formed by turbulent structures, scatter the incident beam according to the Bragg condition,

$$\mathbf{k}_\perp = 2\mathbf{k}_\mathrm{i} \sin\theta_\mathrm{s}, \tag{1.22}$$

where $\mathbf{k}_\perp$ is the wavenumber of the turbulent corrugations at the cut-off, $\mathbf{k}_\mathrm{i}$ is the wavenumber of the incident beam and θ_s is the scattering angle - the angle of the incident beam relative to the normal of the plasma surface [63]. The -1^{st} order scattering returns at $\theta_\mathrm{s} = 180°$, or backscatters, along the incident path when the Bragg condition matches $k_\perp = -2k_\mathrm{i}$.

The velocity of the corrugated surface structures can be ascertained from the Doppler shift of the reflected beam $\Delta\omega$ [42], given by,

$$\Delta\omega = 2\mathbf{v}_\perp \cdot \mathbf{k}_\mathrm{i} \sin\theta_\mathrm{s}, \tag{1.23}$$

where $\mathbf{v}_\perp$ is the velocity of the turbulence perpendicular to the normal of the density surface (also the toroidal magnetic field). This velocity is typically dominated by the $E \times B$ velocity [58], from which the radial electric field may be found [64]. DBS experiments mechanically steer the receiving antenna between shots to measure the $\mathbf{k}_\perp$ spectrum and the spatial profile of turbulence velocity.

1.10 Phased arrays

SAMI-2 measures the plasma using a phased array. Phased arrays are found in areas such as military radar [65], for example in fighter jet radar; astrophysics, where arrays of telescopes act effectively as one giant telescope, such as the Square Kilometre Array [66]; and medical imaging, for therapeutic and diagnostic purposes [67].

Phased arrays are made up of a known distribution of antennas on a plane and are digitally focused on arbitrary points in the far-field by phase-shifting the recorded antenna signals, to account for the difference in path traversed by the radiation. Consider a single pair of antennas, a baseline as shown in figure 1.3, of separation d. EM radiation incident on the array from the far field travels slightly different distances to each antenna. For far-field radiation from an angle θ the path difference between the two antennas is

$$\frac{2\pi}{\lambda} d \sin\theta, \tag{1.24}$$

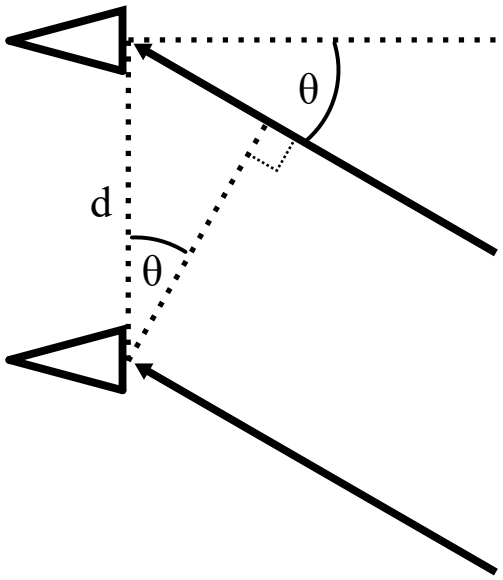

Figure 1.3: A pair of antennas forming a single baseline receiving parallel wavefronts of rays from the far-field. The angle of incidence θ results in a path difference in the distances travelled by the signals which reach the two antennas, equivalent to a phase difference or time delay. By accounting for this difference the two signals may be constructively interfered and the emission from the θ direction calculated.

corresponding to a time delay, or phase shift between the signals from the two antennas. A range of θ values can be scanned to reconstruct the emission pattern along a line in the far-field. However, in this simplest case with a single baseline the resolution is minimal, and a point source would be viewed as a line of finite width.

Consider an array comprising a number of antenna elements. The number of independent baselines in the array is equal to the number of independent vectors between pairs of antennas,

$$\frac{n(n-1)}{2}, \tag{1.25}$$

where n is the number of antennas. For the maximum array resolution for a given n, each displacement between every antenna pair should be different, as repeated baseline displacement vectors are essentially redundant since they provide the same information.

The baselines from a two-dimensional antenna array can be used to reconstruct a two-dimensional surface radiation pattern. Here we will only consider surfaces located in the far-field, though phased arrays can be used in the near-field region [68, 69]. To focus the array at point (θ, ϕ) on this surface the signal of antenna i is phase shifted by

$$\Delta\Phi_i = \frac{2\pi}{\lambda}|r\hat{\boldsymbol{r}} - \boldsymbol{x}_i|, \tag{1.26}$$

where $\boldsymbol{x}_i$ is the displacement of array element i from the origin. The unit vector $\hat{\boldsymbol{r}}$, from the origin

to the selected focus point r on the imaging surface, is given by

$$\hat{\boldsymbol{r}}(\theta,\phi) = \begin{pmatrix} \cos\phi\ \cos\theta \\ -\cos\phi\ \sin\theta \\ \sin\phi \end{pmatrix}. \tag{1.27}$$

This constructively interferes signals from each pair of antennas to reconstruct the source amplitude at the chosen (θ, ϕ) point. Repeating this process over a range of such points allows reconstruction of the 2D surface being imaged.

1.10.1 Frequency domain aperture synthesis

In the SAMI DBS experiments considered here, only a small portion of the intermediate frequency (IF) spectrum is of interest, rarely more than $\pm 0.2\,\mathrm{MHz}$ about the active probing frequency, ν_{probe}. By considering the antenna signals in the frequency domain, phase shifts can be applied only in this particular range. This significantly reduces the calculation time compared to applying phase shifts in the time domain to the entire IF bandwidth of $\pm 50\,\mathrm{MHz}$.

The complex signal recorded by antenna i is the complex sum of the in-phase and quadrature components, $S_i^{\mathrm{A}} = I_i + \mathrm{j}Q_i$, where $\mathrm{j} = \sqrt{-1}$. Over a time interval Δt this is Fourier transformed to

$$\hat{S}_i^A(\nu) = \int_t^{t+\Delta t} S_i^A(t') e^{2\pi \mathrm{j}\nu t} \mathrm{d}t', \tag{1.28}$$

allowing the application of phase shifts to a specific subset of the IF range. Each antenna's contribution is summed to give the frequency domain synthesised beam signal,

$$\hat{S}^{\mathrm{B}}(\nu,\theta,\phi) = \sum_i^N \mathcal{C}_i \hat{S}_i^{\mathrm{A}}(\Delta\nu) e^{\mathrm{j}\Phi_i(\theta,\phi)}, \tag{1.29}$$

summed over N antennas and frequency range $\Delta\nu$, where $\mathcal{C}_i$ is the complex calibration factor accounting for amplitude and phase imbalances between different antenna channels [70]. Integrating the square modulus of $\hat{S}^{\mathrm{B}}$ over the bandwidth $\Delta\nu$ gives the source intensity in the (θ, ϕ) direction,

$$I(\nu,\theta,\phi) = \int_{\Delta\nu} |S^{\mathrm{B}}(\nu;\theta,\phi)|^2 \mathrm{d}\nu. \tag{1.30}$$

Reconstructing the two-dimensional radiation pattern is then a matter of determining this intensity at each angle, (θ, ϕ), over the array's field-of-view (FOV).

1.11 Two-dimensional Doppler backscattering

Performing DBS with a phased array provides two-dimensional DBS capability, a technique first demonstrated by the SAMI diagnostic on the final MAST campaign [71]. SAMI illuminates the plasma with a broad O- and X-mode beam over a $\pm 40^\circ$ FOV in both the horizontal and vertical directions. An array of eight antennas receives the backscattered signals from the plasma edge cut-off which are IQ downconverted to retain both amplitude and phase - allowing post-processing in all directions at all times. Using the known displacements between the receiver array elements, each

pair of signals is constructively interfered by applying the phase difference from (1.26) to reconstruct the signal received from an arbitrary angle (θ, ϕ) in the far-field using (1.30). This reconstruction is performed over a grid of points on the imaging surface to build a 2D image of the backscattered radiation. For 2D DBS measurements SAMI can perform frequency domain aperture synthesis over a limited bandwidth to improve computational time.

On MAST and the National Spherical Torus eXperiment Upgrade (NSTX-U) SAMI has measured MHD activity, effects of Resonant Magnetic Perturbation (RMP) coils, edge k spectra and the edge magnetic pitch angle [70], all while actively probing the plasma. SAMI can also operate passively and has imaged emission from mode converted Bernstein waves on MAST [72].

1.11.1 Magnetic pitch angle

Transport in tokamak plasmas is relatively very fast parallel to the magnetic field and relatively low perpendicular to the magnetic field. Turbulent perturbations thus form elongated corrugations along field lines which rotate perpendicular to the magnetic field direction. SAMI can measure the Doppler shift of backscattered signals from the entire plasma surface within its FOV and from this data the points of maximum blue-shifted and maximum red-shifted power can be localised. The line connecting these two points is perpendicular to the magnetic field direction at the radial location corresponding to the probing frequency. Thomson scattering [73] is used in conjunction with equilibrium reconstruction (EFIT) [74] to calculate the backscattering radial location. Constraining EFIT in different ways can vary the resulting equilibrium and consequently the backscattering location, which will add to the uncertainty in SAMI's pitch angle measurements.

Figure 1.4 shows the Doppler-shifted power difference snapshot on MAST at 300 ms in L-mode shot 27969 [71]. SAMI's FOV of the plasma on MAST was obscured in the grey shaded region by a poloidal field coil. Here the positions of largest and smallest Doppler-shifted power difference ($P_{\text{blue}} - P_{\text{red}}$) have been connected by the black dashed line. The calculated magnetic pitch angle is perpendicular to this line. Magnetic field lines on the O-mode cut-off surface reconstructed by EFIT are overplotted in grey.

1.11.2 Critical review of SAMI

Here follows a critical appraisal of SAMI design, focusing on what should be changed for SAMI-2. The SAMI array was comprised of eight antennas giving 28 independent baselines, using equation (1.25), which correspond to 28 pixels in Fourier space. A simulated annealing optimisation method was employed to find the optimal arrangement of these eight elements [75]. This optimal set of baselines provides a theoretical array response to a point source with a FWHM of $\pm 10°$ and maximum sidelobes at -7 dB relative to the central lobe [76]. When all system signal losses and noise sources are factored in, this is perhaps close to the worst array response that still allows the diagnostic to make the target measurement. As the number of Fourier pixels scales with n^2, even a modest increase in the number of antennas would provide a good rate of return for the diagnostic's resolution. The resolution has a knock on effect on the averaging window time required to produce a relatively smooth pitch angle measurement. Integration times of around 8 ms were used in SAMI pitch angle calculations (and it was thought to need increasing to 10 ms) [71]. Smoothing times on this order inhibit investigation of scenarios when the magnetic field is evolving more rapidly than

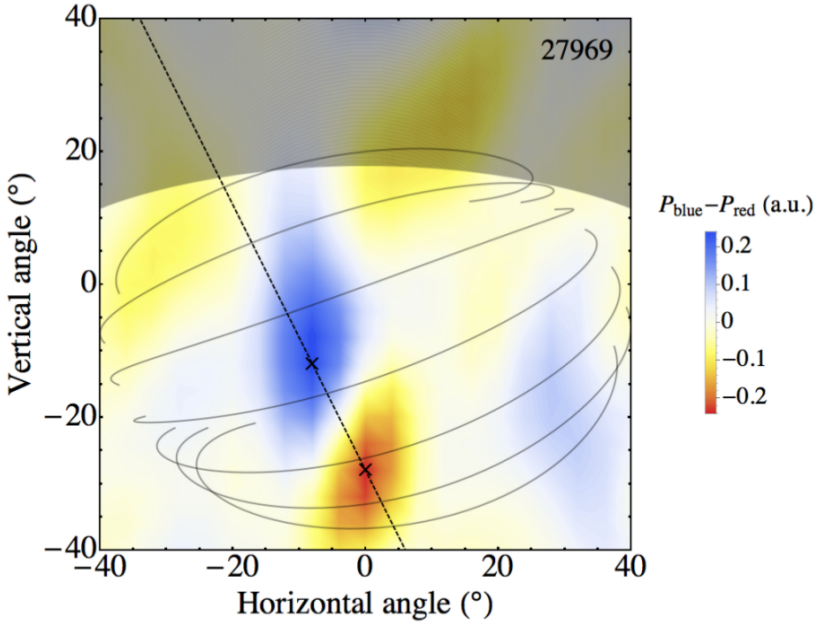

Figure 1.4: An example of the 2D Doppler backscattering image produced from SAMI data on MAST. Difference in Doppler-shifted power received by the array is shown over the FOV of SAMI at 16 GHz during an L-mode shot. The positions of greatest and least difference in Doppler-shifted power are marked by crosses and connected by the black dashed line - SAMI's calculated magnetic pitch angle is perpendicular to this line. Magnetic field lines calculated from EFIT are overplotted in grey. Reproduced from [71].

the integration window. A target for a production SAMI diagnostic could be to match the minimum 2 ms time resolution of the MAST MSE system [77].

Single polarisation Vivaldi antennas used in the SAMI front-end could not differentiate between signals backscattered at the O- and X-mode cut-offs. Depending on plasma parameters the radial locations of these cut-offs can vary up to a few centimetres in the plasma edge, where there are often steep density gradients, which leads to uncertainty in the location of the calculated pitch angle. In addition, there may be interference between the backscattered waves from the two cut-offs [71]. In addition, the three dimensional shape of the Vivaldi antenna is found to cause non-negligible internal reflections within the array [78]. A dual-polarisation planar sinuous antenna was proposed to solve the O- and X-mode separation and the internal array reflection problems.

Single frequency operation requires frequency sweeps to build up a radial profile, required to measure edge current density J_ϕ (using Ampère's Law). Therefore, acquisition at multiple simultaneous frequencies would allow immediate calculation of J_ϕ. As the number of channels is increased by additional antennas, polarisations and frequencies, the data handling capability must improve accordingly. SAMI used a 14-bit digitisation sample depth and a 250 MSps sample rate [79]. The digitisation sample rate can be reduced, especially when the number of channels is increased. This is because having more channels reduces the phased array's spurious signal level (discussed in section 2.3.1), which allows the sample rate to be decreased while giving a better (or similar) signal-to-noise ratio over a given time window.

1.11.3 Edge current density

The parts of the edge current density derivation by De Bock et al. [80] for the motional Stark effect (MSE) diagnostic pertinent to pitch angle measurements using 2D DBS are included here. The overall pitch angle at a given radial location in the plasma is a ratio of the poloidal B_θ to toroidal magnetic field B_ϕ at that location,

$$\gamma_\mathrm{m} = \arctan\left(\frac{B_\theta}{B_\phi}\right). \tag{1.31}$$

With a radial array of magnetic pitch angle measurements the edge current density J_ϕ can be calculated with Ampére's law in cylindrical coordinates:

$$\mu_0 J_\phi = (\nabla \times \boldsymbol{B})\big|_\phi = \frac{\partial B_\mathrm{R}}{\partial Z} - \frac{\partial B_\mathrm{Z}}{\partial R}, \tag{1.32}$$

where μ_0 is the vacuum permeability. Here the assumption $B_\mathrm{Z} \approx B_\theta$ is made, valid for pitch angle measurements on the midplane, which simplifies the geometry from toroidal to cylindrical. The edge toroidal field B_ϕ can be taken from an initial EFIT solution, as it is only weakly affected by the edge J_ϕ and will be close to the vacuum toroidal field. Using the EFIT B_ϕ value in (1.31) one finds B_Z, which, when calculated at multiple radial locations, facilitates calculation of $\partial B_\mathrm{Z}/\partial R$. As the flux surface shape is weakly dependent on the local J_ϕ in the edge, the ratio $B_\mathrm{R}/B_\mathrm{Z} \approx B_\mathrm{R}^\mathrm{EFIT}/B_\mathrm{Z}^\mathrm{EFIT}$ can be assumed, where variables with an EFIT superscript are taken from the EFIT reconstruction. Differentiating by Z leads to

$$\frac{\partial B_\mathrm{R}}{\partial Z} = \frac{B_\mathrm{Z}}{B_\mathrm{Z}^\mathrm{EFIT}} \frac{\partial B_\mathrm{R}^\mathrm{EFIT}}{\partial Z}, \tag{1.33}$$

giving the remaining term in (1.32), as B_Z has been calculated from the measured pitch angle and all EFIT terms found from the reconstruction. MSE makes measurements along the midplane, whereas SAMI-2's FOV encompasses a large poloidal portion of the low-field-side of the plasma, meaning the assumption leading to (1.33) is not always valid.

SAMI-2 is closest to the outboard midplane, so will preferentially measure pitch angle there, allowing use of this derivation to calculate a first approximation of the edge current density. For a more detailed approach we will run a SAMI-2 constrained EFIT, by fitting the toroidal current density profile to find the best match between SAMI-2's observed predominant backscattering locations and the predicted backscattering locations from EFIT (where the B-field direction is perpendicular to SAMI-2's line of sight).

SAMI's pitch angle data will be compared to MSE and EFIT values. EFIT reconstructions may be constrained in different ways, the MSE-constrained EFIT and SAMI-2-constrained EFIT can be compared to unconstrained EFIT, along with the raw pitch angle measurements.

1.11.4 Edge current density diagnostics

Three diagnostic techniques have been deployed which can measure the tokamak edge current density. By measuring Zeeman splitting along an injected lithium ion beam, the radial profile of the magnetic pitch angle has been measured on DIII-D [81, 82]. This system has 32 lines of sight in the plasma edge, with a spatial resolution of about 5 mm. However, due to the photon collection rate

the data is integrated over around 100 ms which is too long to track the rapid evolution of the edge current density during ELM activity. ELMs are produced on a fast timescale, 100 µs on MAST [83], making intra-ELM measurements very challenging.

MSE diagnostics can measure the magnetic field along a neutral beam path and then calculate the edge current density [80]. Charged atoms moving through a magnetic field induce an electric field which splits the atoms' energy levels, altering the wavelength and polarisation of atomic radiation emitted. By measuring this radiation, the local magnetic field can be retrieved and the edge current density calculated. In the absence of a radial electric field E_r the polarisation of this radiation is proportional to the magnetic pitch angle. The MSE relies on the presence of neutral beams and does not work during ELM activity. These diagnostics typically have numerous lines of sight arranged to cover the entire view from the plasma axis to the edge. As a consequence of its wide FOV the radial resolution is rather coarse, at 2-3 cm, over the pedestal. The MAST density pedestal usually had a width between 1-2 cm. Furthermore, the edge current density profile is peaked within the pedestal, requiring sub-centimetre resolution to resolve its shape. Therefore, MSE edge pitch angle profiles from MAST were fitted with a spline to obtain a smooth profile for the derivative in the current density calculation [80].

Generally, MSE diagnostics have very good time resolution, normally 2 ms on both the MAST [77] and MAST-U systems. The MSE is influenced by the local radial electric field, at the intersection of the line of sight with the neutral beam path, which is strong in the plasma edge and must be corrected for. Beam emission polarimetry has also been used to extend the MSE technique by measuring multiple polarisation angles concurrently, enabling the full MSE spectrum to be recorded simultaneously [84].

Thirdly, reverse imaging of the O-mode cut-off surface has been proposed and a full-wave feasibility study conducted of this "anti"-radar method [85]. This technique would identify the direction at the O-mode cut-off layer at which there is the least reflection of the probing beam, from which the inclination of the magnetic field at the cut-off is calculated. The frequency of the injected beam can be swept to measure the radial profile of the magnetic pitch angle.

1.11.5 SAMI-2 capabilities

Here we summarise the planned and potential capabilities of SAMI-2. Passively acquired SAMI-2 data will be analysed for spontaneous emission due to EBW mode conversion, as discussed in section 1.8, providing location and angle of emission data. These data will inform EBW heating and current drive experiments.

Two-dimensional DBS measurements, as described in section 1.11, afford edge magnetic pitch angle measurements which may be used as an alternative EFIT constraint. Furthermore, as discussed, they will be used to calculate the edge current density, which will be compared to MSE and theoretical results. If SAMI-2's time resolution is fast enough, it may be able to measure pitch angle dynamics before or after ELMs, providing information on ELM evolution.

As SAMI-2 is a broad-beam Doppler backscattering system, it may be able to perform correlation reflectometry to track, for example, density perturbations across its FOV. This would enable calculation of the local radial electric field experienced by these structures and could be compared to existing 1D spatial DBS measurements [42]. Finally, it may be possible to measure the extent

to which turbulence at the cut-off is electromagnetic (when electrostatic turbulence is modified by magnetic fluctuations [86]), by analysing the change in polarisation of the backscattered active probing beam.

1.12 Outline and scope of thesis

The goal of this thesis is to describe the design process of a high performance microwave tokamak diagnostic, SAMI-2, using 2D DBS to measure the edge current density on MAST-U. It is particularly focused on the design and testing of the radio frequency (RF) front-end of this diagnostic, which is guided by interplay between experimental and simulation efforts. Summaries of the forthcoming chapters are as follows:

- In chapter 2, we distill the SAMI-2 design process into a qualitative multi-dimensional optimisation problem, evolving from constraints between its subsystems as well as external constraints. This analysis results in some decisions with discrete solutions, which we make directly, and nudges to other more continuous decisions to be made after further research.

- The printed circuit board design methodology we use in this thesis is described in chapter 3. Following this are overviews of the sinuous antenna designs, Vivaldi antenna designs and applied experimental and computational methods.

- We present the design, simulation and experimental results of dual-polarisation sinuous antennas operating from 20-40 GHz in chapter 4, accompanied by Vivaldi antennas operating in the same frequency range. These are the two candidates for the SAMI-2 phased array.

- Chapter 5 describes the microwave PCB design, simulation and testing of the SAMI-2 front end electronics. These front end electronics are made up of a four-channel down-conversion mixer PCB attached directly behind each antenna and the reverse PCB, an up-converter, used to produce the active probing signals. Included in this chapter are results from simulations and experimental testing of several 2.92 mm, 40 GHz PCB connectors, for connecting the SAMI-2 array's antennas to these mixer PCBs. In addition, we present results for a 10 GHz local oscillator (LO) connector.

- Our concluding remarks on the design, implementation and testing of the antennas and PCBs for the SAMI-2 RF front-end are made in chapter 6. In addition, we describe the SAMI-2 mechanical design and its planned installation on the MAST-U vessel. Furthermore, we make suggestions for further work, initially in the testing and deployment of SAMI-2, then predominantly in its exploitation on MAST-U.

- SAMI-2 was designed by a small team of people with regular progress discussions and collaborative efforts for much of the design, manufacture and testing of the diagnostic. The author took the lead on all parts of the design of the antenna and mixer subsystems, all of the antenna testing effort and played a large part in the mixer and LO verification experiments.

Chapter 2

High level design of SAMI-2

2.1 Defining the problem is a component of the research

A substantial part of the work in this thesis has been deciding and constraining the problem, the specification of the Synthetic Aperture Microwave Imager-2 (SAMI-2) system. In this chapter, we aim to define the parameters of the problem sufficiently precisely so that, upon completion, we may decide how well we have succeeded. The design requires detailed proactive planning to identify critical issues so they may be mitigated against. The two main physics goals for the diagnostic on the Mega-Ampere Spherical Tokamak Upgrade (MAST-U) are measurement of magnetic pitch angle at two simultaneous radial locations and imaging of electron Bernstein wave (EBW) mode conversion. These goals dictate key aspects of the diagnostic design, here the capability to actively probe at two frequencies simultaneously and operate in a passive mode, respectively. In addition, there are auxiliary requirements such as dynamic range, sample rate and signal-to-noise ratio.

With hindsight, we now appreciate that eight antennas on SAMI was only ever sufficient for a proof-of-principle device. Therefore, we know that SAMI-2 requires significantly more than this number of antennas to be a production level diagnostic. This necessitates is a step change in the design methodology, as SAMI-2's performance must be much greater than the original's, without causing major increases in spatial volume or cost.

We describe the diagnostic in high level blocks, or subsystems, and list the key constraints affecting each block. These four constraints are then elaborated and applied across each subsystem. Following this, we describe baseline and maximum cases for each subsystem. Finally, we explain the main interrelations between constraints, before concluding with some resulting important binary decisions and less definite nudges to subsystem specifications.

2.1.1 Block system description

SAMI-2 is divided into two major sections, the dividing line being the frequency range of the signals processed: the front end signal collection, radio frequency (RF) operating frequency in tens of GHz, and the back end digitisation and data processing, carrying the intermediate frequency (IF) frequency in tens of MHz. Both sections are comprised of a number of interconnected blocks which are described here and shown in figure 2.1. They are referred to interchangeably as "blocks" and "subsystems".

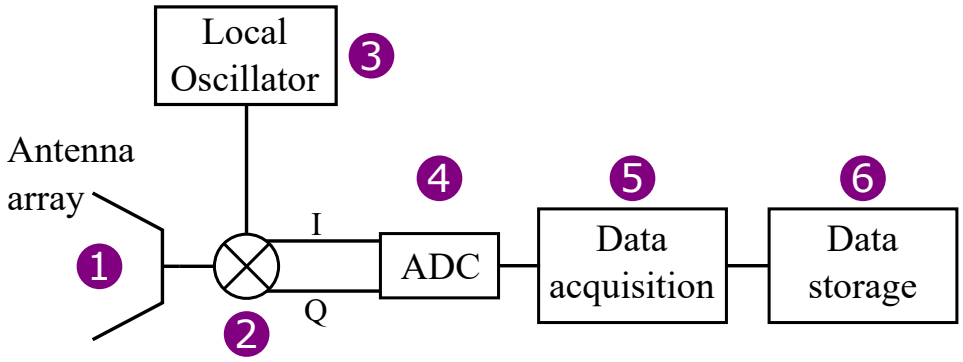

Figure 2.1: High-level block diagram showing the main system blocks required for a 2D Doppler backscattering (DBS) diagnostic. Only one antenna polarisation and frequency signal path is included for brevity: each antenna is dual-polarisation and both polarisations are mixed with two local oscillator (LO) frequencies (3). An In-phase and quadrature (IQ) mixer is labelled (2) and the analogue to digital converter (ADC) conversion stage labelled (4). This feeds digitised data into the acquisition module (5) to be packaged and stored in (6).

A 2D DBS diagnostic needs multiple antennas in its array (block 1) to measure the backscattered radiation and the plasma's passive thermal emission and a smaller number to launch the active probing signal at the plasma. Block 2 has a dual function both to produce the active probing signal for the launching antennas and to mix down (downconvert) the signals from the receiving antennas. The downconverters in block 2 must be IQ mixers so that phase information is acquired, enabling separation of the two sidebands. This mixing stage forms the separation between the front and back ends, where GHz signals (referred to as the RF) are mixed down to MHz signals (referred to as the IF). These IF signals can be transmitted over tens of metres without significant losses compared to only tens of millimetres for GHz signals, although here the IF only travels tens of centimetres as the diagnostic operates in a noisy environment. The reference signal for this mixing is provided by block 3, the LO. Block 4 is an ADC which digitises the analogue IF signals. These digital signals are processed by the data acquisition subsystem, block 5, before being stored in block 6.

2.1.2 Project constraints

There are four main constraints affecting each subsystem block, both externally and in the relationship between each block:

- performance, ability (a)
- spatial volume, bulk (b)
- cost (c)
- deliverability (d).

Every block has a desired performance (a) for all its attributes which were decided using the original SAMI diagnostic as a proof-of-principle baseline upon which to design this production version. Sector 5 of the tokamak area of MAST-U containing the port window allocated to SAMI-2 contains other diagnostics and hardware, imposing a constraint on the spatial volume (b) available for SAMI-2. The budget limit (c) is set mainly by the EPSRC grant EP/S018867/1 awarded to the SAMI-2

project in October 2018, as well as other consumables budgets. Deliverability (d) is an umbrella term comprising the time-sensitive project constraints including complexity, risk and component availability, all of which potentially impact the likelihood that SAMI-2 will be ready for the start of the first MAST-U campaign.

As the design progressed, the performance criteria for each subsystem were updated and the resulting impact on the volume, cost and deliverability ascertained, and vice versa.

A cost function can be constructed, containing the contributions from each subsystem, which describes the impact on the overall system's performance caused by downgrading the performance of a subsystem's attribute from the ideal level and the interplay with both the objectives for other blocks and constraints (b), (c) and (d).

2.2 Application of constraints

Each specification of the system has a baseline performance, that of the original SAMI. While SAMI was successful in proving phased array imaging and 2D DBS work on spherical tokamaks, most aspects of the system should be improved or changed for a production diagnostic. The corresponding maximum desired performance of each system specification is described in section 2.2.1. Applying the four constraints above to each specification may put upward or downward pressure on its performance level, and may also impact the characteristics of other subsystems due to the interfaces with them. Through following all the interrelations between subsystem blocks an overall picture is formed to highlight the areas suffering the greatest pressure and requiring the most consideration. These interrelations impact high-level decisions such as:

- Choice of antenna
- Off-the-shelf connectorised components or printed circuit boards (PCBs) vs designing custom PCBs
- Reconciling desired RF frequency range with achievable range of available components
- ADC speed, which dictates IF bandwidth and data bandwidth
- Local oscillator frequency range
- Digitisation system's capability (impacts number of channels per ADC/FPGA)

A system constraint diagram is shown in figure 2.2 displaying external factors imposing constraints on the various blocks as well as the impact certain subsystem's characteristics, desired or unavoidable, have on the other subsystems. The aim is to increase performance and deliverability as much as possible while reducing or limiting the volume and cost. In the following four subsections the constraints in figure 2.2 are explained before they are applied to each subsystem. We relate these constraints together and partly prioritise them in section 2.6, before we make decisions resulting from them in section 2.7. We make these comparisons quantitatively where possible, and discuss others in a qualitative sense.

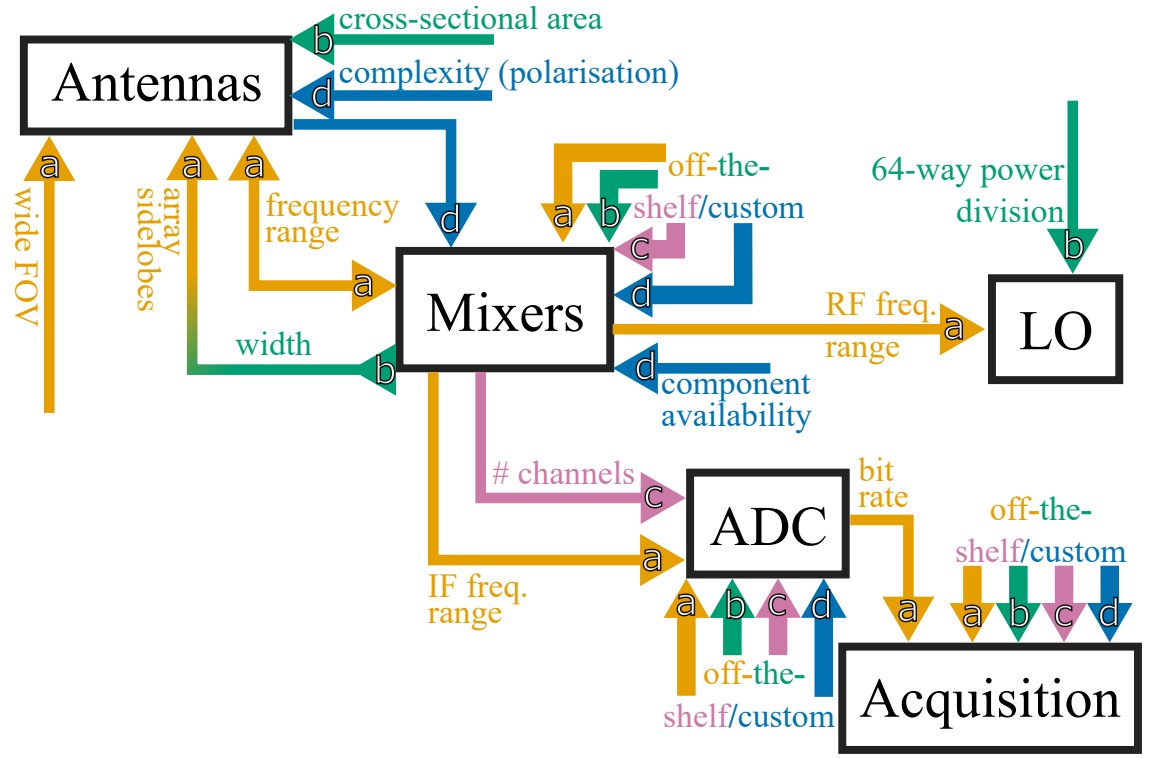

Figure 2.2: An interconnection diagram giving an overview of how the main four constraints manifest externally to affect each block and how they are found to impact interrelations between blocks. These four constraints are performance or ability (a) which dictates the physics that can be measured, spatial volume or bulk (b) which is constricted by that available around the MAST-U vessel, cost (c) limited by the project budget and "deliverability" (d) that comprises time sensitive factors such as risk, design complexity and component availability. Constraints (a) and (d) are ideally increased and (b) and (c) are decreased. The ABCD key at the bottom lists these constraints and shows the limit or target of each constraint.

2.2.1 Performance

This project aims to maximise performance of the diagnostic in terms of measurement of the desired physics. The minimum performance of SAMI-2 is to replicate the capability of the original SAMI with the addition of a second probing frequency to enable measurement of the edge magnetic pitch angle at two simultaneous radial locations, from which the edge current density is calculated.

The antennas need a wide field-of-view with which to see large part of the plasma surface. Their operable frequency range directs the choice of mixer as both frequency ranges should ideally overlap completely. The mixer modules sit directly behind each antenna and consequently the module's width limits how close two antennas can be separated in one axis. The knock on effect of this is a degradation in the array performance, as the shortest array baseline (separation between each pair of antennas) determines the array's field-of-view and sensitivity to large scale structure. The diameter of the vessel vacuum window constrains the array diameter and consequently limits the longest baselines, which dictate the angular resolution of the array.

Performance enters into the choice between custom or off-the-shelf solutions for the mixers, ADCs and acquisition subsystems as the custom option is likely to provide more varying levels of capability which can be selected as desired. The mixer RF frequency range puts a condition on that required for the LO and its IF bandwidth influences the filtering required prior to the ADC stage. In turn, the ADC bit rate sets a goal for the acquisition subsystem's performance.

2.2.2 Spatial volume

A re-entrant window was installed in 2016 on the Sector 5 midplane for SAMI-2, shown in figure 2.3 and the volume from the flange extending back from the vessel allocated for the diagnostic hardware. As a first approximation the available volume can be thought of as a cuboid extending back from the vessel wall about 1.5 m. Ideally all subsystems except the data storage part of the acquisition block would be located in this space directly adjacent to MAST-U. The next nearest available location for hardware is metres away; hence, the RF and IF signals should be limited to travelling short distances within the volume extending back from the port window. As the environment around the vessel will be rather noisy, only once the IF has been digitised should it travel the longer distance to data storage.

The cross sectional area of the antennas implements an upper bound on the number of array elements that will fit into the port window aperture. This may impact the array's performance in the same way as does the width of the mixer modules, mentioned above. The LO subsystem includes 64-way power division which could be the limiting factor on the width or height of the diagnostic box. Custom solutions to the mixer, ADC and acquisition subsystems are likely to offer smaller volumes than their off-the-shelf counterparts.

2.2.3 Cost

The project budget is limited mainly by EPSRC grant number EP/S018867/1, awarded in October 2018, and a few smaller general budgets. Many performance aspects directly link to price of components. Off-the-shelf options are often significantly more expensive than customised subsystems. Custom solutions require a number of prototype stages which may prove costly if the complexity

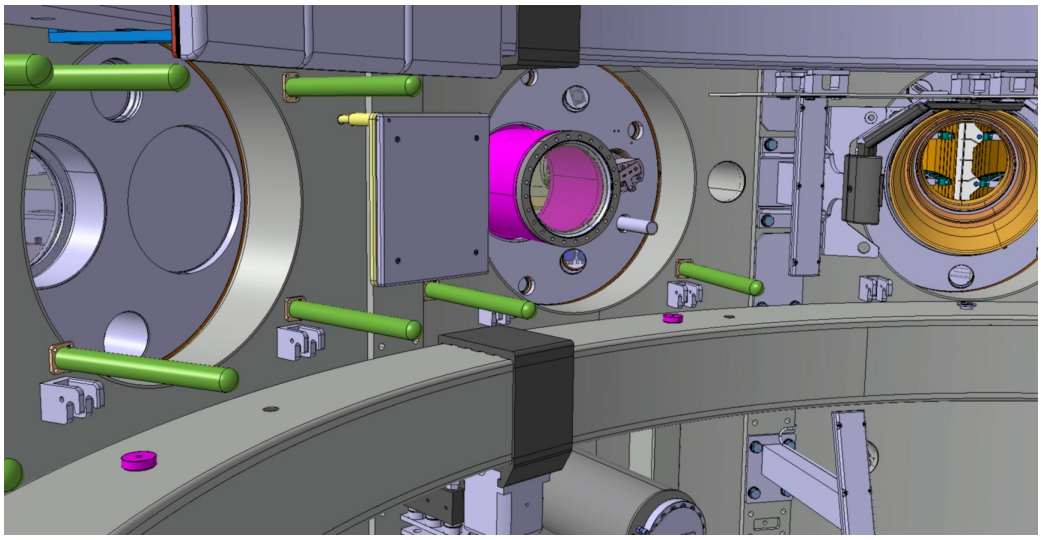

Figure 2.3: In-vessel CAD view of the re-entrant port (pink) installed for SAMI-2 on Sector 5 of MAST-U.

or risk factors are significant. The hardware budget for SAMI-2 is £160 000, versus that of the proof-of-principle SAMI, totalling about £130 000. As is detailed later, compared to the baseline the maximum SAMI-2 performance includes almost a fourfold increase in the number of antennas, each producing four times as many data channels. Using these multipliers as a first estimate SAMI-2 requires 16 times the hardware for under a 25 % increase in budget.

SAMI used off-the-shelf mixers and ADCs, which was feasible for the rapid delivery of a proof-of-principle. However, this would be cost-prohibitive for SAMI-2. This push to custom modules brings with it overheads when costing the system, such as from prototyping stages, navigating the positives and negatives of potential components and the complexity introduced by costs scaling with the number of antennas.

2.2.4 Deliverability

Deliverability encompasses all factors which can impact the successful delivery of SAMI-2 to MAST-U in time for its first campaign. Relevant factors are complexity: a more complex system will be harder to implement than one less intricate; risk: that a given subsystem's design may not work or may fail; component availability: whereby selected parts may be released too late, be out of stock or be under export control; compatibility with fusion experiments: the diagnostic must be suited to its environment in which it will experience conditions including strong magnetic fields, electromagnetic (EM) noise and persistent vibrations; and finally operational difficulty: higher difficulty may delay the diagnostic installation or calibration and increase chance of data collection failure.

Competition in off-the-shelf microwave integrated circuits has been decreasing recently, moving towards fewer, bigger manufacturers. This amplifies supply bottlenecks to the consumer by reducing the number of alternative providers. We compile lists of candidate off-the-shelf components for pivotal parts of the diagnostic

2.3 Subsystem's baseline and maximum cases

A significant part of the project is to identify and tackle difficulties with pivotal subsystem specifications before they delay the critical path of the implementation of SAMI-2. The severity of some risks involved is arguably substantial in this type of project due to the large number of external factors. Subsystems and their shorthand forms follow: the antenna array, α, the mixers, μ, the LO, λ, the ADC, δ and the acquisition subsystem, ρ.

2.3.1 Antennas and array

Minimal and maximal settings for each specification of the antenna and array are listed in Table 2.1. The number one candidate, the sinuous antenna, for these criteria is designed and tested in chapter 4, along with a modified version of the SAMI antenna as a backup option, the antipodal Vivaldi antenna. In the discussion of those results, we will discuss how well both of these antennas fulfill the specifications described in this section.

Antenna specification	SAMI baseline	Optimal
Antenna type	Single polarisation	Dual polarisation
Frequency range [GHz]	10-35.5	15-40
Shape	3-dimensional	Planar
Profile	$\sim$15 mm wide	Similarly small cross-section
Field-of-view (10 dB width)	$\pm 40\,^\circ$	$\pm 40\,^\circ$
Polarisation separation	High	Better than 10 dB
Polarisation wobble	Low	Reproducible
Array specification	**SAMI baseline**	**Optimal**
Number of elements	8	$\geq$30
Side- to main-lobe ratio [dB]	-7	≤ -15
Manufacture	Individual PCBs, repeatable	Array on single PCB

Table 2.1: Antenna and array characteristics for the optimal design of SAMI-2 compared with those used in SAMI, the baseline case.

The optimal frequency range is guided by MAST-U density profiles, which can be converted to linear plasma frequency using (1.8). One such density profile, from an H-mode TRANSP simulation, is shown in figure 2.4 over the normalised minor radius. No simulated L-mode density profiles are currently available, but they will have an overall lower density profile mainly due to a shorter, lower gradient steep edge region. A maximum frequency of 40 GHz enables imaging of a large way up the H-mode pedestal and a minimum frequency of 20 GHz covers most of the edge beneath that. Nonetheless, the optimum minimum frequency is chosen to be 15 GHz, so that the entire pedestal can be imaged. The frequency channels on SAMI below about 15 GHz often produced very noisy data, so for this reason we will not aim to match SAMI's minimum frequency.

The number of array baselines scales quadratically with antenna number, (1.25), so we aim to have as many as possible that will fit in the array while balancing with cost. Sidelobes are artifacts in the image reconstruction (of a point source) due to the finite number of antennas in a phased array. The maximum sidelobe relative to the main lobe at 0 dB for randomly placed arrays of 6-32 antennas are shown in figure 2.5. Several thousand random placements were tested and the lowest

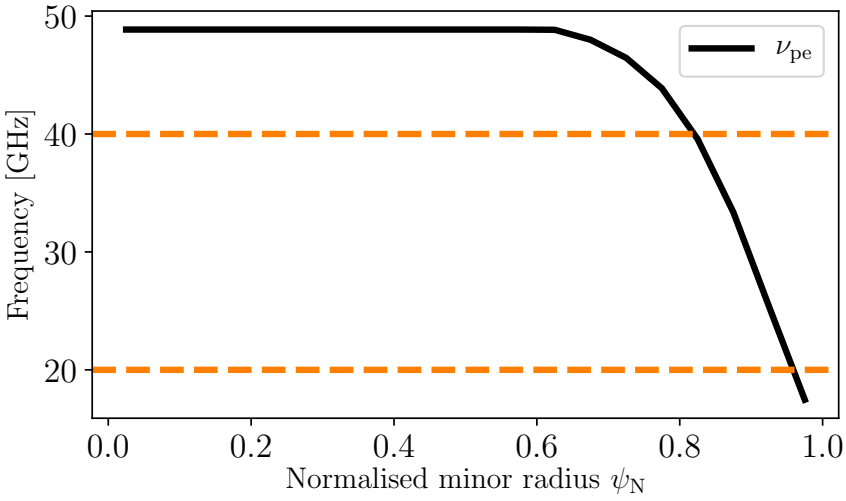

Figure 2.4: MAST-U plasma frequency ν_{pe} (black) over normalised minor radius, density data from H-mode TRANSP simulation K26 for scenario A2. The minimum and maximum frequency of SAMI-2 (as built) are marked by the orange dashed horizontal lines. This shows that the resulting 20-40 GHz range covers a large proportion of the plasma edge.

maximum sidelobe taken for each antenna number. Using these data as a guide we will aim for at least 20 antennas, but preferably more than 26.

The total volume of the array must fit within the re-entrant port, a technical drawing of which is shown in Figure 2.3, which has a window of diameter 160 mm. The cross sectional area of each antenna must be small enough to allow a sufficient number of elements, ideally at least 32 (30 receivers, 2 emitters), to fit into in the array disk diameter 150 mm. SAMI used Vivaldi antennas successfully up to 35.5 GHz; in a mid-performance case this design will be re-purposed for SAMI-2 with the top frequency extended up to 40 GHz. Attempts will be made to design a higher performance antenna operating in dual linear polarisations and with a less 3-dimensional structure than a Vivaldi antenna. In either case the antennas will be manufactured on printed circuit boards (PCBs) and do not threaten to drain the project budget.

Given the prior experience from the SAMI project using Vivaldi antennas, which can be used as a back up for SAMI-2, the deliverability of some form of antenna array is not of paramount concern here. Some work remains to ensure these baseline antennas can operate up to 40 GHz and that two orthogonal Vivaldis can be placed sufficiently close to be an acceptable substitute for a co-located dual-polarisation antenna. In spite of this back up option, the optimum SAMI-2 system would use a compact, 2-dimensional and dual-polarisation alternative, which is yet to be designed. Therefore, the deliverability of the maximum performance SAMI-2 antenna is significantly more challenging than the baseline case.

2.3.2 Mixers

Optimal performance of mixer modules:

- IQ capable

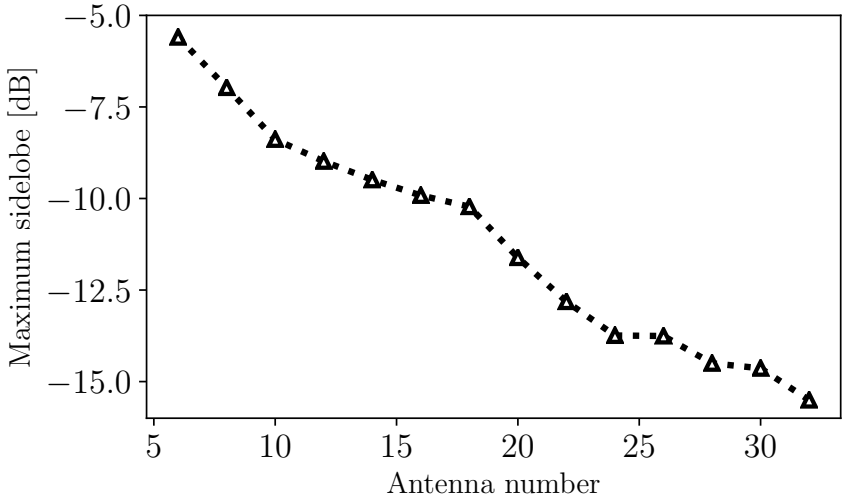

Figure 2.5: Best maximum sidelobe for phased arrays containing a range of antenna numbers between 6-32 . The array response to a point source at 29 GHz was calculated for several thousand random placements of antennas in a 150 mm disc. The lowest maximum sidelobe, relative to the main lobe at 0 dB, in the ±50° field-of-view (FOV) (horizontally and vertically) is plotted against antenna number. The greater the number of antennas, the more accurately the array can image a point source.

- frequency range 20-40 GHz
- one four channel module per antenna (two polarisations at two frequencies)
- maximum width of 40 mm
- high gain, greater than 10 dB
- IF bandwidth of 50 MHz

Mixers with IQ capability to retain phase information is essential for aperture synthesis. Their RF frequency range could be curtailed at the expense of radial range of view in the plasma, in turn this would reduce the antenna performance constraint. A high gain mixer is desirable as the signal in passive acquisition mode will be rather low in power. Other optimal features of the mixer module and components are a minimal module width and height (in plane of array), ability to control remotely and availability to buy and use in the United Kingdom. For the two active probing channels the downconverter mixer block is replaced by an upconverter mixer block. This should have all the same characteristics as the downconverter mixer module.

To minimise the high frequency signal path length, we will place each mixer module directly behind its antenna. This makes the spatial volume of the mixer module a key parameter to constrain. The module's width and height, looking down the antenna's boresight, directly impact the array placement and consequently the array sidelobes. Its length does not affect the array performance, however power loss per unit length of transmission line increases significantly with frequency, so the RF track length should at least be minimised in balance with other constraints. Simulations of the frequency dependence of this power loss are discussed in section 5.10. The downconversion for

Component	Volume [cm^3]	Unit cost [£]	Mass [g]	No. units
Mixer (MMIQ-1040LS)	11	1,760.70	14	128
Amplifier (ZVA-443HGX+)	93	2,500	220	64
Power-divider (TB-EP2KA+)	15	820	45	64
Totals	8,320	437,849.60	18,752	

Table 2.2: The volumes, unit costs and masses of the main components required to build a connectorised version of the SAMI-2 down-conversion subsystem, along with the total volume, cost and mass.

SAMI-2 could have been constructed using off-the-shelf pre-packaged components. A set of components forming a roughly equivalent subsystem are listed in Table 2.2, along with their respective volumes, unit costs and number required. Given the fixed antenna array diameter of 15 cm, if the total 8.320 cm^2 volume could be packed into a cylinder of the same diameter it would have a length of 47 cm. As we show in chapter 5 a custom solution is made with a length of under 20 cm. Furthermore, the masses of connectorised components become significant in a system with 32 antennas and the support structure for such would require more rigorous design than for the relatively light custom PCB solution. Component frequency range is a major factor in microwave mixer cost and options are limited for broadband mixers in the K and Ka frequency bands. Customised RF module PCBs are undoubtedly less expensive than an off-the-shelf equivalent: the total cost in Table 2.2 of £438,000 is almost three times the entire SAMI-2 budget! Even with multiple prototyping stages, producing 32 custom mixer modules, described in chapter 5, has cost under £40,000.

2.3.3 Local oscillator

Optimal performance of the Local Oscillator subsystem:

- two simultaneous frequencies
- frequency range matching that required by the mixers
- fast switching time, on the order of 1 ms
- 64-way division for each frequency channel
- highly tunable frequency
- flat power output over frequency

Other optimal features are a small form factor of the signal generators and the associated power dividers as well as SPI or i2c control of the generators. The LO switching time is chosen so the probing frequency may be swept within a plasma shot, enabling measurement of the radial variation in magnetic pitch angle. A LO switching time on the order of 1 s would be too slow, given that the maximum planned shot length on MAST-U is 5 s. Although the edge turbulence correlation time was ∼20 µs on the Mega-Ampere Spherical Tokamak (MAST) [87], a microsecond switching time is

much faster than necessary here. SAMI-2 has two independent probing frequencies, which means it need not switch frequencies faster than the eddy time, because signals from the two channels can be correlated. The cost and complexity of the LO subsystem would increase were it to have a microsecond switching time. Therefore, the target switching time is chosen as 1 ms to balance the cost and deliverability with the ability to radially scan the plasma in each shot.

The local oscillator is comprised of two signal generators, one for each simultaneous frequency, and power division of these signals over the 32 down-conversion PCBs and the up-converter modules. Due to the dual polarisation operation of SAMI-2, each LO must undergo an extra division stage on the up- and down-conversion PCBs, making a 64-way division overall. Its frequency range should match that required by the up- and downconverter mixers and the output tuneable within that range. The signal generator's switching time between frequencies should be as least as fast as the mixers' switching times to avoid being the bottleneck in radial scans of the plasma. The initial 32-way power division should be performed using connectorised components of acceptably small form factor, with low deviation in loss between channels and relatively flat output power versus frequency. The final output power, after amplification and division, must be sufficiently flat over frequency so as not to impact the mixer performance.

The original SAMI used a set of DROs (Dielectric Resonance Oscillators) which are expensive and have a fixed frequency. Technological progress in the intervening years has yielded affordable Phased-Locked Loop (PLL) signal generators which provide a tuneable broadband signal output. Chosen fixed LO frequencies on SAMI went up to 17.25 GHz as it used second-harmonic mixers. The ADMV1014's internal LO frequency quadrupler drastically reduces the complexity of the LO supply. Other candidates, such as the HMC8192, would require LO provided up to 40 GHz, greatly increasing the subsystem's performance requirements and cost.

2.3.4 Analogue-to-digital converters

The MAST MSE system had a time resolution of 1 ms, which was sufficient to resolve the edge pitch-angle evolution [77]. SAMI had a sampling rate of 250 MSps and a 14 bit sample depth, but the data had to be averaged over 8 ms chunks to produce a relatively smoothly varying measurement. With 15 times SAMI's number of baselines and, coincidentally, 15 times as many channels, SAMI-2 will not need such long integration times. We will reduce the sampling rate to 125 MSps of 12 bits on SAMI-2, in order to limit the data rate but maintain sufficient dynamic range and reduce the time resolution to match the MSE system. A component search for these criteria is performed to select the most cost-effective part manufactured by Analog Devices, who provide comprehensive, well written documentation. Products from Texas Instruments were also searched.

Unless the mixer IF output matches the ADC sampling frequency, anti-alias filtering will be required between these two stages. A cheaper option than the IF filters available from Mini-Circuits was sought. The filter needs good transmission in the passband while the stopband leakage only need be below a reasonable level. Consequently, a custom filter of the Inverse Chebyshev (or type 2 Chebyshev) was designed using discrete surface mount components. As the diagnostic as a whole requires lots of gain, which is simpler and cheaper to apply to the IF than the RF, an amplification module is specified in the ADC subsystem to provide low-noise amplification. Again, an Analog Devices part search was conducted and the AD8331 ultralow noise, programmable amplifier IC

selected. The amplifier, filter and ADC are designed on three separate PCBs to reduce maintenance and upgrade costs.

2.3.5 Acquisition

SAMI-2's acquisition subsystem should be able to acquire data for an arbitrary length of time, ideally up to 5 seconds which is the maximum length planned for a plasma shot on MAST-U. With eight IF channels per antenna in an array of 30 there are 240 channels to process simultaneously. This necessitates real-time data processing with streaming to storage and consequently the number of bits per sample stored is limited by the streaming bandwidth. As many bits will be retained as possible. Development of part of a Field-Programmable Gate Array (FPGA) solution for this subsystem is described in C. Vincent's PhD Thesis [88]. The design and testing of the full acquisition subsystem will be presented in a future publication on the SAMI-2 diagnostic. FPGAs offer a highly flexible approach and their firmware can be continually updated *in situ*. However, they are difficult to program which increases the development time of the subsystem. The selected FPGA board must offer sufficient headers for signal inputs and control outputs to operate all the RF and IF electronics. In addition, it should have sufficient on-board memory to temporarily store data dumps, to transfer into storage between shots, in the first instance. It is desirable for a reduced set of data to be streamed directly to storage as the MAST-U shot length increases, requiring sufficient high-bandwidth outputs on the FPGA board. The board must be reasonably priced for its performance as an off-the-shelf unit.

2.4 Acquisition block diagram and integration

We had to design the SAMI-2 front end to interface effectively with the digitisation and acquisition back end. We used the same Samtec high density connectors on the down-converter, IF amplifier, filter and ADC modules for compatibility.

On the down-converters and IF amplifier module we assigned the facing connector pins in a rotationally symmetric manner, so that it does not matter which orientation two boards are connected. By placing power pins on the outer sides for the 40 pin connector, power planes are routed along the side of the board. IF differential pairs are This allows the down-converters to be attached to their respective antennas either way up. As we will see in chapter 5, the final down-converter is asymmetric either side of the RF connectors, so the flexibility afforded by a rotationally symmetric cable makes the array placement easier.

A schematic diagram of one SAMI-2 digitisation and acquisition subsystem module pair is shown in figure 2.6. Ten of these modules make up the full SAMI-2 acquisition subsystem, each handling the eight differential analogue channels from three antennas. Each set of eight channels passes through the IF amplifier module and a bandpass filter module before being digitised on its ADC module. Next, each ZCU102 FPGA processes the resulting 24 digital channels, packages them and sends them over 10 gigabit ethernet to data storage. This diagram does not include the clocking module, which synchronises the ten blades together, the power supply or the Ethernet network switch.

One blade provides the active probing signals to the two active probing antenna elements,

following the reverse process to the receiver blades. A digital to analogue converter (DAC) outputs an analogue IF which is passively filtered, then transmitted to the up-converter. The digitisation and acquisition systems modules have been tested individually and in unison, using dummy IF signals in place of the mixer module outputs. With the addition of a mixer module, we then tested the entire diagnostic (without the antenna array, instead using the RF output directly from an up-converter into the down-converter). This proved successful and repeatable between channels and the three digitisation submodules on the blade. Each diagnostic component is ready for testing and a full system test will follow in due course. This will initially be conducted using the prototype sinuous antenna array (shown in figure 4.8), while the final 30 element array is being constructed.

2.5 Mechanical design

Most of the SAMI-2 hardware will be situated adjacent to the tokamak vessel: blocks 1-5 in figure 2.1, while the data storage machine (block 6) will be located in a server room rack. Blocks 5 and 6 will be linked by fibre optic cables. The ADC and data acquisition subsystems (4 and 5) are housed in an aluminium exoskeleton frame, which will be attached to the MAST-U sector 5 midplane flange. Blocks 4 and 5 are modular, supporting three antennas worth of channels per whole module. One such module, referred to as a blade, is displayed in figure 2.7 in the frame.

The SAMI-2 blades will be arranged vertically inside the bottom section of the frame. Figure 6.2 shows their orientation relative to the front-end in the middle (shown by the three grey discs) and the tokamak vessel on the left (transparent). The top section of the frame holds the LO power dividers (cream), the power supply (black) and the clocking module (blue). A typical down-converter module is shown linking the three grey discs (bulkheads), and the 30 down-converters will be supported by these bulkheads, which will be 3D printed. The LSHM connectors and cables will be joined at the back bulkhead, and a middle bulkhead will provide additional support along the board's length. The With-wave connectors will pass through the front bulkhead, which will directly link to the balun and array support mount, shown in figure 4.8. Coaxial cables will link the LO power dividers and the microwave PCBs and Samtec HLCD flat tape cables will join the digitisation modules to their respective down-converters, providing power and control and receiving the IF.

2.6 Constraint interrelations

Most constraints are interrelated, have an impact on, and are affected by many of the other constraints. The grid in figure 2.8 categorises the effect of maximising and minimising each constraint (by row) on all other component constraints (by column), these extrema are described for each subsystem in section 2.3. Blue elements denote an increased effect on that particular constraint, making it harder to deliver at the desired level. Red elements show a decreased effect on a constraint, making it easier to deliver at its desired level. Maximising or minimising the performance constraint (A) of a subsystem sets the performance to the top or bottom of the ranges defined above. Maximising the spatial bulk constraint (B) requires that subsystem to occupy the smallest possible space, and relaxing this constraint increases its allowed volume. A maximised cost constraint (C) means that budget does not limit development, and vice versa. Finally, maximising the deliverability constraint (D) necessitates that the deliverability must be as fast and simple as possible.

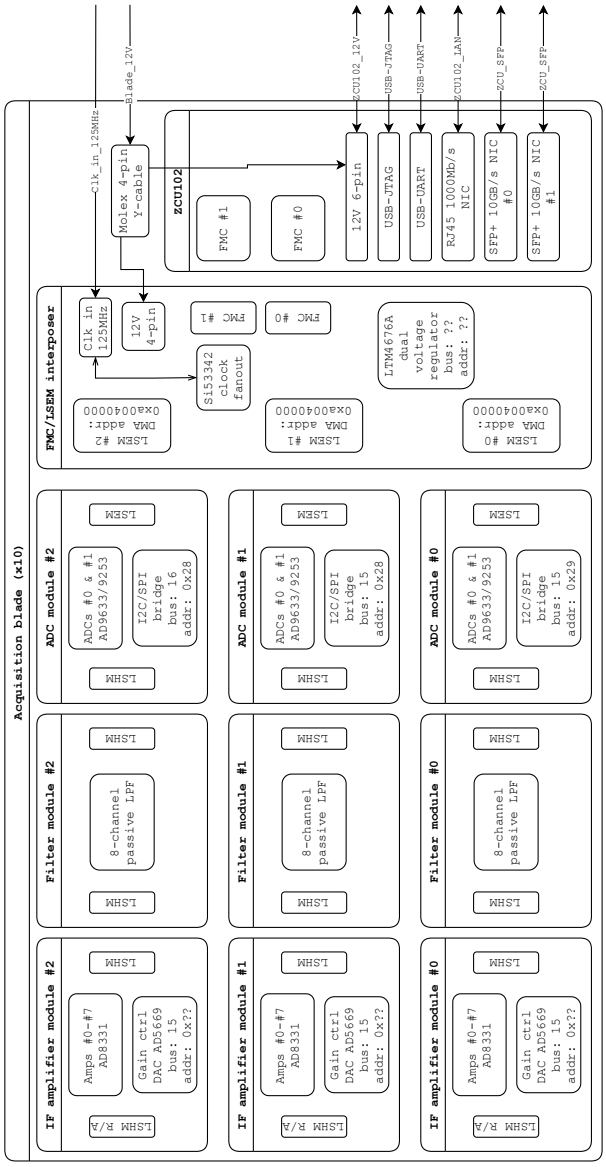

Figure 2.6: Block diagram of one of the SAMI-2 acquisition system modules (blades), receiving IF signals from the down-converters on the left hand side and outputting the digitised data over $10\,\mathrm{GB\,s^{-1}}$ links on the right hand side. There are 10 blades in the final diagnostic, which each support three antennas. Each of the three down-converters connects to its own digitisation signal chain, made up of the IF amplifier module, filter module and ADC module. The ADCs' outputs are fed through an intermediary PCB into the ZCU102 FPGA, then transferred to the storage PC (not shown). The gigabit Ethernet network switch, clocking module and power supply are not shown. Diagram produced by Roddy Vann.

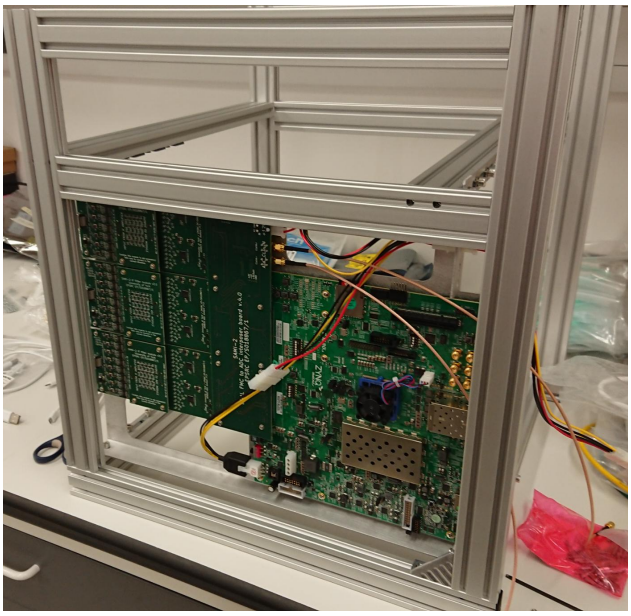

Figure 2.7: Photograph of one acquisition 'blade' in the SAMI-2 exoskeleton frame. The right hand board is the Xilinx ZCU102 FPGA, the data acquisition module. On the left hand side are three submodule chains, containing the IF filter, amplifier and ADC PCBs.

Having identified all of the constraints and interrelations, some have higher priority than others. These dominating constraints can be viewed independently from the rest, as the success of the diagnostic depends on them. Sidelobes arising from an array element number less than, or equal to about 16 will increase the uncertainty in the final pitch-angle calculations and will prevent the diagnostic from working as desired. Therefore, we can effectively remove antenna number from the mix of interrelated constraints, by fixing it at a higher value with sufficiently low resulting sidelobes. Conversely, an acceptable solution can be made using either the Vivaldi antenna or the sinuous antenna. Consequently, this constraint is not removed from the interrelated network as the sinuous antenna is not essential to the success of SAMI-2, because a Vivaldi solution will still be somewhat worthwhile. Frequency range is another dominant constraint. As can be inferred from figure 2.4, a maximum frequency below about 15 GHz (or a 50 GHz minimum frequency) would render the diagnostic useless for probing the edge plasma on MAST-U.

We moved away from quantifying the constraint and interrelation effects, as most are mainly qualitative. However, some effects may be made quantitative. For example, system cost scales roughly linearly with antenna number, as there are an integer number of most components per antenna. In contest with this cost scaling is array performance, which scales quadratically with antenna number. Total system cost can then be balanced against this measure of system performance, between the range of possible array element numbers. The port window diameter (externally fixed) limits the maximum antenna number and our choice of maximum sidelobe level limits the minimum antenna number.

As figure 2.8 shows, there are some interrelations which dominate when we seek an operable solution. For example, consider maximising α_{A} the antenna ability or performance, as detailed in section 2.3.1. This has a significant impact on both the deliverability of the antennas α_{D}, as it requires in depth research, and on the performance of the downconverter mixer modules, μ_{A},

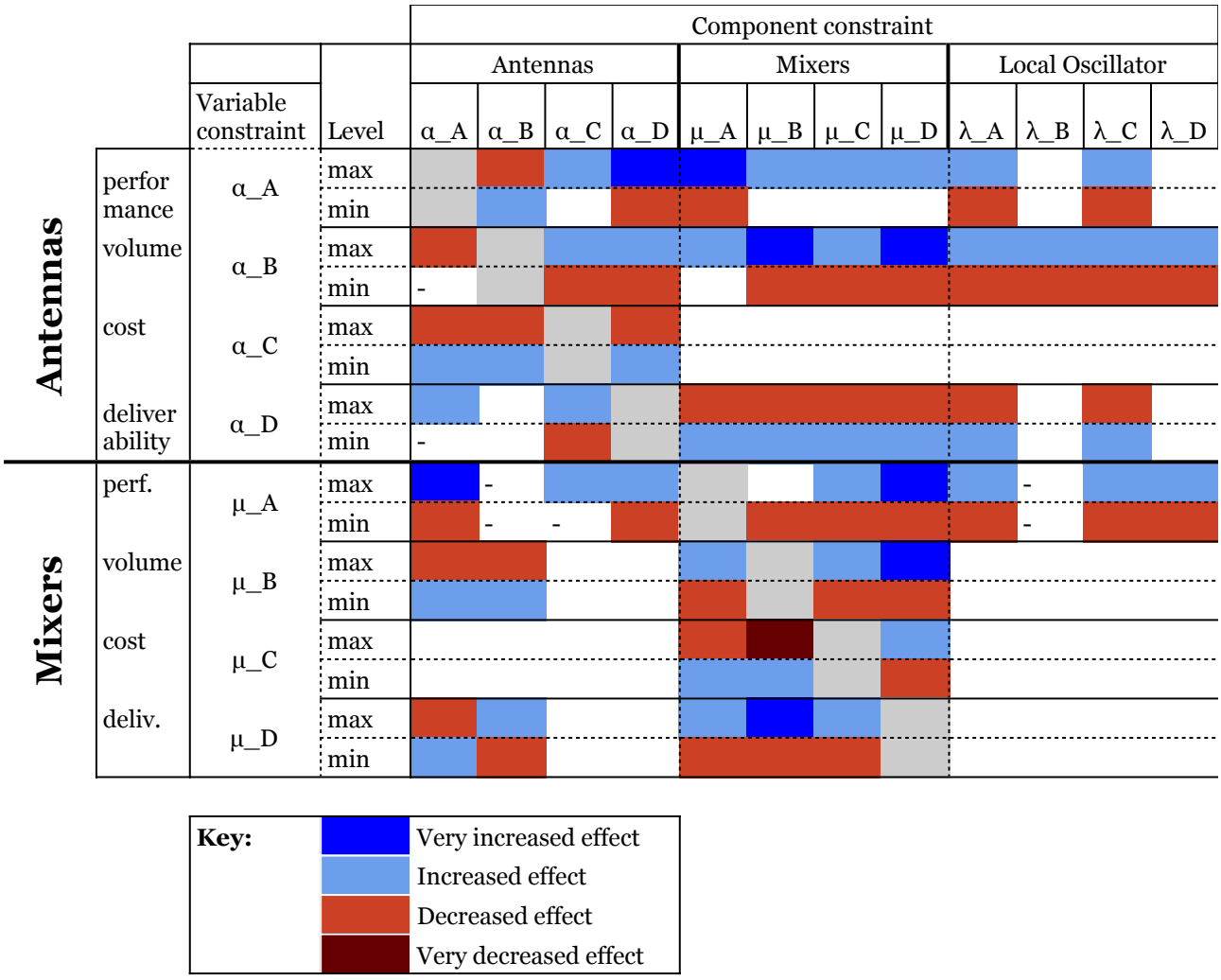

Figure 2.8: Constraint interrelation grid showing how varying each constraint of each subsystem impacts the other facets of each subsystem. Each row begins by maximising or minimising a constraint. The key lists the five categories of impact both these extreme shifts may have on every other constraint column. Increased effects (blues) indicate that for that constraint fulfilling its newly required level or maintaining its current level is now harder. Decreased effects (reds) make these easier.

which now needs to match the newly increased antenna performance. In turn, the now maximised μ_A puts pressure on mixer deliverability μ_D as it will now be more difficult to deliver them in the desired time frame and at the desired risk and complexity level. Achieving the optimum number of array elements, 32, or close to that number, moves α_B toward its maximum. In turn this applies pressure to the mixer bulk μ_B as the cross-section of the downconversion module must be limited to enable this number of antennas to actually fit within the 150 mm array. The major knock-on effect of the limited cross-section is to mixer deliverability μ_D as the design becomes more difficult and lengthy. The main reduction in pressure comes if mixer budget μ_C is maximised as this enables more prototyping steps, which will facilitate greater reduction of the module's cross-sectional area.

All impacts of maximising antenna performance α_A are now described as an example, shown in the top row of Figure 2.8. First considering the other antenna constraints: this reduces pressure on α_B as the target antenna design is small enough to fit at least 32 elements within the array diameter, increases α_C slightly as more prototyping stages will be required and greatly increases α_D as the maximal design requires new research, which is more risky and requires more time. Its impact on mixer constraints are: large pressure on μ_A due to the broad operational frequency range, and knock-on increases in pressure on μ_B, μ_C and μ_D. The requirements on the LO performance λ_A, and consequently its cost λ_C, are increased.

2.7 Concluding decisions

Some constraint interrelations raise immediate decisions to be made, whereas others nudge less critical choices in a certain direction but do not fix the choice. The key binary choice is between connectorised or integrated circuit mixers which, as explained in section 2.3.2 and compared in Table 2.2, is made by both volume and cost arguments in favour of designing custom PCBs. Stemming from this initial decision comes the choice of which integrated-circuit mixer to use in the PCB design, between Analog Devices' HMC8192 and ADMV1014. This was made externally by the delayed release of the HMC8192.

The option to redesign the Vivaldi antenna used in SAMI for use here provides a safety net for the research and design of the higher performance, optimal antenna. No such protection is available for the mixer subsystem and consequently the mixer design should take priority. Nevertheless, the benefits of an antenna fulfilling the optimal case, discussed in Section 1.11.2, should not be underestimated.

Digitisation rate can be reduced below the 250 MSps used in SAMI and sample depth can, and must, be reduced due the vastly higher number of channels in SAMI-2, compared to the proof-of-principle. FPGA specifications limit but do not make the choice: the chosen unit should support enough channels to cover roughly two to four antennas, to balance the required volume, cost of unit failure and difficulty of synchronisation. A data processing solution that can scale to MAST-U's planned maximum shot length of 5 s is preferred, such as direct streaming of reduced bit-depth samples to storage from the FPGAs.

Other constraints and interrelations may be satisfied by a relative continuum of solutions, which will therefore be finalised in later chapters. The down-conversion PCB may have a continuously varying width that must be confirmed before the antenna array layout is decided upon. Antenna number can, in principle, vary between 8-32 depending on the number of channels allowed by the

available budget. The extent of the antenna performance; operable frequency range, polarisation separation, gain profile and polarisation wobble are determined in chapter 4.

Chapter 3

Methodology

This chapter lays out the main methodologies followed in this thesis. It contains an overview of the design and experimental techniques used to produce a functional 2D Doppler backscattering (DBS) diagnostic. We describe a broad range of techniques in this chapter, all of which are required for the success of the project and all of which the author encountered for the first time after their PhD research began. First, we discuss some useful formulae, considerations and tools for printed circuit board (PCB) design at microwave frequencies. Second, the design equations and background theory for the Vivaldi and sinuous antennas are presented, along with those for an optimal matching network using the Klopfenstein taper. Following this, experimental techniques and common experimental set ups are described. Finally, the key computational framework used in this research, to simulate antennas and circuit boards, is described and derived in the simple 1D case.

To produce a particular component, one follows a rough sequence as follows: said component is designed, then simulated, then a prototype is manufactured and tested, from which the results are used to improve the design, thus restarting the cycle. One needs a degree of pragmatism, one cannot keep simulating and tweaking a component forever: at some point the component must be built and tested. One follows this loop until the device works sufficiently well, according to its specification. The Synthetic Aperture Microwave Imager-2 (SAMI-2) diagnostic is comprised of a number of subsystems, which we describe and specify in chapter 2. The production loops of each subsystem interact with each other, as the subsystems must interface with others, which complicates the process. This complexity necessitates further pragmatism: in initially drafting realistic specifications and updating expectations in line with prototype test results.

3.1 Microwave PCB design

3.1.1 Microstrip transmission lines

Microstrip lines are commonly used for PCB signal transmission as they are easily manufactured and facilitate simple connections between packaged integrated circuits. A thin conductor of width w is cut on a substrate of dielectric constant ϵ_r and thickness t, faced by a ground plane, a diagram of which is shown in figure 3.1. When investigating the mode carried by such a transmission line it is useful to first consider the special case when the substrate is a vacuum, $\epsilon_r = 1$. The system

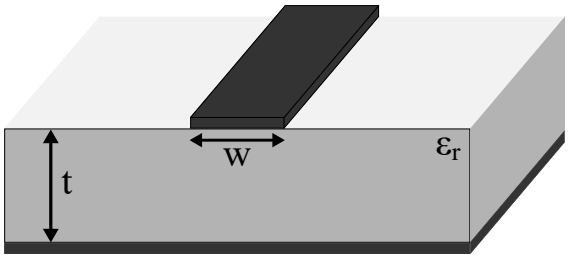

Figure 3.1: Generic microstrip transmission line geometry with parameters line width w, substrate thickness t and substrate permittivity ϵ_r, with a ground plane on the underside.

reduces to a two-wire line in a homogeneous medium and hence carries a transverse electromagnetic (TEM) mode, with phase velocity $v_p = c$ in a vacuum.

A microstrip line on a given PCB substrate, permittivity ϵ_r, carries signals whose fields straddle the substrate-air interface. Therefore, the microstrip cannot support a pure TEM mode as this would propagate at different phase velocities in the two media, leading to a phase discontinuity at their interface. In reality, a microstrip line supports a complex hybrid TE-TM mode, which, for the common case where $t \ll \lambda$, can be approximated as a quasi-TEM mode. The following simplified formulae, equations 3.1, 3.2 and 3.3, are approximate solutions from curve-fitting to more involved quasi-static equations [89]. For this approximation, an effective permittivity ϵ_e is estimated by

$$\epsilon_e = \frac{\epsilon_r + 1}{2} + \frac{\epsilon_r - 1}{2}\left(\frac{1}{\sqrt{1 + 12\,t/w}} + \Lambda\right), \tag{3.1}$$

to combine the contributions of fields in the substrate and in the air into a single value for the dielectric constant experienced by the transmitted wave. If the line width is less than the substrate thickness the additional factor Λ adjusts the effective dielectric constant accordingly:

$$\Lambda = \begin{cases} \left(0.04\left(1 - \frac{w}{t}\right)\right) & \text{for } \frac{w}{t} < 1 \\ 0 & \text{for } \frac{w}{t} \geq 1. \end{cases} \tag{3.2}$$

The impedance of the line, Z_0, is approximated by

$$Z_0 = \begin{cases} \frac{60}{\sqrt{\epsilon_e}} \ln\left(\frac{8t}{w} + \frac{w}{4t}\right) & \text{for } \frac{w}{t} \leq 1 \\ \frac{120\pi}{\sqrt{\epsilon_e}(w/t + 1.393 + 0.667\ln(w/t + 1.444))} & \text{for } \frac{w}{t} \geq 1, \end{cases} \tag{3.3}$$

where again there are two forms depending on the w/t ratio.

For most conventional microstrip lines this quasi-TEM approximation holds, allowing simplified analysis of the line's effective dielectric constant and impedance. The electric and magnetic fields of a typical quasi-TEM mode are sketched in figure 3.2. For relatively wide lines a greater proportion of the electric field is situated within the substrate, whereas for thinner lines this proportion decreases, leading to the dual forms of equations 3.1 and 3.3.

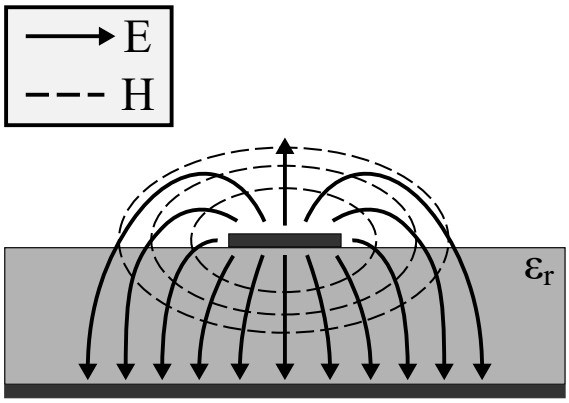

Figure 3.2: Cartoon electric (solid) and magnetic (dashed) field lines of the quasi-TEM mode in a cross section of a microstrip transmission line. The quasi-TEM approximation holds for $t \ll \lambda$. The tangent of the electric field is continuous across the substrate-air boundary and the magnetic field component perpendicular to the boundary is also continuous.

3.1.2 High frequency design considerations

As the frequency band of interest begins to extend into the gigahertz range, several aspects of PCB design become more complicated. Shorter wavelengths are likely to be more similar in scale to features on the board and interact with them to a greater extent. Impedance matching of high frequency tracks is therefore very important, particularly in locations with a higher chance of suffering discontinuities, such as corners, connector launches and integrated circuit (IC) pin connections. A proportion of the propagating signal is reflected at an impedance mismatch, relative to the difference between the two impedances. Corners should be curved but if space is too tight, for a bend radius greater than three times the track width, they should be mitred. Connector launches should be simulated and the results confirmed experimentally using a pass-through PCB. If possible, connections to IC pins should be replicated from the component's datasheet. Signal paths should be routed in order of decreasing frequency, so that component positions are chosen to make the paths carrying higher frequencies shorter, thus reducing loss of the most important signals.

A material specifically designed for use as a high-frequency PCB substrate should be used. It should have stable permittivity so a given track width's impedance is reproducible between PCBs, as well as a low loss tangent, a measure of signal dissipation in the dielectric. Sufficient low impedance interlinking between ground sections should be placed. Grounding via fences alongside grounded coplanar waveguide (GCPW) transmission lines should be regular, to maintain a constant impedance and to keep the propagating fields as stable as possible.

3.1.3 KiCad

KiCad is a powerful collection of open source software supported by CERN (and other organisations) for PCB design. Its variety of tools for electronic design automation (EDA) aids the process of designing PCB schematics and transforming them into copper artwork, which can then be manufactured. KiCad comes with large libraries of component schematic symbols and footprint copper layouts, which ease initial development. Most key files, such as footprints and PCB layouts, can

be viewed as raw text files, enabling fast batch editing (often of mistakes!) and a high degree of customisation. It benefits from a strong online community providing support and user-made plugins to extend the program's capability. Many manufacturers offer symbols and footprints for their components in KiCad file formats which simplifies the PCB design process. If these are not provided, SamacSys offer a part request service [90].

3.1.4 Gerber files

The Gerber file format is an open specification for PCB design [91]. It has become the de facto standard in PCB design tools and for manufacturers. Gerber files describing circuitry in this thesis were produced using Kicad, Wolfram Mathematica or CST Microwave Studio, depending on the specifics and provenance of the board in question. The down- and up-converter in chapter 5, along with the other manufactured boards in the same chapter, were designed almost entirely using Kicad. For some of the more complicated copper shapes such as the sinuous antenna and balun designs, as well as the Vivaldi antennas (all in chapter 4), Mathematica was used to produce the shapes to import into Kicad. CST's Gerber export function was used for high-frequency connector launch designs which were tweaked within the simulation package, then imported into Kicad.

3.1.5 PCB manufacturers

We describe two distinct types of PCB in this thesis. The first type is those of the antennas in chapter 4, which are two-layer, bare boards containing no assembled components, with complicated copper artwork. Garner Osborne are a small to medium batch PCB manufacturer and assembler, based in Berkshire. We visited their factory to discuss the sinuous antenna design and their manufacturing process, which helped us reach a feasible design. Several of their manufacturing tolerances, such as minimum track width, plating thickness, minimum drill diameter and drill location precision, influenced the sinuous antenna plated slot feed design. The requirements for this design reached some of the boundaries of Garner Osborne's manufacturing limits, requiring them to order the smallest router tip available from their supplier (0.3 mm). The second type of PCB described in this thesis are larger boards for signal processing, involving a number of ICs. For this type we chose Eurocircuits as the manufacturer, which is based in Belgium. They offer order pooling with other customers to reduce costs, as PCB substrate panels come in fixed sizes, parts of which may be wasted without order pooling. We also made this choice because Eurocircuits' automated online checking tools are invaluable for ironing out design and manufacturability issues before boards are fabricated.

3.2 Antenna background

The antenna specification for SAMI-2 is described in section 2.3.1. The proof-of-principle SAMI diagnostic used Vivaldi antennas in its array. Although these are adopted as the baseline case for SAMI-2, they have some undesirable characteristics, as previously described in section 1.11.2. A dual-polarisaion sinuous antenna design is therefore presented in chapter 4 to ameliorate these issues. Introductions to the design of both the Vivaldi and sinuous antenna, along with their feed networks, are presented in this section.

Figure 3.3: The copper artwork for each side of the antipodal Vivaldi antenna annotated with key design dimensions. It is to be driven by a connector on the left hand side launching to the purple microstrip section of width W_{MS}. The microstrip tapers to a section of symmetric microstrip before following an exponential flare from x_{flare} out to the nose of the antenna.

3.2.1 The Vivaldi antenna

Vivaldi antennas are broadband, high gain, have low cross-polarisation and can be manufactured on PCB. Their design was first published by Gibson in 1979 [92] and has been developed, branched and used in many areas since [93–97]. Eight broadband antipodal Vivaldi antennas were used on SAMI operating from 10-35.5 GHz [78] and were manufactured on Rogers Duroid 5880 substrate, thickness 0.381 mm.

The modified SAMI Vivaldi antennas featured an antipodal slot line first suggested by Gazit [94]. The vertical position y of the flare openings in this modified design, relative to that at x_{flare}, is described by:

$$y = c_1 e^{Tx} + c_2, \tag{3.4}$$

where x is horizontal position, T is the flare opening parameter, $c1$ and $c2$ are constants and y is the resulting vertical position. A labelled diagram of the antipodal Vivaldi antenna is shown in figure 3.3. At $x = 0$, on the unbalanced signal copper layer (purple), a connector launches to a traditional 50 Ω microstrip line, width W_{MS}. Between x_{taper} and x_{Rcentre} this tapers linearly to a balanced microstrip, width W_{SYM}: calculation described in section 3.2.5. At position x_{flare} the copper follows the exponential flare described in equation 3.4 on one side, and a circular arc radius R on the other. The unbalanced ground layer (green) is constructed in the same way apart from beginning at $x = 0$ as a ground section of full width $W + 2D$, which follows the same circular arc to provide the back-layer mirrored track in the balanced microstrip line at x_{Rcentre}. The slot end opening between the opposing flares, labelled W, is determined by the bottom cut-off frequency [97]:

$$\text{W} = \frac{c}{f_0\sqrt{\epsilon_r}}. \tag{3.5}$$

3.2.2 The sinuous antenna

Patented by DuHamel in 1987 [98], the sinuous antenna is produced by adding log-periodicity to a spiral antenna. This combination retains wideband capability while enabling dual-linear polarisation usage. A sinuous antenna possesses a self-similar shape which can be scaled to cover the desired frequency range of operation and means their impedance is independent of this frequency range.

Furthermore, they consist of planar antenna arms which can be repeatably manufactured on PCBs, allowing production of pre-aligned arrays of sinuous antennas. This combination of benefits has led to a broad range of uses in areas such as radio astronomy [99, 100], aerospace [101], and Terahertz wave applications [102]. Most examples in the literature are manufactured to operate below 20 GHz [103–105]; only Edwards et al. is found to show dual-polarised sinuous antenna operation up to 24 GHz.

The sinuous shape in polar coordinates (r, ϕ) is defined by

$$\phi = (-1)^p \, \alpha \sin\left(\pi \frac{\ln\left(r/\tau^p R_0\right)}{\ln \tau}\right) \pm \delta \qquad \text{for} \quad R_0\tau^p < r < R_0 \quad (\text{when } \tau < 1)\,, \tag{3.6}$$

with fixed design parameters α, τ, δ and R_0. The outer radius of the arm R_0 is built up in p integer successive switch-back cells each of inner radius $\tau^p R_0$. The curve's divergence angle α is traced through twice in each cell, once in the positive direction and once in the negative direction; the scaling factor τ determines the radial growth of the antenna; and δ sets the angular width of each arm. The two resulting curves are shown in figure 3.4, where $\tau = 0.77$, $\alpha = \frac{\pi}{4}$, $\delta = \frac{\pi}{8}$. Each of the four arms of the dual-polarisation sinuous antenna structure is created by sweeping between these two curves and rotating about the origin.

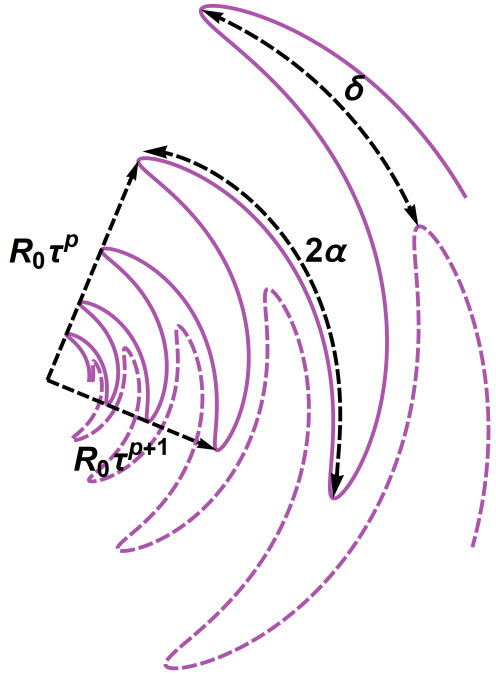

Figure 3.4: Diagram of the two sinuous curves resulting from equation 3.6. Parameters labelled are the outer radius R_0, the expansion factor τ (0.77), cell number p, divergence angle α ($\pi/4$) and angular arm width δ ($\pi/8$).

Typical values of α are between 30-70° and the usual range of τ values is 0.7 to 1.5 [102, 105–107]. Simulations show that a lower value of τ reduces the variation of polarisation angle over frequency [102, 105]. A self-complementary shape is identical to its inverse arbitrarily rotated about a common origin: for the four arm sinuous antenna, if the metal is swapped from the arms

to the gaps between the arms, the same structure is produced rotated by 45 °. Self-complementary structures have real impedances which are independent of frequency [108]. For the four arm sinuous antenna, the arm width parameter δ must be 22.5° to preserve frequency independent impedance, by retaining the self-complementary nature of the antenna shape.

To calculate the four-arm sinuous antenna's impedance one may first consider the a single port antenna formed of two conductors. A consequence of Babinet's principle relevant to antenna design is:

$$ZZ' = \left(\frac{\eta}{2}\right)^2 \tag{3.7}$$

where Z and Z' are the impedances of the antenna and its complement, respectively, and η is the impedance of the medium containing the antenna. For a self-complementary antenna $Z = Z' = \frac{\eta}{2}$ which, for an antenna in free space, equals $\frac{\eta_0}{2} = 188\ \Omega$ [109]. Log-periodic antennas cannot be connected to their feed network from the low frequency end, otherwise the high frequency signals will excite higher order modes in the antenna before reaching the high frequency end at which they should radiate (receivers suffer from the same problem [108]).

The sinusoidal, log-periodic shape of a sinuous antenna receives and emits waves when the distance between switch-back sections on opposing arms equals $\lambda/2$. Therefore, the structure responds to shorter wavelengths nearer its centre and longer wavelengths at its extremities. Its low frequency limit is

$$\lambda_{\max} = 4R_0(\alpha + \delta), \tag{3.8}$$

and the antenna's upper frequency cutoff is

$$\lambda_{\min} = 8\tau^p R_0(\alpha + \delta), \tag{3.9}$$

after allowing for a transition region between the central feed and the high frequency cut off radius, to ensure reliable impedance and emission patterns [98].

3.2.3 Baluns

The word *balun* is a portmanteau of ***bal****anced* and ***un****balanced*. The balanced port has two outputs 180° out of phase with each other, which are floating (due to the fact that they are not referenced to ground). The unbalanced port has a signal and a ground terminal input, e.g. a coaxial cable or a microstrip line. Even and odd mode input at the unbalanced end of the balun is transformed into solely odd mode at the balanced end [110]. Impedance matching capability can be combined with the balancing transformation within a single device by tapering both signal and ground unbalanced input traces to a new width of the desired impedance.

3.2.4 Klopfenstein taper

The Klopfenstein, or Dolph-Tchebycheff, transmission line taper provides an optimum impedance transformation for a given length taper. It achieves this by minimising the reflection coefficient over the chosen bandwidth, using the theory of small reflections [111]. A taper of this form offers the best possible performance for a given taper length or the shortest taper length for the specified

maximum reflection. The impedance $Z(x)$ along the x-axis is given by:

$$\ln Z(x) = \frac{1}{2}\ln(Z_0 Z_\mathrm{L}) + \frac{\rho_0}{\cosh(A)}\Phi\left(\frac{2x}{L} - 1, A\right), \qquad \text{for } 0 \leq x \leq L \tag{3.10}$$

where Φ is the modified Bessel function

$$\Phi(z, A) = \int_0^z \frac{I_1(A\sqrt{1-y^2})}{A\sqrt{1-y^2}} dy, \qquad \text{for } |z| \leq 1, \tag{3.11}$$

where $I_1(\cdot)$ is the Bessel function of the first kind, which is even in z. The impedance conversion factor ρ_0 is

$$\rho_0 = \frac{1}{2}\ln(Z_L/Z_0) \tag{3.12}$$

and A sets the maximum amplitude of the reflection coefficient in the pass band, equal to $\rho_0 \cosh A$.

3.2.5 Balanced microstrip

As well as the Klopfenstein taper used to match the impedance to the antenna, a further transformation from regular, unbalanced microstrip to a balanced transmission line is required, as the antenna is a balanced structure. In this case, it is straightforward to transition to a balanced microstrip transmission line, where the widths of the signal and ground copper are equalised. Svacina [112] semi-empirically calculates the parameters of a given balanced microstrip line, using a Moving Perfect Electric Wall (MPEW) for any substrate height, dielectric constant or opposing track width ratio. The MPEW acts as a virtual ground between the two conductors (a PEW) which can be used to separately calculate each of their impedances which are summed to find the combined impedance of the balanced microstrip line. The MPEW is almost a plane bisecting the substrate between the two conductors and only significantly differs in the "far" field domain beyond the extent of both conductors, where it begins to diverge away from the wider conductor. A cartoon of a microstrip line with finite ground plane, showing how the PEW sits between the two conductors, is displayed in figure 3.5. This method considers two opposing conductors of width w_1 and w_2 across a substrate of thickness h and dielectric constant ϵ_r. The distance of the MPEW from conductor 1 is given by

$$h_1 = \frac{h}{2} + \frac{h}{2} \cdot \frac{\left(\frac{w_2}{w_1}\right)^{w_1/h} - 1}{\left(\frac{w_2}{w_1}\right)^{w_1/h} + 1}, \tag{3.13}$$

with bounding results of $h_1 = h/2$ for the balanced case where $w_1 = w_2$ and $h_1 \to h$ as $w_2 \to \infty$ and the second conductor becomes an infinite ground plane, returning to a microstrip line.

3.3 Experimental techniques

Several generic types of experiment were conducted in the research and development of SAMI-2. An overview of the techniques and equipment used is presented here, before particular instances of these experiments are described in later in Chapters 4 and 5.

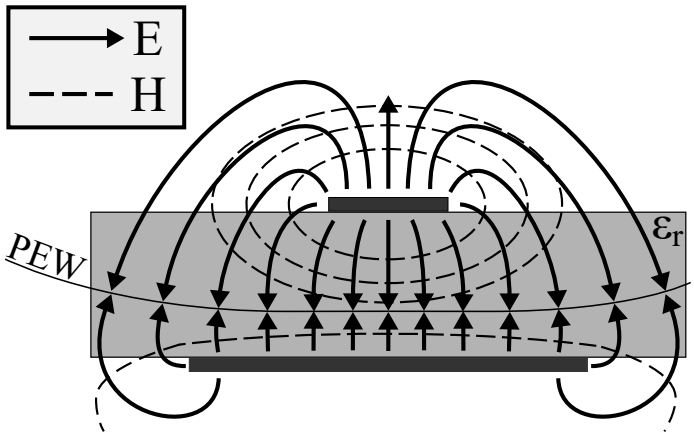

Figure 3.5: Cartoon diagram of finite-ground microstrip, an intermediate step between conventional microstrip (infinite ground plane) and balanced microstrip. The PEW (snapshot of a MPEW) in between the two connectors is used as a virtual ground, in order to separately calculate the impedance of each conductor. Sketched electric field lines are shown by solid arrows, and the magnetic field is the dashed lines.

3.3.1 S-parameters

In microwave electronics, scattering parameters, or S-parameters, describe the transmission and reflection of signals between ports of a network. They are commonly written as a scattering matrix $\boldsymbol{S}$ operating on the incident waves, $\underline{a}$, to each port in the network to give the transmitted and reflected waves, $\underline{b}$, at each port [110], shown by:

$$\underline{b} = \boldsymbol{S}\underline{a}. \tag{3.14}$$

For an N-port network this can be written as

$$\begin{bmatrix} b_1 \\ b_2 \\ \vdots \\ b_N \end{bmatrix} = \begin{bmatrix} S_{11} & S_{12} & \dots & S_{1N} \\ S_{21} & S_{22} & \dots & S_{2N} \\ \vdots & \vdots & \ddots & \vdots \\ S_{N1} & S_{N2} & \dots & S_{NN} \end{bmatrix} \begin{bmatrix} a_1 \\ a_2 \\ \vdots \\ a_N \end{bmatrix}. \tag{3.15}$$

The scattering matrix S contains N^2 elements each corresponding to one path through the network. Two port networks are the most common type referred to here, for which (3.15) reduces to

$$\begin{bmatrix} b_1 \\ b_2 \end{bmatrix} = \begin{bmatrix} S_{11} & S_{12} \\ S_{21} & S_{22} \end{bmatrix} \begin{bmatrix} a_1 \\ a_2 \end{bmatrix}. \tag{3.16}$$

The return losses, or proportions of reflected signal, into the two ports are S_{11} and S_{22}, respectively. For a passive device this is reciprocal, as the transmission in both directions is equal: $S_{21} = S_{12}$. The two-port matrix is symmetric when it is reciprocal and has equal reflection coefficients, $S_{11} = S_{22}$.

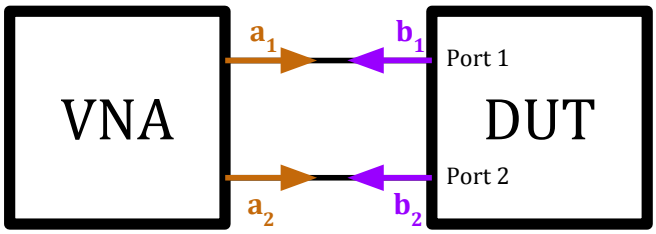

Figure 3.6: Simple experimental diagram using a two-port VNA to measure the S-parameters of a DUT. Incident waves a_1 and a_2 are sent out by the VNA and the transmitted or reflected waves b_1 and b_2 are measured. (3.16) can then be used to calculate the S-parameters of the two-port device.

3.3.2 Vector Network Analysers

A Vector Network analyser (VNA) sends a radio frequency (RF) signal into each of the ports of a device under test (DUT) and measures both the reflected amplitude and phase at that port as well as the amplitude and phase of the signal transmitted to the other ports. By transmitting signals, $\underline{a}$, into the ports of the DUT and measuring the transmitted and reflected signals, $\underline{b}$, over the desired frequency range the S-parameter matrix can be calculated for the network in question. A simple cartoon of this set up is shown in figure 3.6. Passive networks can be straightforwardly tested with a VNA as they will not return more power to the VNA ports than originally provided to the DUT. VNA ports are very sensitive, so any input signals must be strictly controlled. We used both the HP 8510C 26.5 GHz and the Anritsu ??? 40 GHz two-port VNAs. The 8510C is manually calibrated with a set of standard

3.3.3 Spectrum Analysers

Spectrum analysers measure the power over the frequency spectrum of an incident signal. Signals produced by components can be individually examined for spectral content prior to connecting multiple components together. In this way we safeguarded our experimental set ups against component damage by ensuring maximum input power ratings were not reached. Furthermore, in the case of components like mixers and frequency multipliers, their spectral content can be checked for spurious frequencies, such as unwanted sidebands or harmonics. Several measurements in this thesis were carried out with the HP 8564EC 40 GHz spectrum analyser.

3.3.4 Anechoic chamber

Anechoic chambers are often used to house antenna experiments, with the dual purpose of shielding external radiation and reducing reflections of emitted signals, by absorbing as much stray radiation as possible. A generic antenna experiment is described in the next section.

We designed and built an anechoic chamber with an operational range up to 40 GHz for the characterisation of the SAMI-2 antennas. A CAD diagram of the chamber is shown figure 3.3.4. The chamber must have a sufficient length, l, to ensure the emitter is in the far-field of the receiver, and such that the rotations of the receiver produce a negligible difference in the distance between

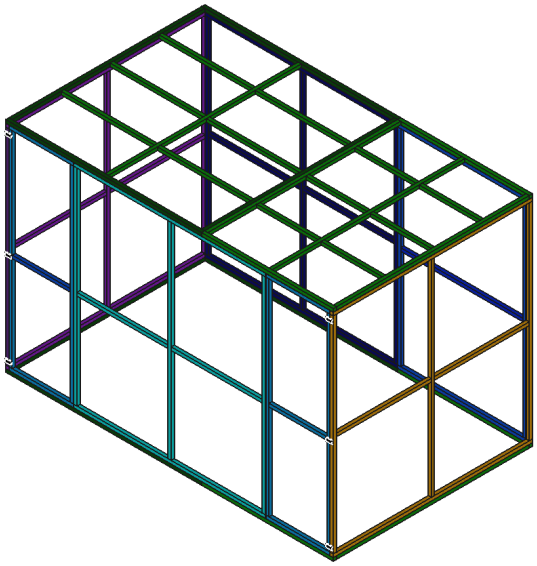

Figure 3.7: Anechoic chamber frame modular design with different colours highlighting separate panels. Only the extruded aluminium frame is shown here, thin aluminium sheet covers all six sides upon which the absorbing foam is adhered with velcro. The chamber has an approximate volume of $3 \times 1.8 \times 2\,\mathrm{m}^3$ and was modified from an initial design by K Niemi at the University of York.

the two antennas. The width of the chamber, w, must fulfil the condition

$$w \geq \frac{1}{\sqrt{3}}\, l, \tag{3.17}$$

to minimise reflections from the walls at angles less than 60° from the boresight of the antennas. We achieve internal shielding of reflections by covering the walls with absorbing foam, designed to give the good absorption over the chosen frequency range. The foam surface is a grid of pyramids, being tapered such that small reflections of incident radiation created tend to cancel one another out over the whole range of frequencies used. The foam spike gradient is effectively an impedance gradient, the minimum height of these pyramids must be greater than half the wavelength of the minimum operational frequency [113]. For a minimum frequency of 10 GHz the pyramid height must be greater than 1.5 cm. The foam we used is well over this limit, with a pyramidal height of 7.4 cm. An external view of the constructed anechoic chamber is shown in figure 3.8.

3.3.5 Generic antenna experiment

Prior to a measurement of the performance of a given DUT, the anechoic chamber is calibrated using two Flann Microwave DP-241AC horn antennas, which operate from 6-50 GHz (referred to hereon as horn antennas). The emission pattern of these antennas is known allowing characterisation of the insulating and absorbing capability of the chamber. A cartoon diagram of an antenna experiment in an anechoic chamber using a VNA is shown in figure 3.9. In this initial experiment both antenna 1 and 2 are standard horn antennas. The distance between antenna 1 and 2 is recorded as well as the selected polarisation of each antenna. The desired frequency range, number of points sampled within the range and the sweep time are selected, then the VNA is calibrated to remove the effect

Figure 3.8: An external photograph of the completed anechoic chamber frame and sheet panels. When pushed shut, the doors seal against the adjacent panel with an overlapping section of aluminium sheet. Several bulkhead connectors were installed for cable lines into the chamber.

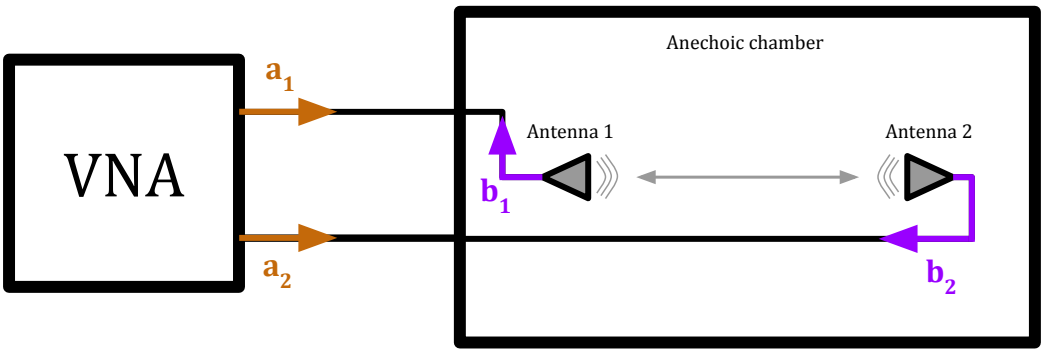

Figure 3.9: Block diagram of a generic antenna experimental set up in an anechoic chamber with a VNA. Here the DUT in Figure 3.6 is a pair of antennas and the anechoic chamber is designed to minimise internal reflections, as it is the direct signal transfer between the antennas which is to be measured.

of the cables between the VNA and the DUT. The VNA is one example of measureing device and could be substituted for a signal generator and spectrum analyser.

An example experimental setup is displayed in figure 3.10, with a horn antenna facing an array of sinuous antennas. In this case, the horn antenna is fed by the LMX2594 PLL synthesiser passed through a frequency quadrupler (the AQA-2040, which also provides amplification), seen in the foreground. The mount holding the sinuous antenna array is able to rotate through two axes and can be controlled programmatically. This allows measurement of the full two-axis emission pattern of a given DUT.

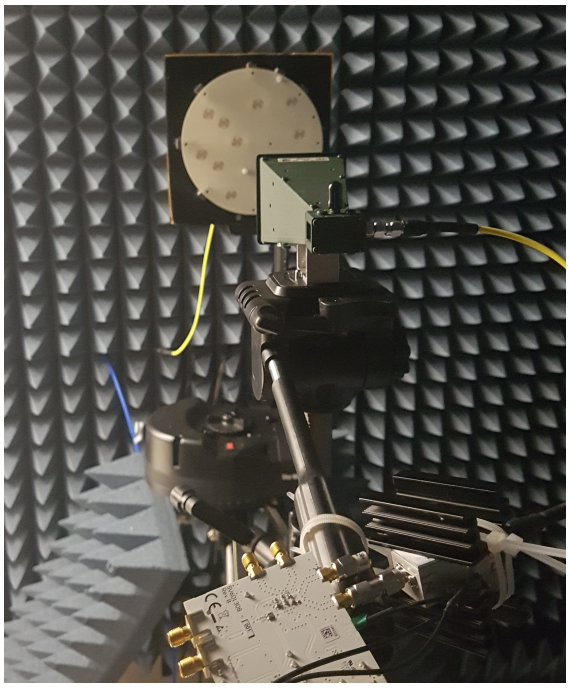

Figure 3.10: Photograph of an experimental set up in the anechoic chamber in figure 3.8 using a horn antenna (near) and an array of sinuous antennas. The horn antenna is fed by an LMX2594 PLL Synthesiser through the AQA-2040 quadrupler to provide it with frequencies between 20-40 GHz.

3.4 Simulation techniques

3.4.1 CST Microwave Studio

CST Microwave Studio is a widely used electromagnetic (EM) simulation tool sporting a well integrated set of CAD tools, enabling easy creation and tweaking of electronic components such as circuit boards and antennas within the user interface. An academic research licence is available making it affordable for non-commercial research. We used CST to simulate all of the PCBs presented in this thesis (and many more besides!). We created some directly in CST, while Gerber or image files of other PCB artwork were imported. The program saw most use by us in the design of the sinuous antennas (chapter 4) and in the process of choosing a 40 GHz connector (section 5.4). Objects we built in CST were able to be parameterised, which enabled us to easily tweak designs according to the results. The Visual Basic language can be used to automate object creation, we used it to initially place via fences alongside curved tracks, as seen in section 5.10.

3.4.2 Finite-difference time-domain simulation method

The finite-difference time-domain (FDTD) method is a widespread simulation technique based on a relatively simple concept which suits EM problems. Due to its construction and computational expense FDTD is usually best suited to structures of a size on the order of the wavelength under consideration. Ray-tracing methods are likely to be far more efficient at solving problems where the wavelength is much smaller than the structural features and quasi-static approximations are often more efficient when modelling features much smaller than the wavelength.

The generalised FDTD equations begin by using Taylor expansions either side of a central point to approximate the gradient at the central point. A summary of the formulation in 1D is presented here, see [114] for a thorough description of FDTD in three-dimensions and its implementation in the C programming language. We perform the Taylor expansion of the function $f(x)$ about $x_0 \pm \delta$ and subtract one from the other and divide by δ, which is equivalent to the derivative of $f(x)$ at x_0. If δ is sufficiently small this allows higher order terms (δ^2 and above) to be neglected, leading to:

$$\left.\frac{df(x)}{dx}\right|_{x=x_0} \approx \frac{f\left(x_0+\frac{\delta}{2}\right)-f\left(x_0-\frac{\delta}{2}\right)}{\delta}, \tag{3.18}$$

known as the central-difference approximation. This gives an approximation of the derivative of the function at x_0, with second order accuracy, using sample points either side of the central point.

3.4.3 Maxwell's equations solved using FDTD

The key steps for the formulation of Maxwell's equations in a 1D FDTD framework are contained herein. The electric field (E-field), $\mathbf{E}$, is related to the electric flux density, $\mathbf{D}$, by $\mathbf{D}(t) = [\epsilon(t)] * \mathbf{E}(t)$, where $[\epsilon(t)]$ is the permittivity, or dielectric, tensor of the medium in question. Similarly, the magnetic field (B-field), $\mathbf{B}$ is related to the magnetic flux density, $\mathbf{H}$, by $\mathbf{D}(t) = [\mu(t)] * \mathbf{E}(t)$, where $[\mu(t)]$ is the permeability tensor.

For linear, isotropic and non-dispersive media the permittivity and permeability tensors reduce to scalar quantities, reducing Ampère's and Faraday's laws to:

$$\nabla \times \mathbf{H}(t) = \epsilon \frac{\partial \mathbf{E}(t)}{\partial t} \tag{3.19}$$

and

$$\nabla \times \mathbf{E}(t) = \mu \frac{\partial \mathbf{H}(t)}{\partial t}. \tag{3.20}$$

In terms of the central-difference approximation, these two equations show that, respectively, a circulating H-field induces a time-varying E-field at the centre of circulation (in proportion to the permittivity) and that a circulating E-field induces a time-varying H-field at the centre of circulation (proportional to the permeability). By offsetting the definitions of the $\mathbf{E}$ and $\mathbf{H}$-fields by half a timestep, the curl of the E-field can be used to calculate the H-field derivative half a timestep further along. Considering these equations in one-dimension, we can write:

$$\nabla \times \mathbf{H}(t) = \epsilon \frac{\mathbf{E}(t+\Delta t)-\mathbf{E}(t)}{\Delta t}, \tag{3.21}$$

and

$$\nabla \times \mathbf{E}(t) = \mu \frac{\mathbf{H}(t+\frac{\Delta t}{2})-\mathbf{H}(t-\frac{\Delta t}{2})}{\Delta t}. \tag{3.22}$$

To proceed further, this one-dimensional geometry is arbitrarily specified in Cartesian coordinates to only vary in the x-direction and the E-field is assumed to only have a component in the

z-direction. Using this definition we find

$$\nabla \times \mathbf{E}(t) = \begin{vmatrix} \hat{e}_x & \hat{e}_y & \hat{e}_z \\ \frac{\partial}{\partial x} & 0 & 0 \\ 0 & 0 & E_z \end{vmatrix} = -\hat{\mathbf{e}}_y \frac{\partial E_z}{\partial x}, \tag{3.23}$$

which means the only time-varying H-field component is in the y-direction, meaning $\nabla \times \mathbf{H}(t) = -\hat{\mathbf{e}}_z \frac{\partial H_y}{\partial x}$. The E-field is discretised on the integer spatial and temporal grid points and the H-field discretised halfway between each integer grid point. The sample spacings are Δx and Δt in space and time, respectively and the location of each sample point in space and time is notated by

$$E_z(x,t) = E_z(m\Delta_x, q\Delta_t) = E_z^q[m] \tag{3.24}$$

and

$$H_y(x,t) = H_y(m\Delta_x, q\Delta_t) = H_y^q[m]. \tag{3.25}$$

Indices m and q respectively denote the current spatial step and time step. Now rearranging both (3.21) and (3.22) and using the central-difference approximation, 3.18, we reach the following update equations for the H-field and E-field:

$$H_y^{q+\frac{1}{2}}\left[m+\frac{1}{2}\right] = H_y^{q-\frac{1}{2}}\left[m+\frac{1}{2}\right] + \frac{\Delta t}{\mu \Delta x}(E_z^q[m+1] - E_z^q[m]), \tag{3.26}$$

$$E_z^{q+1}[m] = E_z^q[m] + \frac{\Delta t}{\epsilon \Delta x}\left(H_y^{q+\frac{1}{2}}\left[m+\frac{1}{2}\right] + H_y^{q+\frac{1}{2}}\left[m-\frac{1}{2}\right]\right). \tag{3.27}$$

It is relatively straightforward to construct a numerical model using these two update equations in a 1D geometry. A guide to doing so, along with further considerations such as numerical stability, boundary conditions and translation to 2D and 3D, is found in [114].

3.4.4 FDTD in three-dimensions

Models in one-dimension are instructive in understanding the concept of FDTD; however, the PCBs described in this thesis (and, indeed, the vast majority of PCBs) require modelling in 3D in order for their behaviour to be fully understood. The 1D grid described in the previous section can be extended to three-dimensions with the same offset between E- and H-field samples in each axis. The resulting Yee lattice [115] is shown in figure 3.11. Electric field points are situated on the middle of the edges of the cube and magnetic field points are located at the centre of the faces of the cube, or vice versa. The electric and magnetic fields are evaluated at different time steps using a leapfrog method, whereby, for example, the future magnetic field is calculated using the finite difference method with the current local electric fields and the past magnetic field. The explicit time-stepping of the leapfrog method avoids the need to solve simultaneous equations and gives dissipation-free numerical wave propagation.

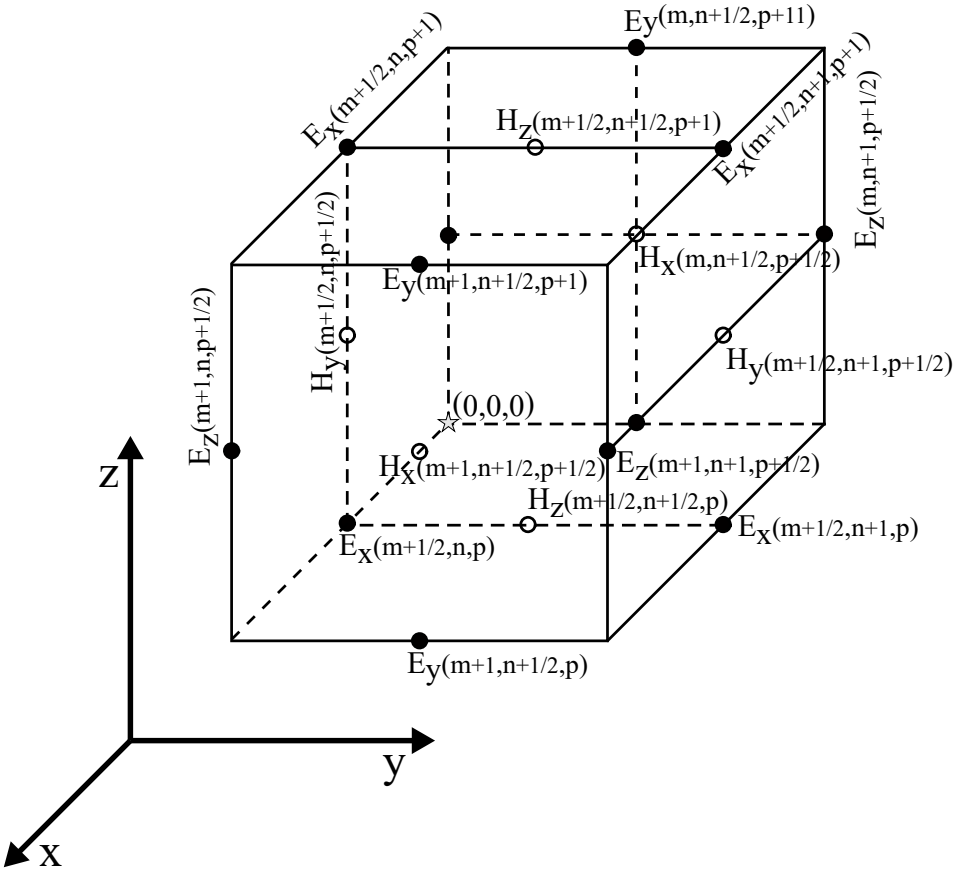

Figure 3.11: Diagram of the Yee cell with electric field components at the centre of the cell edges and the magnetic field components at the centre of each face. Each component's indices are in reference to the cell's origin at the back bottom left of the cube.

3.4.5 CST simulation process overview

The CST Studio Suite [116] affords a variety of solver methods, the simulation results in this thesis were exclusively obtained using the CST Microwave Studio subset. Within that subset, the Finite Integration Technique (FIT) is best suited for simulations over a broad frequency range, as after a single simulation all the required frequency responses are calculated by FFT. This method is paired with a hexahedral mesh, applied with an adaptive algorithm over features with varied dimensions. FIT simulations are stable provided the integration time step fulfills the Courant-Friedrichs-Lewy criterion, which depends on the minimum mesh cell dimensions: the higher the maximum mesh density, the smaller the maximum stable timestep becomes which increases simulation time. CST employs some further approximations, one being the Perfect Boundary Approximation to efficiently model irregular and curved surfaces within a hexahedral mesh.

Models are mostly excited by waveguide ports which simulate a waveguide of infinite length connected to the structure. This method allows excitation and absorption of energy to/from the simulation domain with very low levels of reflection. A 2D eigenmode solver is used to calculate the modes transmitted by the waveguide port, which depends on the transmission line structure bounded by the port. The CST documentation provides advice for the creation of waveguide ports for several types of common transmission line [116].

Chapter 4

Antennas

Any piece of conductor can, in principle, act as an antenna. The shape and size of this conductor are varied to control the frequency range the antenna can emit or receive and the direction in which it emits to or receives from. The selected antenna for Synthetic Aperture Microwave Imager-2 (SAMI-2) must be broadband, operational over at least 20-40 GHz; small in size, to enable as many as possible (at least 30) to fit in the 150 mm diameter port window; preferably dual-polarisation, to image both O- and X-mode, and have a shape to minimise reflections within the antenna array. This chapter describes the design and testing of one candidate, the sinuous antenna, and one back up, the Vivaldi antenna, with reference to the criteria outlined above and detailed in section 2.3.1 and Table 2.1.

4.1 Experimental setup

Here we describe the experimental set up used in this work for testing performance characteristics of antennas. All antenna measurements were performed in the anechoic chamber described in section 3.3.4. A cartoon diagram of a generic experiment is shown in figure 3.9. However, in most experiments described hereon the Vector Network analyser (VNA) is replaced by the HP 8564EC Spectrum Analyser, which measured received signals, while a separate synthesiser produced the signals to be emitted. A DP-241AC horn antenna from Flann Microwave is always "Antenna 2" in this diagram, which can be seen in the foreground of figure 3.10. We calibrated the experimental set up the devices under test (DUTs) by first using a horn antenna as the receiver. This provides a reference measurement for the power received by the spectrum analyser. In these initial experiments we do not care about phase, so do not need to use a VNA. In future we will measure the phase response of the SAMI-2 antennas, once they are integrated with the mixers, digitisation and acquisition subsystems, which measure phase information.

4.1.1 Frequency quadrupler power

The LMX2594 PLL synthesiser is used to produce signals which are fed into the AQA-2040 frequency quadrupler, then into the emitting horn antenna, via a short 40 GHz coaxial cable. The mean output power of this 20-40 GHz combined source is shown in figure 4.1, with standard deviations from three measurements, except for 12 of the 51 points which are from two measurements. The register values

for these points were not set properly by the SPI control of the LMX2594, due to a clocking issue which was since resolved. We see from this figure that the quadrupler's output power is reproducible within acceptable errors, especially above 27 GHz. We are unable to explain the larger errors under 27 GHz, further testing of the individual components is required to attribute these errors to a particular component, either the synthesiser or the frequency quadrupler. Furthermore, the minimum to maximum change in output power is reasonable, at 2.9 dB. This variation is reasonable and is sufficiently small for our experiments. For a larger variation, of 10 dB for example, we would begin to lose the lower power frequency signals in the spectrum analyser's noise floor, at the larger rotation angles in the forthcoming experiments. Unless otherwise stated, the LMX2594 always produced 51 frequency points every 100 MHz between 5-10 GHz. These are multiplied up by the quadrupler to give 51 points spaced every 400 MHz, between 20-40 GHz. Acquiring a set of these 51 frequency points takes almost exactly 5 minutes, so the resolutions of angular scans shown later are mostly limited to 1° or 2° steps. We set this limit partly because of the limited return for smaller resolutions and partly for brevity (keeping the longest scans under 12 hours so that two could be run each day). Aside from the frequency quadrupler and the Vivaldi measurements, all experimental data in this chapter was recorded within an 11 day period. Spurious harmonics were not investigated, as only the desired 4× frequency is measured on the spectrum analyser.

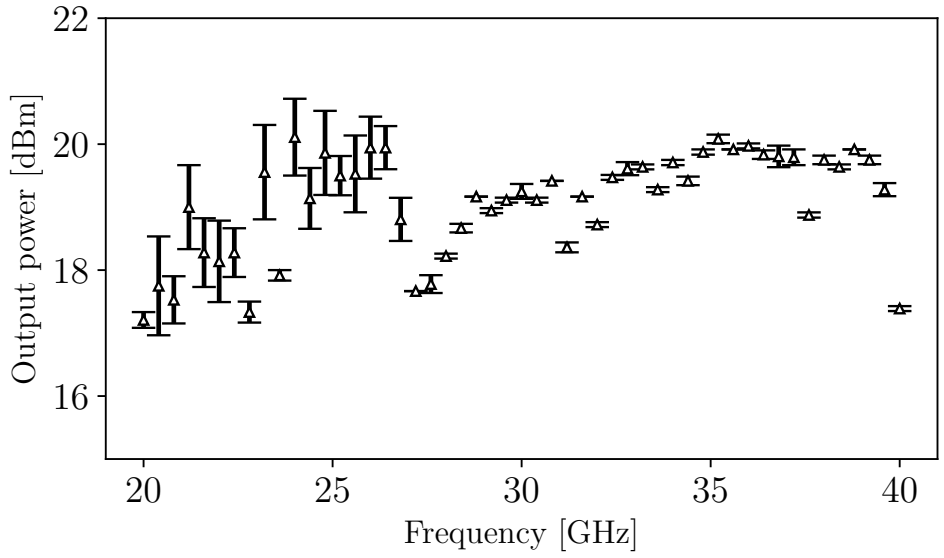

Figure 4.1: Frequency quadrupler output power over 20-40 GHz, fed by LMX2594. These points are the mean of three measurements, apart from 12 out of the 51 total, which are only from two measurements (due to a now resolved SPI clocking issue). The minimum to maximum variation is 2.9 dB between the minimum as 20 GHz and the maximum at 24 GHz. Its output power is acceptably flat and reproducible for use in the forthcoming anechoic chamber antenna measurements, as the frequencies at lowest power will not immediately fall below the noise floor of the spectrum analyser.

4.1.2 Friis gain equation

The Friis Transmission formula [89] for radiation of wavelength λ is

$$\frac{P_\mathrm{r}}{P_\mathrm{t}} = G_\mathrm{t} G_\mathrm{r} \left(\frac{\lambda}{4\pi R_\mathrm{sep}} \right)^2 , \tag{4.1}$$

where the received and transmitted powers P_r and P_t are in W on a linear scale. The factor $(\lambda/4\pi R)^2$ is the effective solid angle of the transmitter as seen by the receiver. It is a combination of the effective aperture of the antenna, $\lambda/4\pi$, and the inverse surface area of a sphere, $1/4\pi R^2$, where R is the sphere's radius and the distance between the two antennas. This effective aperture relation applies for aperture antennas, which radiate from a well defined area, or aperture. Equation 4.1 may be written in the logarithmic form

$$P_\mathrm{r} = P_\mathrm{t} + G_\mathrm{t} + G_\mathrm{r} + 20 \log_{10} \left(\frac{c}{4\pi R_\mathrm{sep} f} \right) , \tag{4.2}$$

where subscript r is the receiver and t is the transmitter, P is the power received or transmitted in dBm and G is the antenna gain in dB. As a calibration of sorts, identical standard horn antennas are used for the transmitter and receiver, meaning $G_\mathrm{t} = G_\mathrm{r}$. Transmitted power P_t is always fed into the same horn antenna from the LMX-quadrupler signal source, whose mean output power is shown in figure 4.1. Received power P_r is measured on a 40 GHz spectrum analyser, the HP 8564EC, and the gain of the horns calculated using (4.2). Following this, the receiver horn is replaced by a given DUT, a similar experiment performed and the gain of the DUT, G_r, calculated.

4.1.3 Reproducibility of fixed boresight measurements

The horn antennas used here are the DP-241AC from Flann Microwave, operational from 6-50 GHz and with dual perpendicular linear polarisations. To ascertain the reproducibility of the horn's emission pattern, power received by a second horn was measured several times for the two co-polarised pairs of ports on the two antennas. The cables were detached between each measurement to change polarisation. Some of the measurements were made on a different day, after the mounting apparatus for each horn had been disassembled and reassembled. The mean gains and standard deviations for these multiple runs are displayed in figure 4.2. The horns have ports nominally on their side (s) and top (t). The mean of top-port to top-port measurements 0, 1 and 2 is in black and mean side-to-side measurements are in orange and blue. Side measurement 0 (s0) significantly increases the standard deviations at several frequencies. The reason for this is unknown as s0 and s1 were automated repeat measurements, between which the experimental set up was untouched. We do not assign any importance to the difference of s0. We ran an additional two independent repeat measurements (s3 and s4) to improve confidence in the reproducibility of the horn side-port gain. The DP-241AC datasheet specifies a gain between 10-20 dBi, which our measurements match.

4.2 Vivaldi antennas

Eight broadband antipodal Vivaldi antennas were used on Synthetic Aperture Microwave Imager (SAMI), manufactured on 0.381 mm Rogers Duroid 5880 substrate, which operated over 10-

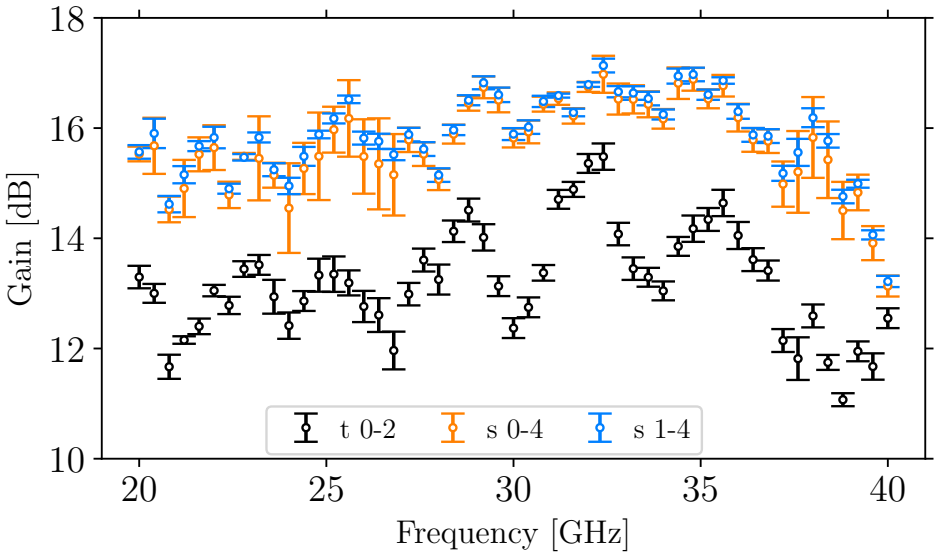

Figure 4.2: Co-polar horn-to-horn mean gains and errors for multiple independent measurements. "s" is the horn's side port, "t" is the top port. Although there is significant variation in horn gain with frequency, the variation is reproducible with acceptable errors. The cables were detached between each measurement, *except* between *s0* and *s1*. Somewhat inexplicably *s0* introduces the largest gain error of the five measurements; therefore, inclusive (orange) and exclusive (blue) sets of the side-to-side measurements are plotted to highlight its impact. Maximum standard deviations: top-to-top (black) 0.77 dB, side-to-side inclusive (orange) 1.65 dB, *s* exclusive (blue) 0.53 dB. Minimum to maximum gains: top (black) 8.8 dB, side-inclusive (orange) 7.7 dB, side-exclusive (blue) 7.8 dB. Errors in frequency are too small to be visible: a third of points had a frequency error, the largest being ±1.2 MHz and all other errors are below ±0.2 MHz.

35.5 GHz [78]. Eurocircuits instead have Rogers 4350B in their RF-pool and Garner Osborne do not stock Duroid 5880. Therefore, the design was modified for Rogers 4350B of 0.25 mm thickness. Additional modifications were made to extend the frequency range up to 40 GHz while removing the unnecessary capability below 20 GHz. Figure 3.3 exhibits the copper layers and some design parameters of the Vivaldi copper shapes on a two layer printed circuit board (PCB). The full list of design parameters on Rogers 4350B 0.25 mm is given in Table 4.1. Several of these parameters are used in equation 3.4 to set the flare openings and the rest are labelled in figure 3.3. We simulated both original and modified designs in CST and found that the performance on 4350B was not significantly worse. Consequently, we had a set of Vivaldis manufactured on 4350B by Garner Osborne.

We tested our Rogers 4350B Vivaldi antenna in the anechoic chamber, separated from the emitting horn by 60 cm. A comparison of the measured and simulated boresight gains (co-polarised) is shown in figure 4.3. The experimental gain is the mean of three repeat measurements, between which the maximum standard deviation is 0.5 dB and the mean is 0.1 dB, showing good reproducibility. Its minimum to maximum gain variation is 4.5 dB, which is reasonable over an octave at these frequencies. This figure also shows the polarisation separation (PS) of the antenna (in

Parameter	Value [mm]
Microstrip track width W_{MS}	0.53
Taper start x_{taper}	12.0
Balanced microstrip width W_{SYM}	0.74
Taper end, semicircle centre x_{Rcentre}	15.0
Semicircle radius R	6.63
Flare start x_{flare}	17.0
Flare opening parameter T [mm^{-1}]	0.1488
Constant c_1	6.275×10^{-4}
Constant c_2	-0.38
Slot width W	8.0
Edge metallisation width D	3.0

Table 4.1: Design parameters of the 20-40 GHz Vivaldi antenna described in this section, manufactured on Rogers 4350B 0.25 mm. Several of the parameters are labelled on figure 3.3 which shows the PCB layout of the antenna.

blue), calculated by subtracting the cross-polarised gain from the co-polarised gain. For our Vivaldi antenna the PS is mostly above the design target of 10 dB, the minimum is 8.0 dB and the mean is 15.7 dB.

We designed these Vivaldi antennas as a reserve option, in case the sinuous antennas did not perform well enough. As discussed in section 1.11.2, the 3D shape and single polarisation capability of the SAMI Vivaldi antennas produced non-negligible uncertainties in the measured data. In section 4.7, we conclude that the sinuous antenna has fulfilled most of the optimal design criteria and therefore does perform well enough for use in the SAMI-2. As a result and in the interest of time management, we did not measure the full Vivaldi emission pattern, leaving it for further work.

4.3 Dual-polarisation sinuous antennas

A dual-polarisation sinuous antenna was designed using the process described in section 3.2.2: the maximum and minimum wavelength relations (3.8) and (3.9) were used first to find the minimum outer radius, R_0, to be able to operate down to 20 GHz and then to calculate the cell number p and expansion factor τ to produce an inner radius capable of responding to 40 GHz waves.

4.4 In-plane feed design

As the desired upper frequency of operation increases, the central area in which to connect the antenna arms to a feed network decreases. For a maximum frequency of 40 GHz and free space wavelength 7.5 mm, the corresponding inner sinuous radius is 0.64 mm, in the diagram in figure 3.4, for $\tau = 0.77$, and $R_0 = 6.75$ mm. For dual-linearly polarised emission opposite pairs of arms must be connected to the same feed. Together, these opposing arms produce balanced signals which need to be converted to unbalanced signals for transmission on most conventional transmission lines, such as coaxial cables, microstrip and grounded co-planar waveguide. A simple way to achieve this is by connecting one arm to ground and the other to the signal conductor. This is described in more detail in section 4.5. Due to the interleaved arms there is little space to route conductors in

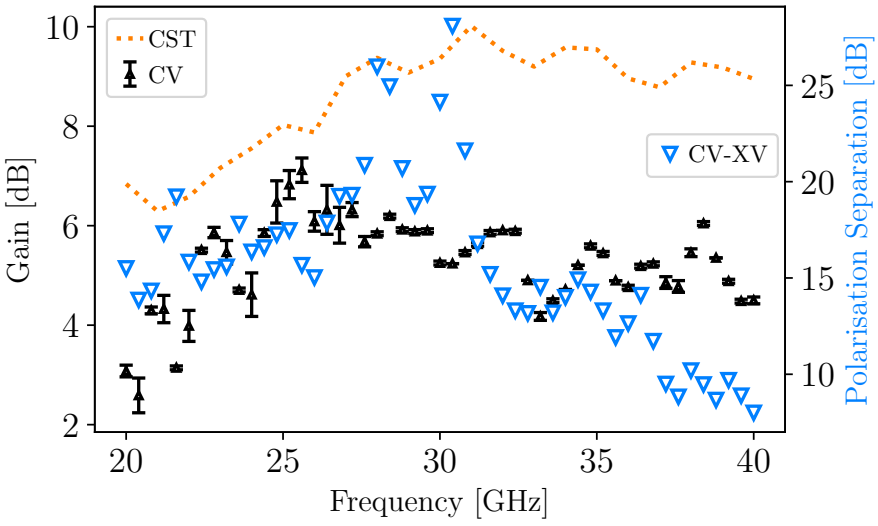

Figure 4.3: Mean experimentally measured boresight gain of the Vivaldi antenna from three tests (CV, black), compared against the simulated boresight gain (CST, orange). The measured minimum to maximum gain variation is 4.5 dB and the shape largely, and qualitatively, matches simulation. Polarisation separation is also included on the right hand vertical axis (CV − XV, blue) and is mostly above the 10 dB target.

the plane of the antenna, although this feed solution has been implemented [105]. Perpendicular feeds are more common, such as the coaxial feed lines orthogonal to the antenna plane employed by Edwards et al. in their 6-24 GHz scaled design. Perpendicular microstrip balun feeds [99, 103, 106, 117] replace the coaxial cables with transmission lines on a PCB connected to the antenna centre, which may be manufactured on the same substrate as the antenna.

The in-plane antenna feed design may begin once the required inner antenna diameter is found and the balun method chosen, which influences the finishing location of the in-plane feed. We chose dual-polarisation microstrip baluns to feed the antenna through a slot cutout at the centre. Using (3.9) we found that a maximum inner cell radius of 0.8 mm is required to see 40 GHz, allowing for a transition region between the arms and the in-plane feed. From the relation $R_{\text{min}} = \tau^p R_0$, where $\tau = 0.77$ and $R_0 = 6.75$ mm, each arm must contain 8.2 cells, p, rounded to nine. The smallest radius of the ninth cell comes out to be 0.64 mm. This leaves a circle of that radius at the antenna centre, in which to place the in-plane feeds and connect them to the four balun tips.

We produced a preliminary design by extending tracks from each antenna arm to the balun-tip locations at the cutout slot, using the narrow end width between the pairs of swept log-periodic curves, of under 0.1 mm (produced with (3.6)). Significant efforts were made to length match all four in-plane extended feeds, by solving for coefficients of several trigonometric curves to retain the same track width as well as length. The goal of this process was to minimise phase misalignment with incoming signals and between antenna polarisations. Due to the narrow conductor width, the resulting feed has higher impedance than the bulk antenna. This high impedance in-plane feed had a poor match to the balun and to the antenna, giving poor results. A subsequent feed design was constructed without the unnecessary four-way length matching constraint, with the aim of keeping

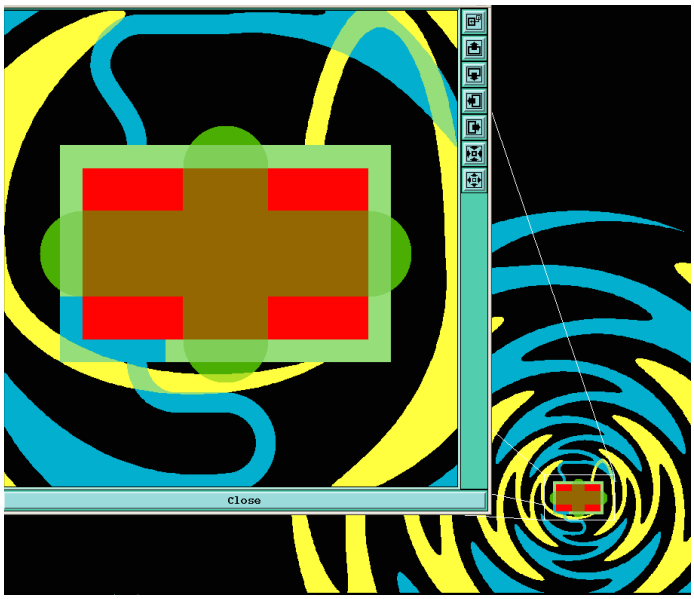

Figure 4.4: Close up of our original sinuous antenna feed, blue denotes one polarisation and yellow the orthogonal polarisation, situated on the other side of the substrate. The red rectangle highlights the central cutout slot which is internally plated, with surrounding copper annuli on both sides of the substrate. Green rounded rectangles show two intersecting paths followed by the 0.3 mm router to break the electrical connection between each of the four arms. This layout was superseded by the design used in the experiments in this chapter.

impedance changes smooth and keeping the in-plane feed as simple as possible. Results for antennas with this latest feed design are presented hereon.

From our discussions with the manufacturer, Garner Osborne, Rogers 4003C 0.203 mm thickness was chosen for its relatively low dielectric constant, 3.55, up to 40 GHz and constant availability in stock. Simultaneously making and retaining connections between the four antenna arms and four balun tips in this way is very challenging. It is made especially challenging after cascading manufacturing tolerances together, which have the largest impact on very narrow copper tracks. To aid these connections the central antenna slot was redesigned to be internally plated, after we visited the manufacturer. To aid the plating a thin annulus was left around the lip of the plated slot, on both sides of the substrate. Once plated, the four arms are shorted together and need to be separated electrically. A 0.3 mm router bit was dropped into the slot, after plating, to break the connection between the four arms. It followed the two green, rounded rectangular straight paths, shown in figure 4.4 and overlaid on the initial dual-polarisation feed. The resulting four notches are small enough such that the central balun crenellation fits in accurately, along with two outer locating crenellations.

In CST Studio, the antenna was simulated on Rogers 4003C 0.203 mm thickness in isolation by excitation with discrete ports (thin wires) between the arms of each polarisation over 20-40 GHz. These emulate excitation by the two balanced balun terminals by providing a current source at a specified reference impedance. CST calculates the impedance of the connected structure, seen the discrete port, by measuring the power reflected back into the port. Here we chose 150 Ω as the reference impedance for both ports. Figure 4.5 displays the impedance of each orthogonal

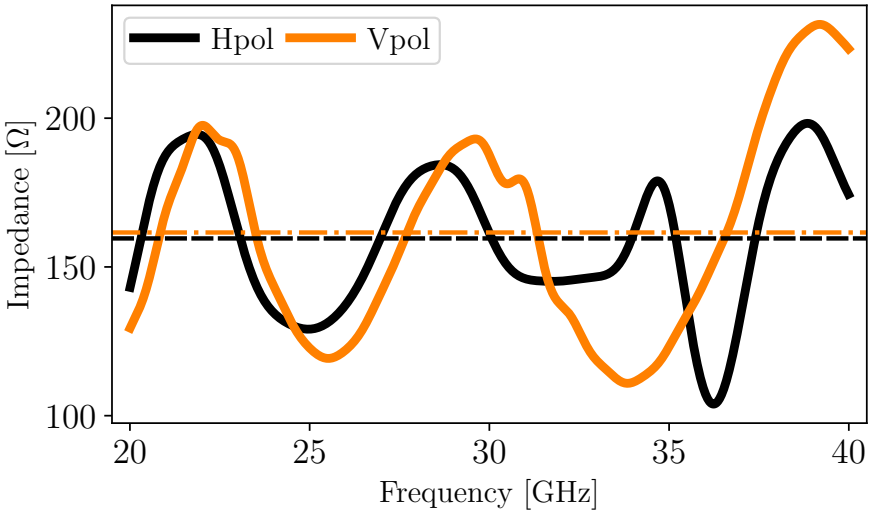

Figure 4.5: Impedance of both sinuous antenna polarisations over 20-40 GHz, simulated in CST Studio. The mean impedances are marked by dashed and dash-dotted lines of the same two colours for the respective polarisations, calculated as 159.6 Ω for the horizontal (black) and 161.6 Ω for the vertical (orange) polarisation.

polarisation as measured by the discrete ports; the horizontal polarisation is shown by the solid black line and the vertical polarisation by the solid orange line. The mean impedance of the horizontal polarisation is 159.6 Ω, marked by the dash-dotted orange line, and the black dashed line at 161.6 Ω gives the mean impedance of the vertical polarisation. For simplicity, both of these values are rounded to 160 Ω for the design of the balun taper, in section 4.5.

4.5 Balun design

A balun is required to feed the sinuous antenna, which must convert an unbalanced signal at the balun input to a balanced signal at the antenna end, as described in section 3.2.3. Bounding the balun design is the impedance of the antenna feed (Z_2) on one end and standard 50 Ω (Z_1) transmission line impedance on the other. The balun should vary in impedance by tapering to provide a match at both ends. We calculated a Klopfenstein taper [111], using the equations in section 3.2.4, to find the optimum taper between these two impedances in the space available. There will be two mirrored baluns on the same PCB to serve both polarisations of the sinuous antenna.

The locations of the antenna's in-plane feed ends dictate where the high impedance end of the balun should finish. Given that the central slot is 1 mm wide, the balun's two pairs of balanced, high impedance tracks will need to be brought inwards to within this 1 mm width at the central tip of the balun. At the low impedance end, the choice of connector imposes a minimum spacing between the balun for each orthogonal antenna polarisation. This connector choice is detailed in section 5.4, in which we select the Narrow Body 2.92 mm connector from With-Wave. We accounted for the width of this connector, along with an estimate of the additional space required for a spanner to fit between the two connectors, and calculated a pin-to-pin spacing between the two connectors of

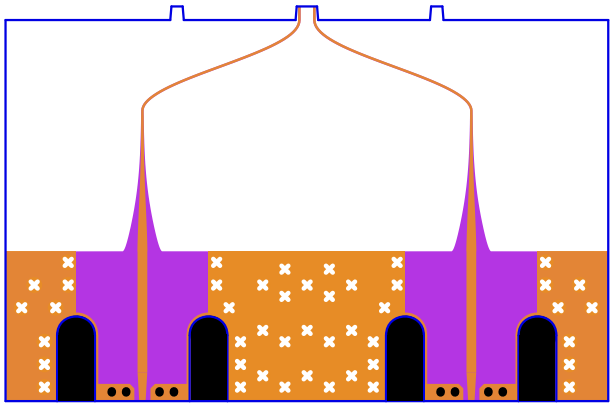

Figure 4.6: Dual-polarisation microstrip balun artwork as manufactured on Rogers 4003C, thickness 0.203 mm. The top copper layer is orange, bottom copper is purple and the connector launch vias are black filled circles. The connector plated mount slots are black rounded rectangles, white crosses denote 0.3 mm diameter grounding via locations and blue lines outline the PCB. Its width is 26.6 mm and its length is 17.4 mm, including the 0.6 mm crenellations.

14.5 mm.

Using the suggested microstrip launch in the component datasheet [118], we designed the low impedance balun end for 0.203 mm Rogers 4003C, with a 50 Ω track width of 0.43 mm. We also included a short linear taper close to the connector pin flanked by narrow copper sections grounded with two 0.25 mm vias. These vias aid the transition from the connector mode to the microstrip mode. To calculate the width of the balanced end, we solved (3.3) for the chosen impedance, $Z_2 = 160\,\Omega$ by finding its root for a microstrip track of impedance $Z_2/2$, with a Perfect Electric Wall acting as a ground plane situated at the centre of the substrate, as described in section 3.2.5. Due to the symmetric dimensions of the tracks at the balanced end, the combined field pattern is also symmetric about the parallel plane through the origin (occupied in the calculation by the infinite ground plane). The impedance is double that of a single microstrip line situated above a ground plane through the origin. Using these bounding track widths, we designed a Klopfenstein taper to transition between them.

The artwork for one dual-polarisation balun is shown in Figure 4.6. The two signal tracks transitioning from microstrip to balanced microstrip, nominally on the front side, are shown in orange along with co-planar ground sections adjacent to the connector bodies. The purple back layer incorporates the microstrip ground plane, stitched to the front side ground sections with 0.3 mm diameter vias denoted by white crosses. Pairs of 0.25 mm vias straddle the connector pin, as suggested in the connector datasheet. For ease of mounting the With Wave connectors, we included plated edge slots, shown filled with rounded black rectangles.

4.5.1 End-to-end simulations

To design and test a device such as this impedance transforming balun, with a non standard impedance at one of the ports, the structure can be mirrored. We mirrored the copper artwork

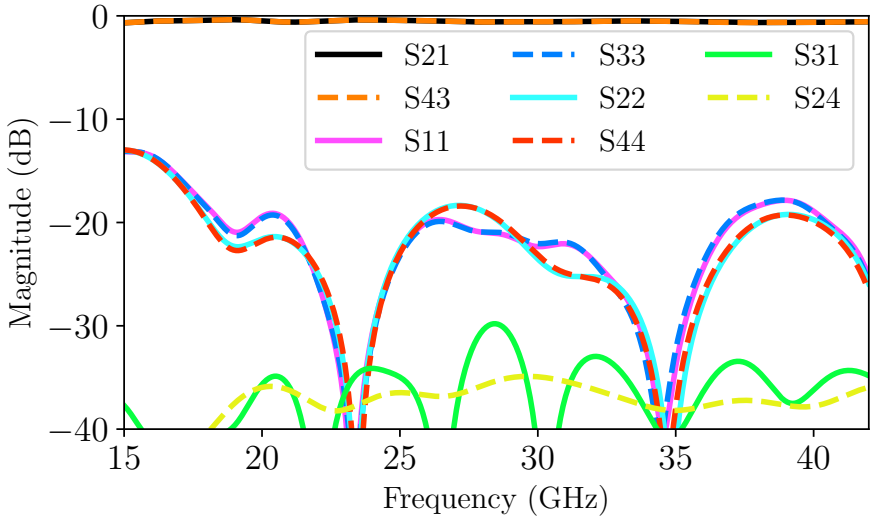

Figure 4.7: Simulated S-parameters for the end-to-end dual-polarisation balun over 15-42 GHz, the model is a duplicated mirrored version of Figure 4.6 on lossy Rogers 4003C of 0.203 mm thickness. Port 1 connects to port 2, and port 3 transmits to port 4. In the 20-40 GHz region of interest: transmission, S21 (black) and S43 (orange), is all better than −0.7 dB and maximum return loss of all four ports is −17.8 dB. The worst leakage (S32 and S24) between baluns is −29.8 dB.

in the line directly adjacent to the end of the tips of the balun's crenellations, along the top edge of Figure 4.6. This results in a "balunbal" which converts from 50 Ω unbalanced to 150 Ω unbalanced and then back to 50 Ω unbalanced. As a result, we are able to attach 2.92 mm end-launch connectors to either end, which will enable us to measure the S-parameters of the end-to-end balun.

Prior to manufacture we simulated the end-to-end balun in CST, giving the results in figure 4.7. The substrate material is 0.203 mm lossy Rogers 4003C and the two pairs of ports are excited by waveguide ports between 15-42 GHz (although here we focus on 20-40 GHz). In the desired frequency range the end-to-end balun exhibits low loss, as transmission between electrically connected ports is all above −0.7 dB, lines S21 and S43 (and by reciprocity S12 and S34). Correspondingly, return loss into all four ports is below −17.8 dB. Although the balanced microstrip balun ends come within under 0.6 mm of each other, cross-talk between baluns (S32 and S24) is never above −29.8 dB over the frequency range of interest.

Although several end-to-end baluns have been manufactured, we leave the experimental testing of the balun for further work. As we discuss in the next section, the sinuous antenna achieves most of the optimal criteria for the SAMI-2 antenna. The balun is an integral part of the sinuous antenna. Therefore, we know that it performs well enough for our purpose, although its performance is still worth measuring. This is because by comparing its real performance to its simulated performance, we may be able to improve the balun's design, and consequently the sinuous antenna performance, for a future iteration of the SAMI-2 array.

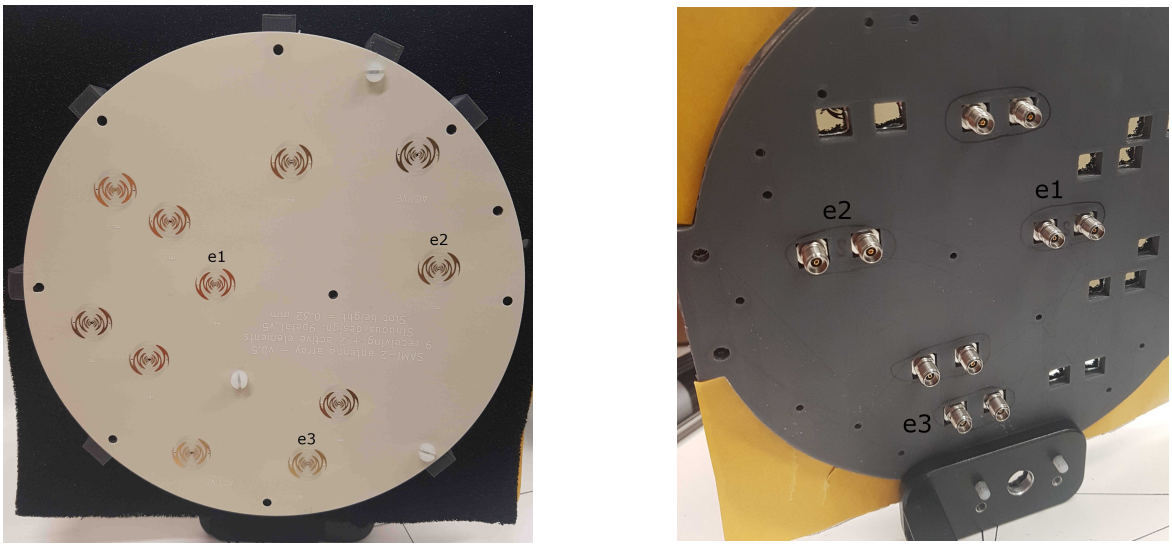

(a) Front. (b) Back.

Figure 4.8: Photographs of the 11 antenna array tested in this chapter. The array substrate disk is mounted on support struts from a 3D printed backing plate (dark grey). With Wave 2.92 mm connectors are supported by the bulkhead to remove stress from the fragile antenna-balun interconnection. Labels 'e1', 'e2' and 'e3' mark the three sinuous antennas whose test results are reported here.

4.6 Sinuous antenna-balun results

4.6.1 Array construction and mounting

An 11 antenna test array and baluns were fabricated by Garner Osborne. The antenna-balun interface is fragile and requires support. We designed a 3D printed bulkhead support structure for this purpose. This is the grey plastic seen most clearly in figure 4.8b. Rectangular holes hold the With Wave connectors on each balun, which are heavy enough to jeopardise the integrity of the antenna-balun connection without support. Several struts support the array disk, three are connected to it by the white plastic screws which can be seen in figure 4.8a. Elements 1, 2 and 3 are labelled in both of these figures as 'e1', 'e2' and 'e3'. The baluns sit in the air gap between the bulkhead and the substrate. We covered the front face of the bulkhead with microwave absorbing foam, backed with foil (which extends superfluously in a square around the array in these photos, and was trimmed down before testing). The bulkhead has screw holes allowing the array to be mounted on a rotating tripod.

4.6.2 Reproducibility

We tested the sinuous gain measurement's reproducibility by measuring the received power on boresight multiple times independently, by detaching the cables between measurements. The means and standard deviations from repeat measurements of both sinuous polarisations are plotted in figure 4.9. The mean of two co-polar measurements of the horizontal sinuous polarisation (H) are in black and the mean of three vertical polarisation (V) datasets are in orange.

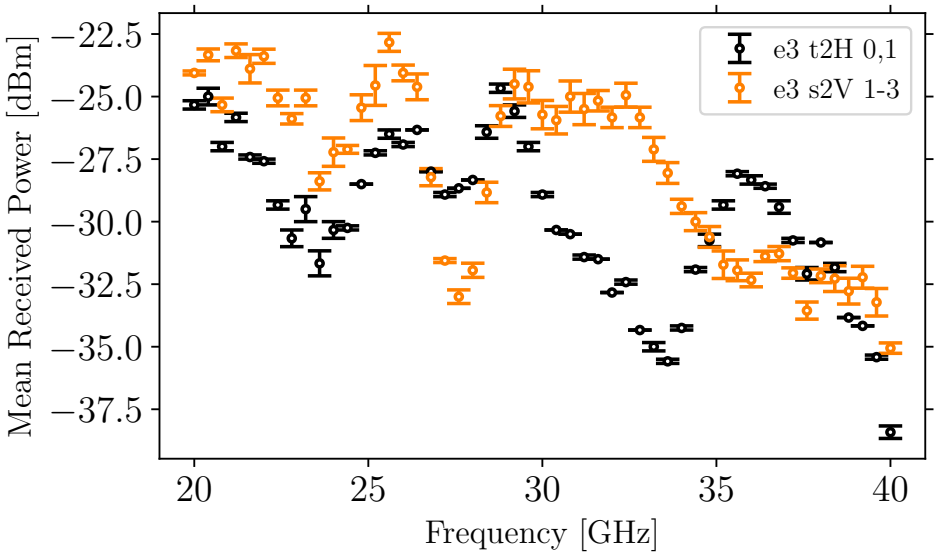

Figure 4.9: Mean received powers and errors for multiple independent measurements for each polarisation of element 3 (e3). We detached the cables and changed the connected antenna polarisation between each measurement. Maximum to minimum variation for top-to-Horizontal (H) polarisation (black) is 13.8 dB and for side-to-Vertical (V) polarisation is 12.2 dB. Maximum errors in received power are 0.5 dB for (H) and 0.80 dB for (V). Errors in frequency are too small to be visible, with the largest being ±0.3 MHz.

4.6.3 Polarisation wobble

Due to the sinuous antenna's sinusoidal shape, the polarisation angle at which maximum power is received by the antenna varies with frequency. To measure this, we rotated the antennas about their boresight axis and measured the power received at each angle, from which the realised gain was calculated using equation 4.2. The sinuous antenna design parameter opening angle δ is 22.5°, so we do not present data for rotations much larger than that, positively or negatively with respect to its origin (at zero degrees). The maximum magnitude boresight rotation presented here is 40°. We did perform rotations up to 90°, but as the angle increases above 40° this simply tended to a cross-polar measurement, as the emitting horn's polarisation remained unchanged.

We rotated three sinuous antennas, labelled elements 1, 2 and 3 (or e1, e2 and e3), about their boresight to locate the angle of maximum gain for each frequency. The same horn antenna was used as the emitter in all experiments, located 100 cm from the antenna under test in the anechoic chamber. Figure 4.10 shows the power received by element 3 over frequency and rotation angle, normalised to the maximum value at each frequency. Locations of these maxima, at 0 dB, are in white. There are multiple maxima at some frequencies because the spectrum analyser (HP 8564EC) has finite resolution and there are multiple angles with a received power within the power resolution increment. The HP 8564EC has a power resolution of 0.17 dBm in the acquisition mode used for these experiments.

Using the received power maxima in figure 4.10, we calculated the adjusted boresight gain of the horizontal sinuous antenna. This is the gain adjusted for its polarisation wobble, and we performed

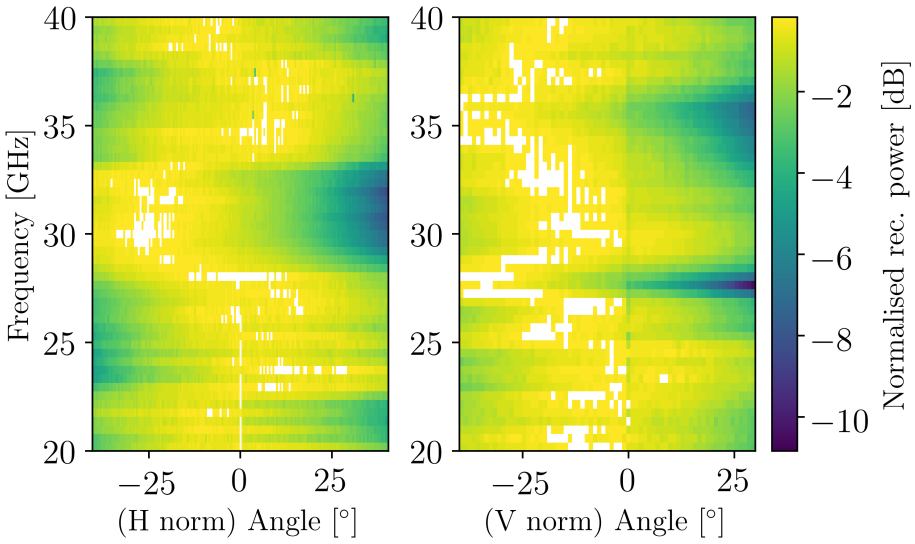

Figure 4.10: Normalised received power comparison between sinuous Horizontal (H) polarisation and Vertical (V) polarisation of element 3, over boresight-rotation angle and frequency. Power at each frequency normalised to the maximum value over angle at that frequency, to remove any frequency dependence in the colour map. White highlights angles of maximum received power at a given frequency. This shows that the optimum polarisation of the sinuous antenna varies with frequency, as expected.

the adjustment separately for each sinuous polarisation. For the horizontal polarisation of element 3 the gain at 0° is compared to the maximum gains at each frequency in figure 4.11. The largest difference between the 0° gain and the maximum is 1.33 dB. A similar comparison for the vertical polarisation is shown in figure 4.12, where the greatest difference is 3.33 dB between the gain at 0° and the maximum. Given that the difference in received power, from 0° orientation to the maximum, is not massive and is reproducible, we can account for it in the array image inversion algorithm. Synthetic aperture imaging relies on the accurate measurement of phase differences between array elements and the phase being independent of the signal power.

The rotating mount could not always rotate the sinuous antenna under test precisely about its boresight axis. In each experiment we positioned the array in such a way as to minimise linear offsets introduced by the rotation. Here we will refer to rotation angles, ρ, the extent to which we deliberately rotated the test antenna about its boresight axis, and maximum displacement angles, δ_i, arising from these unavoidable linear offsets during the rotations. We calculate $\delta_{1,2,3}$ for the three elements, relative to the horn antenna, for the maximum $\rho = \pm 40°$, used here. Element 2 has a maximum displacement angle of $\delta_2 = 2°$, while $\delta_{1,3}$, for e1 and e3, are under 0.7°. This means that at $\rho = 40°$ rotation about the boresight axis, e2 has moved 2° away from the boresight axis, relative to the emitting horn (displaced by $\delta_2 = 2°$). Figure 4.13 shows the mean resulting gain difference at both $\delta_2 = \pm 2°$ (black triangles) from the horn boresight in the altitude plane. These gain differences are relative to the horn's boresight gain. There is almost no detrimental effect to e2 moving by 2° relative to the horn. In fact, at several frequencies the gain is higher at this small angle away from boresight. Similarly, the negative maximum displacement ($\delta_2 = -2°$) will be reached when e2 is rotated to the $\rho = -40°$ point. Gain differences at $\delta_2 = \pm 2°$ are very similar, so the error bars

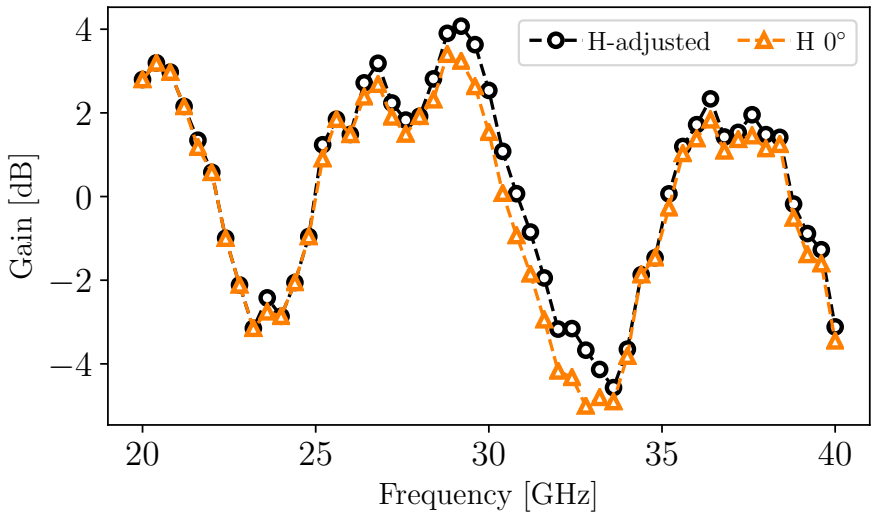

Figure 4.11: Sinuous antenna element 3 horizontal polarisation adjusted and unadjusted boresight gains, plotted over frequency. We calculated the adjusted gain (black circles) using the maximum values at each frequency, highlighted in white in figure 4.10 (H). The largest adjustment is 1.33 dB.

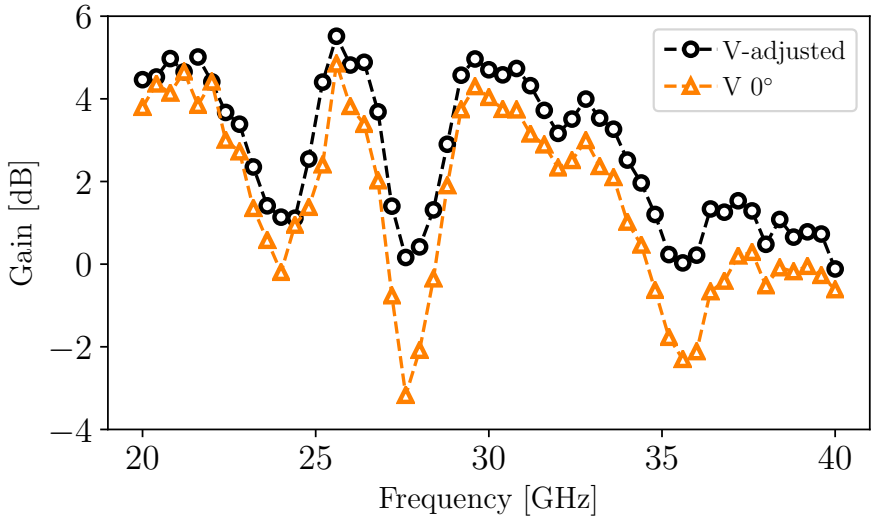

Figure 4.12: Sinuous antenna element 3 vertical polarisation adjusted and unadjusted boresight gains, plotted over frequency. We calculated the maximum gain (black circles) using the values highlighted in white in figure 4.10 (V) at each frequency. The unadjusted, 0° gain (orange triangles) is calculated with the received powers at that fixed angle. Here, the largest adjustment is 3.33 dB.

are too small to see. The mean error between the gain differences at $\pm\delta_2$ is 0.04 dB. As an aside, this shows that the horn emission pattern is slightly annular about the boresight (we see a similar pattern in the azimuthal plane).

In this horn gain deviation measurement, the peak gain difference of nearly 2 dB, at 25 GHz, is not negligible. However, this is the maximum difference seen by any of the three elements in all of the polarisation wobble experiments. This may account for why we see maximum received powers above 22.5° rotation at some frequencies in figure 4.10, mainly in the vertical sinuous polarisation data. We will not correct for this error here. However, if, say, we applied a linearly increasing error as rotation angle gets further from zero, this would enhance the central columns in figure 4.10 and make the wobble more pronounced.

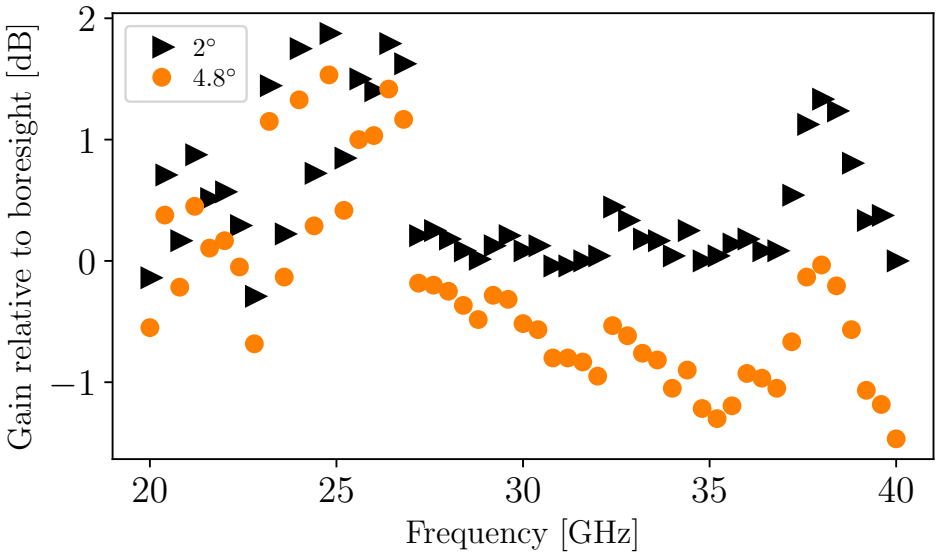

Figure 4.13: Horn gain deviation at 4.8° (orange circles) and the mean of angles ±2° (black triangles), in the altitude plane relative to boresight. A negative gain difference signifies a lower gain at that angle than on boresight and vice versa for a positive gain difference. These gain differences contribute to uncertainty in sinuous antenna results presented here and will be referred back to.

4.6.4 Experimental and simulated gains

Now we have adjusted the sinuous boresight gain for the three array elements, we may compare it to the simulated sinuous gain from CST. We built a model of a single dual-polarisation sinuous antenna and feed network in CST, from the Gerber files used to manufacture the array and baluns. This model is shown in figure 4.14. The inbuilt library model of lossy Rogers 4003C material was used for the antenna and balun substrate. We set up two waveguide ports to stimulate the system from the microstrip ends of the balun over 20-40 GHz and used open boundaries, with additional space between the structure and the boundaries. To more effectively model the real antenna, we included foil-backed absorbing foam and a PLA plastic backing. These are the same thicknesses as used in the array mount (figure 4.8) and their dielectric properties were chosen to try to match the real materials as closely as possible. We selected CST's time domain solver to calculate the propagation

of these stimulated signals throughout the structure, using a method based on 3D finite-difference time-domain (FDTD) (briefly described in section 3.4.4). CST calculates the antenna's far-field emission pattern at a sufficient distance from the radiator, relative to the wavelength, that the waves are approximately spherical.

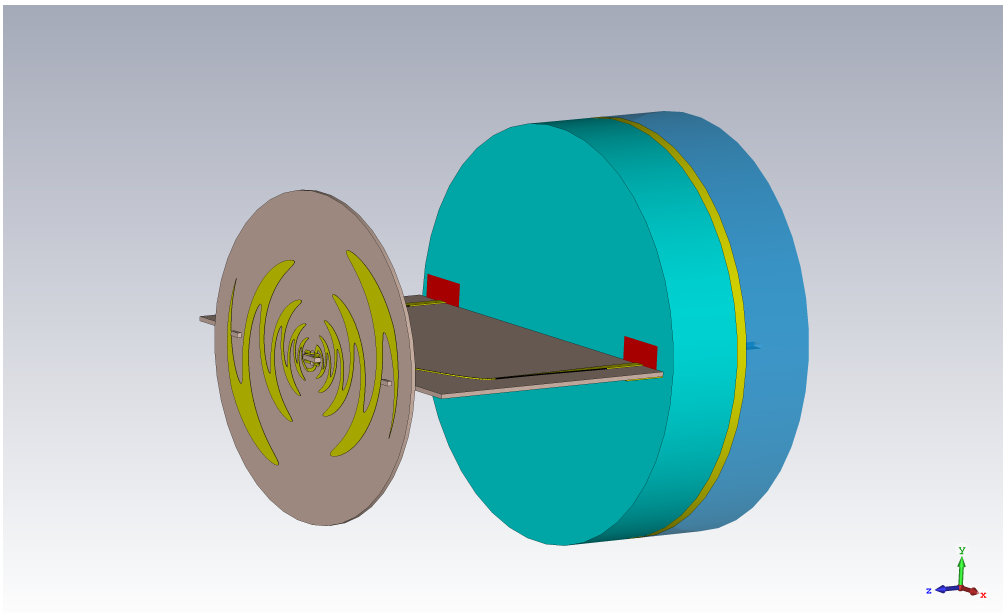

,

Figure 4.14: Screenshot of the sinuous antenna CST simulation geometry. The antenna disk is on the left hand side, joined perpendicular to the balun. The two red rectangles are waveguide ports which stimulate and measure power at the baluns two 50 Ω ports. The three disks on the right side are microwave absorbing foam (light blue), gold foil (yellow) and PLA (dark blue).

For the three tested sinuous array elements we compare simulated far-field boresight gain with the adjusted measured boresight gains. Figure 4.15 shows the horizontal polarisation (H) and figure 4.16 displays simulation and experimental data for the vertical polarisation (V). There is generally good agreement between the horizontal polarisations, save for the larger fall in e1's gain at 33 GHz. This shows that H can be manufactured to have reproducible performance. Beginning at low frequency, the first trough and first two peaks in measured gain follow the simulation well in form, if not in absolute terms. From 30 GHz upwards the shape is still similar, but the next trough and peak arrive at lower frequency in experiment than in simulation. Analysing the precise reasons for the absolute gain difference and this divergence is not within the scope of this thesis, though we will now discuss some potential factors.

Differences between the designed copper shape (simulated) and the manufactured copper shape (experimentally tested) have a greater effect at these millimetre wave frequencies, compared to lower frequencies. The narrowest track in this design is the minimum track width Garner Osborne can route. Furthermore, the routing tolerance introduces a 100% uncertainty on the narrowest tracks as compared to the model. This will impact the feed's impedance matching and, consequently, the performance. In addition, there are tolerances on hole cutting and plating. At the plated slot connection, these tolerances introduce differences between the modelled and the manufactured antenna-balun interface. These differences further compound the variation of the impedance match-

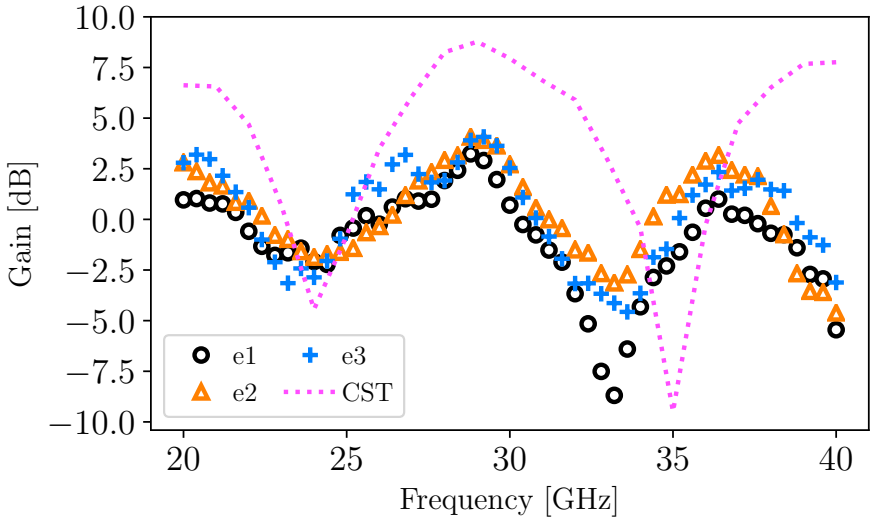

Figure 4.15: Adjusted boresight gains for the horizontal polarisation of the three sinuous array elements compared to the simulated realised gain (pink dashed). The measured and simulated gains generally follow similar variations, apart from a difference in peak gain and a frequency offset of the minimum gain, at 35 GHz. We see well matched performance between the different elements, with the largest discrepancy at the trough at roughly 33 GHz.

ing of the feed, compared to the ideal model. The gain frequency divergence indicates that the CST material model of Rogers 4003C does not match the real material performance above 30 GHz. Permittivity and loss tangent values for this material (and the majority of materials we looked at) are defined at a maximum frequency of 10 GHz in their datasheets, and correspondingly in CST. Divergence between CST and measured performance at higher frequencies, over an octave higher here, is therefore not unrealistic. This difference in frequency scaling is not seen in the vertical polarisation (V) results, in figure 4.16. This may be due to the fact that there are no clear resonances for V. The resonances in the boresight H gain may be caused by destructive interference as a result of impedance mismatches. Accurately modelling the resonant frequency requires the wave propagation in the substrate to be exactly correct. Nevertheless, there is good agreement between the experimental and simulated gain profile over frequency for the vertical polarisation, aside from the measured peak just above 25 GHz. The main issue with these results are the large differences between the performance of elements 1, 2 and 3. One potential reason is that the balun-antenna solder connection of e1 and e2 was found to have broken part way through the testing. At this point we changed the DUT (very carefully) to e3 and bound the connected coaxial cable to part of the rotating support to reduce torques and stresses applied to the balun-antenna solder joints. We recorded H data before that of the V data for these experiments. It is possible the joints of e1 and e2 were compromised by stresses in the H experiment before the vertical polarisation was measured. This would explain the large discrepancies between the measured gains of the three V polarisations. Further testing of other array elements is required to confirm or invalidate this hypothesis.

Next, we take the mean and standard deviation of the adjusted boresight gains of the three array elements (e1, e2 and e3) in figures 4.15 and 4.16, and plot them for both polarisations along

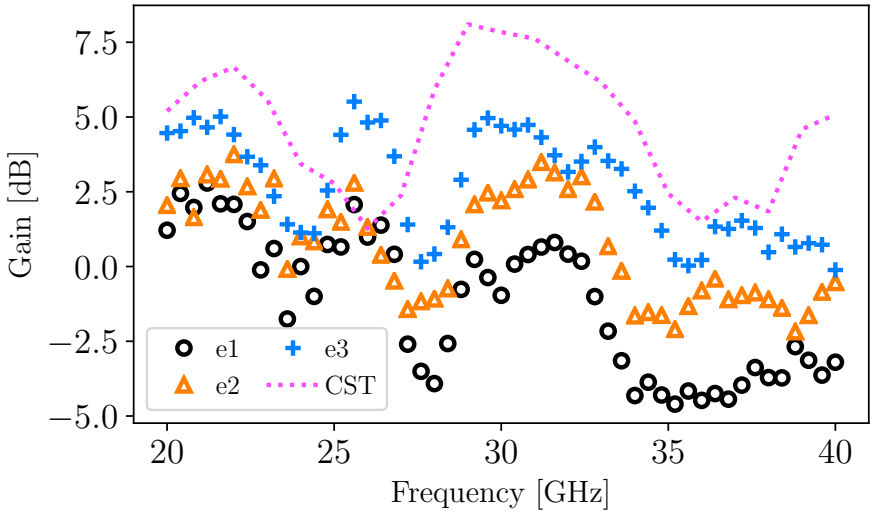

Figure 4.16: Comparison of the simulated realised gain (pink dashed) to the adjusted boresight gains, for the vertical polarisation of the three sinuous array elements (e1, e2 & e3). We see generally the same form in the measured and simulated gains, except for the peak in measured gain at about 26 GHz. The vertical sinuous polarisation has markedly greater variation between elements than the horizontal.

with simulated gains in figure 4.17. The minimum to maximum variation between the three array elements' horizontal polarisation is 9.1 dB and 5.7 dB for their vertical polarisation. For their standard deviations we find the maximum to be 2.4 dB (H) and 2.8 dB (V), the minimum is 0.2 dB (H) and 0.5 dB (V) and the mean is 0.9 dB (H) and 1.7 dB (V).

Element 1 has the worst performance of the three. If we remove it from the averaging, the minimum to maximum variations become 7.9 dB in the horizontal data and 5.1 dB in the vertical data. Similarly, if e1 is removed the standard deviation has the following values: the maximum is 1.3 dB (H) and 2.3 dB (V), the minimum is 0.0 dB (H) and 0.1 dB (V) and the mean is 0.6 dB (H) and 1.0 dB (V). Even including e1 the mean deviation for (H) is sufficiently small at 0.9 dB. For (V), the overall mean deviation is quite large at 1.7 dB, indicating that a number of other elements should be tested to improve the confidence in the measured mean and variation gain of the sinuous antenna. Encouragingly, the subgroup deviation (e2 and e3) is acceptably small at 1.0 dB.

These results show that the (H) performance between different elements is quite repeatable. Even though that for (V) is not so repeatable, it is sufficiently so for our purpose. We will measure the performance of every element in the final SAMI-2 array and account for the inevitable disparities between them in the image inversion algorithm.

4.6.5 Polarisation separation

In the optimal case, the SAMI-2 antenna will be able to discriminate between orthogonal polarisations by at least 10 dB, as listed in Table 2.1. We measured PS of element 2 by subtracting the cross-polarised gain (XH or XV) from the co-polarised (X-polar) gain (CH or CV), between which the horn polarisation is changed to give cross- or co-measurements. Figure 4.18 shows the PS over

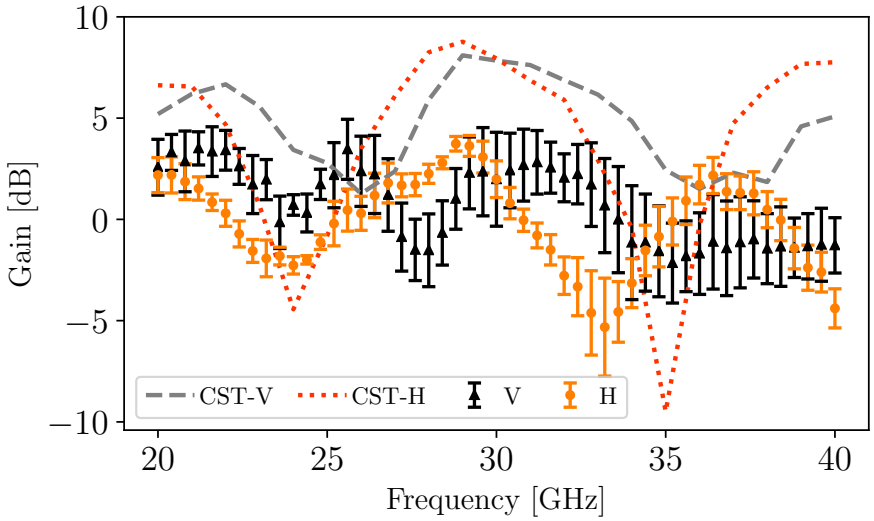

Figure 4.17: Mean boresight gain for the three sinuous elements, both horizontal (H) (orange circles) and vertical (V) (black triangles) polarisations. These are compared with their simulated realised gains over frequency, vertical (gray dashed) and horizontal (red dotted). The measured minimum to maximum variations are 5.7 dB for (V) and 9.1 dB for (H).

frequency, CH − XH for the horizontal (filled stars) and CV − XV for the vertical (filled triangles). The component gains used in this calculation are also plotted: the middle dataset pair is co-polar gain and the lower pair is X-polar gain. Both PS and gain have units of decibels, so their data is plotted on the same vertical axis. The magenta line shows the target PS, which is achieved by both sinuous polarisations over most of the frequency range. More precisely, the mean PSs are 12.3 dB for (V) and 14.3 dB for (H), which are comfortably above the specified optimal value. Only a small range of frequencies are below the target level. The minimum PS for (V) is 7.6 dB and for (H) is 8.5 dB, which we are more than happy with over a frequency octave.

The X-polar data is not adjusted for the inherent polarisation wobble (discussed in section 4.6.3) as it is simply measured only at 0° rotation. Consequently, the actual PSs will be greater than, or equal to what we have calculated here, shown by the filled markers in figure 4.18. In future experiments the X-polar wobble can be measured and these results adjusted to give the full PS.

4.6.6 Co-polar emission pattern measurements

The SAMI-2 array needs a broad field-of-view (FOV) to image a large portion of the the Mega-Ampere Spherical Tokamak Upgrade (MAST-U) edge plasma. The desired FOV is ±40° over two-dimensions, the azimuth and altitude axes. Therefore, the response of the sinuous antenna must be measured over this 2D range of angles.

We set up the rotating mount to enable rotation in the azimuthal and altitude axes. The DUT is positioned so as to minimise linear offsets introduced by rotation in both axes. The antenna separation is fixed at 100 cm. Sinuous antenna gain, over ±60° about the azimuthal and altitude axes, is shown in figure 4.19, horizontal polarisation, and figure 4.20, vertical polarisation. Both figures have values below −10 dB shaded out in magenta to give a greater proportion of the colour

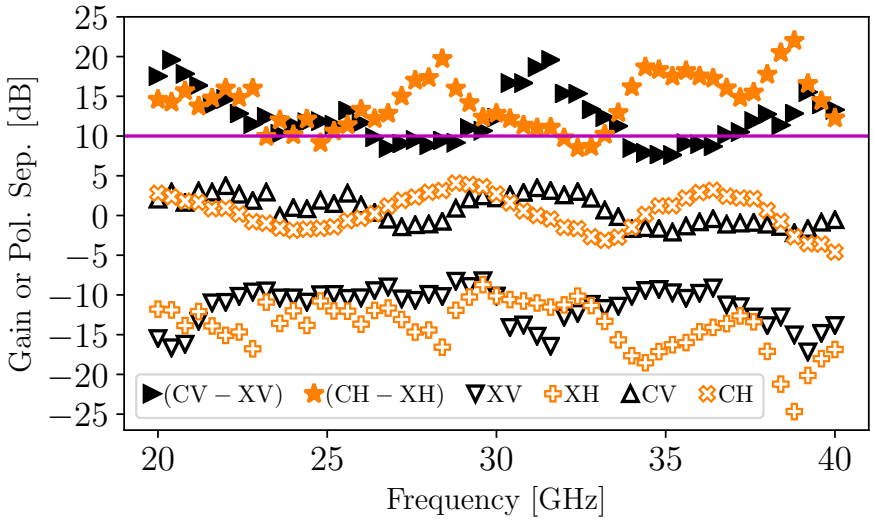

Figure 4.18: Polarisation separation (PS) for both polarisations of element 2, horizontal (CH − XH, filled stars) and vertical (CV − XV, filled triangles). The mean and minimum PS values are 12.3 dB and 7.6 dB for (V) and 14.3 dB and 8.5 dB for (H), respectively. These mean PSs are well above the optimum specified value of 10 dB.

axis to the ares of interest (±40° in both axes).

These gain calculations assume the antenna is rotated about two axes which pass directly through its centre. This is not possible with the present experimental set up. The resulting unavoidable linear offsets introduced in the rotations means the DUT is not always receiving precisely the same power from the horn. By keeping the linear offsets as small as possible, we minimise these power differences. The largest angular displacement of 4.8° occurs at the minimum altitude angle (−60°). The gain difference of the horn at this far-field displacement angle is shown in figure 4.13 by the orange circles. The maximum and minimum differences have the same absolute value of 1.5 dB. When the sinuous antennas are at this smallest altitude angle, some low frequencies will see a slightly higher gain from the horn than the calculation assumes, but the majority will see a slightly lower gain. If this were corrected for, most frequency points would have a somewhat broadened emission pattern. The gain difference values are calculated from the horn emission pattern, measured in the same way as the sinuous antenna's. There will also be a small counteracting error introduced, as the horn is not rotated perfectly about its axes either. (This will be negligible at the small angles focused on here, however.)

As with the polarisation wobble measurements, we remove the frequency dependence in these data by plotting the gain at each angle relative to the gain at 0°. Figures 4.21 and 4.22 show the resulting sinuous antenna gain relative to its gain at $(\theta, \phi) = (0, 0)$, over ±60° about the azimuthal and altitude axes (*not* adjusted for polarisation wobble about the antenna's boresight axis). Over the desired FOV of ±40°, most of the antenna's frequency range has a relative gain of ≥ -10 dB relative to boresight. This performance is sufficient to fulfill the FOV specification in Table 2.1.

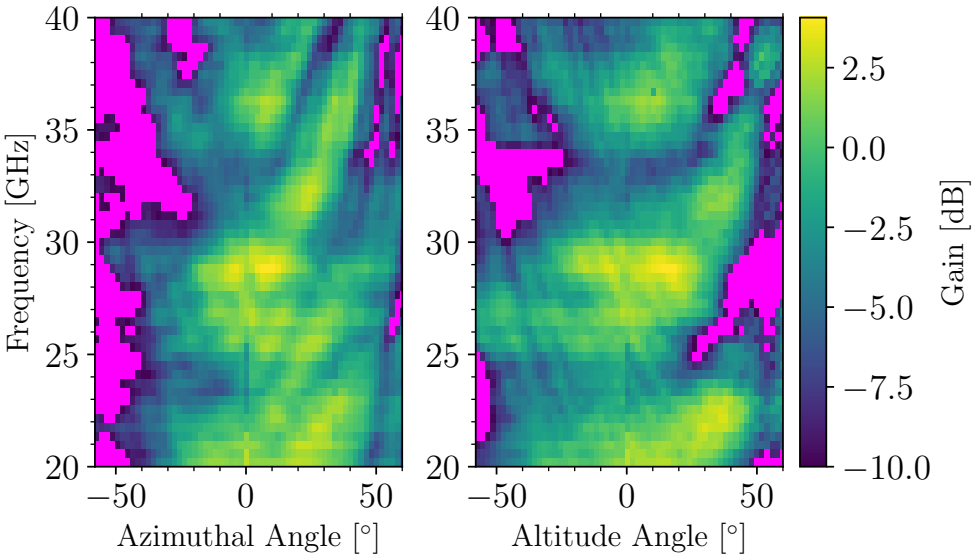

Figure 4.19: Sinuous element 3, horizontal (H) polarisation azimuthal (left) and altitude (right) rotation co-polar measurement over frequency between 20-40 GHz. The colour axis shows the gain at each angle. Magenta is used for points with a gain below −10 dB. Horn-DUT separation is 100 cm and a 2° angular step was used, out to ±60° in both axes.

4.7 Conclusions

In this chapter we have described the design and testing of Vivaldi and dual-polarisation sinuous antennas, with continual focus on the fulfillment of the optimal antenna specifications described in chapter 2, Table 2.1. The modified Vivaldi design meets the baseline antenna criteria, as well as sporting performance extended up to 40 GHz. The sinuous antenna achieves almost all of the optimal specifications: it is dual-polarisation, planar, operates up to 40 GHz, has a small cross-section, has a 40° FOV and ≥10 dB polarisation separation at most frequencies. It may operate acceptably down to 15 GHz, but this has not been tested. This is not necessary, because the radio frequency (RF) mixers chosen in Chapter 5 are only listed as working down to 24 GHz. While they still operate reasonably well at 20 GHz, their performance is likely to drop off substantially at lower frequencies. In any case, operating below 20 GHz only affords view of a small fraction of the H-mode pedestal on MAST-U (see figure 2.4).

We won't know if the sinuous antenna's performance is completely sufficient for SAMI-2 until we calculate an image reconstruction with the whole phased array. Before manufacturing the full 30 element array it is difficult to measure the true reproducibility and inherent variations in the performance of the antenna. This requires a larger sample size than the three elements tested here. Greater inter-antenna and inter-balun effects will also be present in the full array, which will certainly have an impact on the array performance. Construction and measurements of the full array are beyond the scope of this thesis and are left for further work.

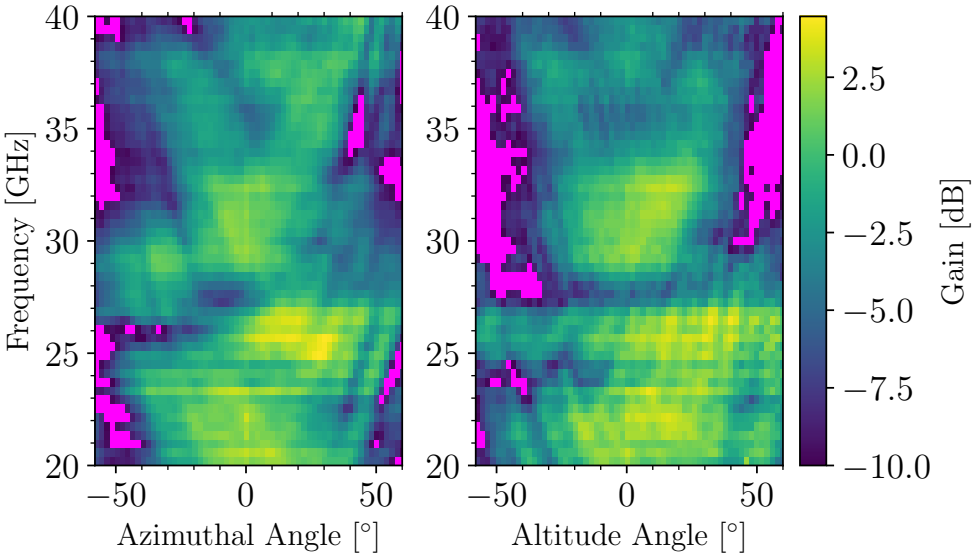

Figure 4.20: Azimuthal (left) and altitude (right) rotation co-polar measurement of element 3 vertical (V) polarisation, over frequency between 20-40 GHz. The colour axis shows the gain at each angle. Magenta is used for points with a gain below −10 dB. Horn-DUT separation is 100 cm and a 2° angular step was used, out to ±60° in both axes.

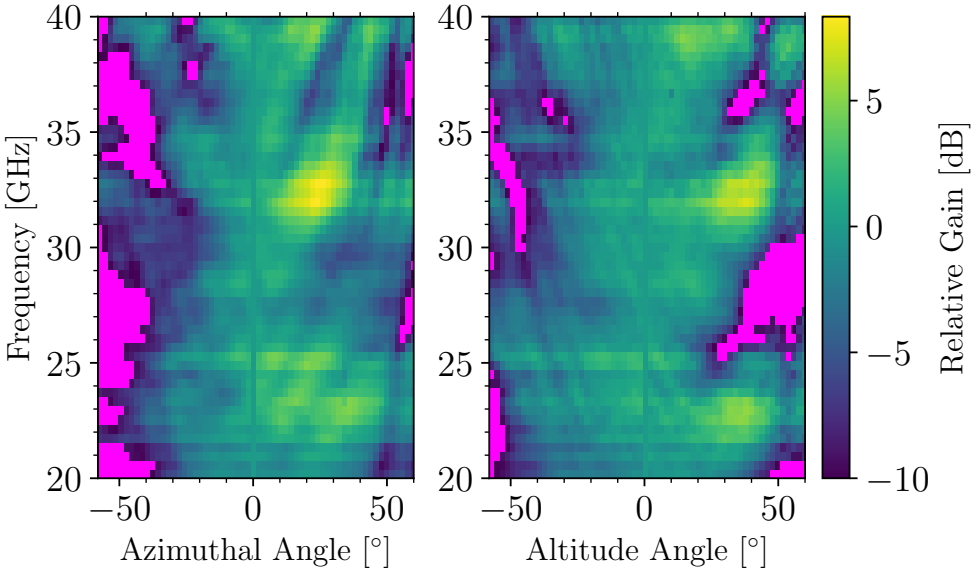

Figure 4.21: Azimuthal (left) and altitude (right) rotation co-polar measurement over frequency between 20-40 GHz. The colour axis shows the gain at each angle relative to the gain at 0°. Magenta is used for points with a relative gain below −10 dB. The DUT is sinuous antenna array element 3, horizontal polarisation. Horn-DUT separation is 100 cm and a 2° angular step was used.

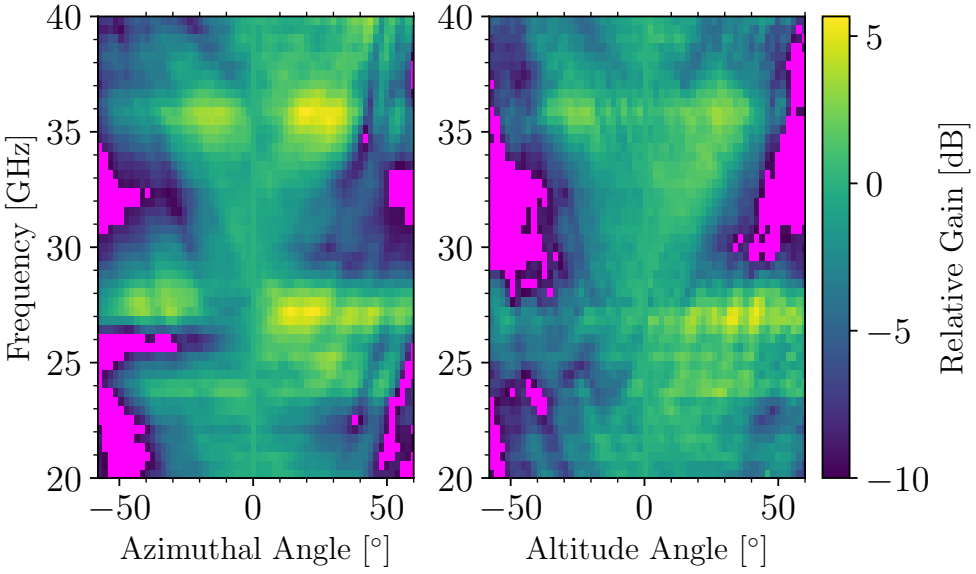

Figure 4.22: Azimuthal (left) and altitude (right) rotation co-polar measurement over frequency between 20-40 GHz. The colour axis shows the gain at each angle relative to the gain at 0°. Magenta is used for points with a relative gain below −10 dB. The DUT is sinuous antenna array element 3, vertical polarisation. Horn-DUT separation is 100 cm and a 2° angular step was used.

Chapter 5

Design of RF electronics

High frequency electromagnetic (EM) waves in transmission lines are more lossy than low frequency waves. To retain information contained in high frequency waves, while transporting them over longer distances, they can be mixed down to a lower frequency. Incoming high frequency signals received by the Synthetic Aperture Microwave Imager-2 (SAMI-2) antennas are mixed with a known, similarly high frequency signal, the local oscillator (LO). The mixed outputs are filtered to remove unwanted products of the mixing. The only product retained is the difference between the unknown input and the LO over a small frequency band either side of the LO frequency. This preserves information about the unknown input signal, but at lower frequencies which can be transmitted over longer distances. Block (2) in figure 5.1 is the mixer subsystem, fed by the antennas (1) and LO (3).

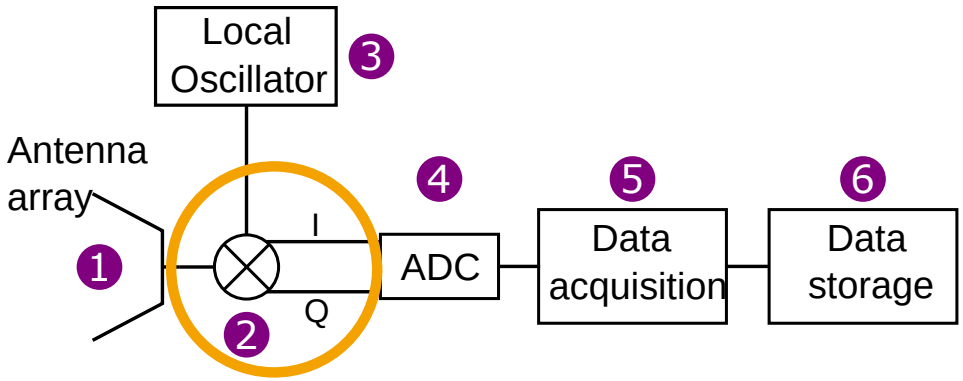

Figure 5.1: (Reprint from chapter 2) High-level block diagram showing the main SAMI-2 subsystems. Only one antenna polarisation and frequency signal path is included for brevity: each antenna is dual-polarisation and both polarisations are mixed with two LO frequencies. Here we focus on block (2): the in-phase and quadrature (IQ) mixer module, encircled in orange. Between the mixer and the analogue to digital converter (ADC) blocks, the IQ signals are amplified and filtered by separate modules. We will not discuss these modules directly in this thesis.

5.1 Down-converter design specification

Gigahertz signals suffer strong attenuation in transmission lines and consequently require some manipulation for practical use. Those received by the SAMI-2 antenna array are down-converted:

mixed with a known LO signal and filtered to leave only the differences between the radio frequency (RF) input and the LO over a bandwidth of several tens of megahertz in frequency, the intermediate frequency (IF). Lower frequency signals such as these experience far less attenuation and can easily be passed on through the system without significant losses.

As discussed in section 2.3.2 the down-converter mixer subsystem is under some constraints which impact its design. Most significant is the downward pressure on its cross-sectional area in the antenna boresight direction. Since the downconverter printed circuit boards (PCBs) are each located behind their antenna, these width and height dimensions (in the horizontal and vertical directions, respectively) may directly impact the antenna array placement, and consequently the array response and sidelobes, if they become larger than the antenna radius. In conjunction with the following design specifications, these constraints, especially to limit the width, are difficult to fulfil.

For the signals from each dual-polarisation antenna in the array, mixed at two simultaneous LO frequencies, we require four mixer channels per downconverter PCB, operating from at least 40 GHz down to ideally below 20 GHz. IQ mixers must be used as they provide phase information in the IF without which the image reconstruction of the phased array would be unattainable. Two RF power dividers operating up to 40 GHz are needed to split the incoming antenna signals and a further two for both LO frequencies. The mixer IF bandwidth should be around 50 MHz and the overall conversion gain of the downconverter should be high given the low received signal expected in passive acquisition mode. Remote control of the mixers may be required, depending on the final choice.

5.2 Down-converter design process

Mixer choice is the pivotal decision to be made early on in the downconverter design process, as most facets of the design depend on this choice. The first branch of this choice is between designing custom RF PCBs or building one from off-the-shelf connectorised components, similar to the choice between Lego and Playmobil. Due to the fact that the spatial volume associated with a connectorised solution would likely be difficult to fit adjacent to the the Mega-Ampere Spherical Tokamak Upgrade (MAST-U) vessel and that the cost would outstrip the entire SAMI-2 budget, detailed in section 2.3.2 and Table 2.2, we sought a custom solution (the length of this chapter may have indicated this choice). To the author's knowledge there are two options for an integrated circuit IQ mixer operational up to 40 GHz, the HMC8192 and the ADMV1014, both manufactured by Analog Devices. The ADMV1014 is an active mixer and consequently needs a number of decoupling capacitors positioned in its immediate vicinity, whereas the HMC8192 is a passive device requiring little in the way of surrounding components. For this reason the total PCB footprint for the passive option is much reduced, which reduces the downconverter's width and accordingly the impact on the antenna array performance, also discussed in section 2.3.2. The ADMV1014 has an in-built LO frequency quadrupler, which drastically reduces the overhead for the LO supply. This is because 10 GHz signals experience far less transmission-line attenuation than 40 GHz signals, made more significant considering the division stages required (up to 64-way) and distance to travel. The choice between passive and active mixer was made for us externally, by continual delays to the HMC8192 release until after the completion of the design of a four channel

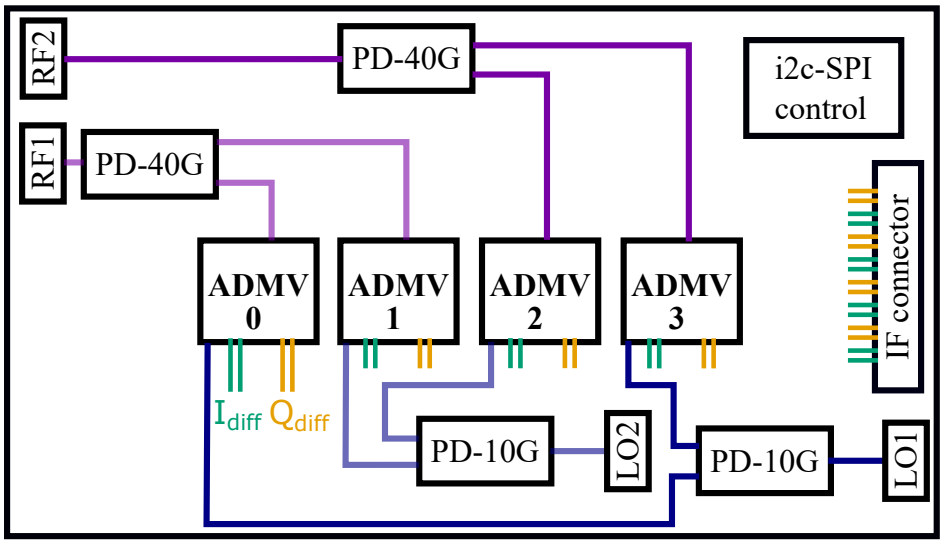

Figure 5.2: Block diagram of the key components on the down-conversion module, block (2) in figure 5.1. The RF and LO signal paths through their respective connectors and power dividers are shown in blue and purple, respectively. *PD-40G* is a power divider up to 40 GHz and *PD-10G* is a power divider up to 10 GHz. IQ differential output locations are also shown, along with the approximate IF connector location, these signal paths are not included as they will use copper layers other than on this top surface. Figure 5.11 elaborates on the i2c-SPI control block.

downconversion PCB using the ADMV1014.

A brief outline of the downconverter PCB design process is described here, following which the key steps are further elaborated. We positioned twenty seven decoupling capacitors surrounding the $5 \times 5\,\mathrm{mm}^2$ ADMV1014 package to make the footprint of one mixer. Then, we arranged four mixers and their satellite components, to begin to ascertain the approximate PCB dimensions. Space for two RF and two LO power dividers was included and rough track routing laid for these signals and the IF, leading to the block diagram in figure 5.2. We added an RF amplifier (the HMC1040LP3) between the RF connectors and power dividers, to boost boost the antenna signal into the mixers. We chose Mini-circuits' EP2KA+ and EP2C+ two-way power dividers for the RF and LO signal paths, respectively. The topology of the high frequency routing means one LO connector must be placed in the middle of the board to avoid sending any microwave tracks through vias. A further effect of the topology is that it necessitates four copper layers as the minimum. Due to this constraint on the LO input, we decided to use vertical connectors. Eight differential IF outputs, in addition to power and control I/O, immediately ruled out low frequency individual connectors, such as MMCX or SMP, as well as large multi-pin options like RJ-45 Ethernet connectors, due to the board width constraint. Instead, we chose the Samtec LSHM connector. These offer dense, low-profile I/O and right-angle configurations are available, which is ideal for the confined space behind the 32 element antenna array.

The mixers use a four line SPI interface and their start up sequence requires toggling of individual reset pins. In total, this gives 11 SPI and low voltage control lines for the control of the four-channel downconverter. To reduce this I/O overhead, we selected the i2c (or iic) 2-line protocol, which is converted through an on-board i2c-SPI bridge, circuitry shown in figure 5.11. Three voltages are

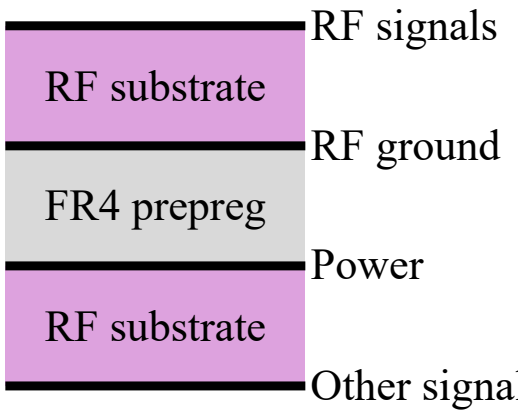

Figure 5.3: Substrate layer build up for the downconversion PCB. The black lines denote copper layers, arbitrarily starting at the top, carrying the RF signals, RF ground plane, power plane and the bottom layer for other signals. The pink substrate is a low loss-tangent substrate, suitable for carrying RF signals, and the two here are bonded with an FR4 prepreg layer.

supplied to the ADMV1014s, 1.5 V, 1.8 V and 3.3 V. Individual mixer voltage regulators were connected to a 4 V power rail, along with a 1.8 V and 3.3 V regulator for powering the control circuitry and a 2.5 V regulator to feed the RF amplifiers.

5.3 Board topology

With dual polarisation and two simultaneous frequencies a topological issue arises for the RF-module. The two RF signals from different polarisations, RF1 and RF2, must be split in two and delivered to each mixer. For the capability to operate at two frequencies simultaneously, we must provide two LO signals to the board, which are divided in two and sent to each mixer. Each LO signal is sent to one mixer receiving RF1 and one receiving RF2. To fulfil these requirements on a single copper layer necessitates one RF or LO connector being placed in the middle of the board, whereas the other connectors will be close to or on the edge. As the RF signals come from the antennas and are fourfold higher in frequency, we gave them priority. Accordingly, the LO2 connector is placed in the middle of the board. It is possible to send signals of several GHz through vias to other copper layers, but this would require simulation work to minimise the resulting impedance discontinuity. Furthermore, as discussed in more detail below, this would more strictly limit the choice of substrates and prepregs, as the signal would pass through the board rather than only on the top surface.

Given the track topology in figure 5.2 at least four copper layers are required for the RF module, as the entire first inner layer below the RF signal layer must be ring-fenced for RF ground. We designated the remaining two copper layers as a power plane and a miscellaneous signal layer, which are all displayed in figure 5.3.

5.4 40 GHz connector launch

Two types of gigahertz capable connector are required by SAMI-2, for the RF and the LO signals coming on and off the downconverter module. A high frequency PCB connector is needed to transfer

both RF signals, up to 40 GHz, between the antennas and mixers. Here we first discuss testing of candidate RF connectors, the final choice being With-wave narrow body 2.92 mm connectors. Secondly, we explain our choice of vertical SMP connectors for the two LO signals, operable up to 10 GHz, see section 5.5.

5.4.1 Amphenol RF SMPM connectors

SAMI-2 requires a high frequency PCB connector, operational up to 40 GHz, to enable the system to be modularised and allow the balun and the down-converter to be manufactured on separate PCBs. Initially, we chose the Amphenol SMPM right-angle 925-140J-51P connector for its small size and low cost for its top frequency of 40 GHz. Naïvely we assumed these would work out of the box, with the manufacturer's recommended copper land pattern. This beleaguered many subsequent tests of test PCBs, such as the first dual-polarisation baluns. After our discussions with the manufacturer, an alternative end-launch version, the 925-169J-51P, was suggested by Amphenol RF to be more likely to work for our application.

5.4.1.1 End-launch

Again, naïvely we repeatedly tested this connector on basic pass-through boards which we designed with little thought, relative to later iterations, and unsurprisingly performed poorly (with low transmissions (S21), especially at higher frequencies). Potential causes for this poor performance were struck down one by on. Substrate loss, resonant reflections, PCB manufacturer error and soldering of the connectors were not found to be significant contributors to the low transmission. We realised that a stronger simulation effort was required, in order to reach a design for the connector launch that would perform satisfactorily (prior to this the simulation efforts had only followed, not led, the experimental measurements and failed to match well). We created an more accurate model of the 925-169J-51P in CST (previously a cylindrical approximation was used) and an attempt was made to replicate Amphenol RF's own simulation results, on 0.305 mm Rogers 4003C using their supplied launch geometry.

5.4.1.2 Replicating Amphenol's data

Simulation data for the connector was provided by Amphenol RF, which gave the minimum return loss for the 925-169J-51P as −17 dB, between 26.5-40 GHz, and better at lower frequency. A more intricate recommended launch layout (than that in the datasheet) was also provided, shown 2D in figure 5.4a. It includes a tapered signal track and a cutout slot on the RF ground layer beneath the connector signal pin. Copper is removed here to lower the capacitance around the signal pin, as the connector's ground legs sit close to the signal launch on either side. We replicated this launch on 0.305 mm Rogers 4003C with FR4 backing (no prepreg and no copper on layer 3) in CST, making a pass-through with a 39.8 mm long grounded co-planar waveguide (GCPW) transmission line. The signal copper in a GCPW line is flanked by co-planar ground sections on either side and has a ground plane on the other side of the substrate. Our simulations produced S21 shown by the magenta line (a) in figure 5.5, exhibiting good transmission, above −1 dB, up to 35 GHz before oscillations caused by an impedance mismatch become significant.

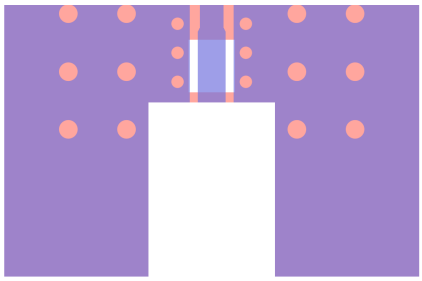

(a) SMPM launch layout recommended by Amphenol, on Rogers 4003 0.305 mm backed with FR4. Purple denotes top layer copper, and orange denotes RF ground layer copper which extends to the same outer perimeter as the top layer and contains a rectangular cutout beneath the wider signal track holding the connector's signal pin. The circular gaps in the top layer indicate positions of vias.

(b) Our optimised geometry for the 925-169J-51P connector launch geometry on Rogers 4003 0.203 mm backed with FR4. Signal copper is in purple and RF ground layer in orange, which covers the same extent as the top copper. Triangular slot can be see underneath the wider signal-pin copper. Vias are not shown here, however they are located in identical positions as the vias shown in the original launch in figure 5.4a.

Figure 5.4: Initial (a) and final (b) SMPM launch copper layouts.

Baluns for the sinuous antennas use 0.203 mm substrate, so we tweaked the track impedance of the original launch to reflect this change, then simulated the new model. As this geometry was untailored for the new substrate thickness the transmission in figure 5.5 (b) is slightly worse overall than (a). To smooth out the impedance transition from the signal pin to the main GCPW transmission line, we tapered the slot down to a width slightly below the main trace width.

We parametrically scanned the slot dimensions, including the beginning and end widths, taper length and total length, to optimise the launch. Our best simulated transmission was observed with the layout shown in figure 5.4a, the end taper width being 0.3 mm. This peak performance is given by line (c) in figure 5.5. Although the data exhibits small oscillations at lower frequencies they are largely eliminated above 30 GHz, showing the effect of the smoother impedance gradient from connector to GCPW, caused by the tapered cutout slot.

5.4.1.3 Experimental verification

To corroborate the simulation results experimentally, the pass-through simulation model using the launch geometry in figure 5.4b was manufactured. We measured scattering parameters of these boards on a Vector Network analyser (VNA) up to 40 GHz. The measured transmission can be seen in figure 5.6 (black dots), compared to the ideal CST simulation [pink, (c)]. A large resonance is observed at 26 GHz, rendering the connector unusable for broadband applications. Were it not for this resonance, transmission over this frequency range is acceptable, despite the approximately 1 dB peak-to-peak maximum wobble measured. Discussions on reasons for this resonance follow, in 5.4.1.4. Firstly, an issue with the experiment is described.

Even with our painstaking preparatory filing, it was difficult to snugly fit the connectors into the edge slots, such that the front face was in contact with the ground copper on layers 1 and 2 (along the short side of the edge slot). Nevertheless, this process was repeated multiple times by both the author and technicians from the Electronic Engineering department of the University of York. The best results obtained are those displayed in figure 5.6. Some discrepancy between the

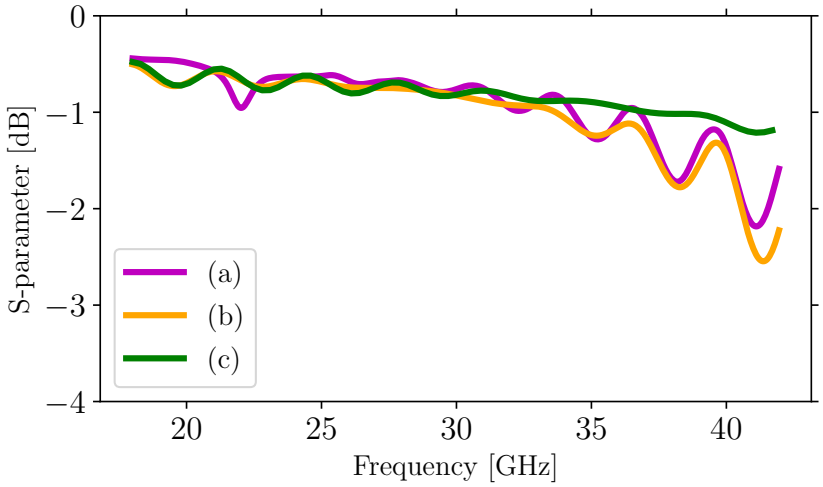

Figure 5.5: Comparison of simulated transmissions (S21) of three SMPM pass through versions with 4-layer board build ups comprised of different thicknesses of Rogers 4003C (L1 & L2) on top of FR4 (L3 & L4). Replication of Amphenol RF launch model on 0.305 mm R4003 (a), first stage 0.203 R4003 (b) and final optimised 0.203 R4003 launch (c).

simulated model and the PCB must therefore exist.

5.4.1.4 Adjusting simulation to show parasitic mode

We applied various changes to the simulation model in an attempt to replicate the resonance in the experimental data in figure 5.6. These included adding an air gap between the connector front and the PCB, adjusting the track taper and track width under the connector pin, removing the FR4 layer and filling in the copper cutout slot. However, none of these changes to the launch geometry brought the transmission anywhere close to the measured data. Finally, we removed a small strip of copper around the three edges of the edge connector slot on the signal and RF ground layers, resulting in a similarly catastrophic fall in simulated transmission as in the experiment. In figure 5.6, simulated S21s, after the copper strip removal, are plotted for two different thicknesses of FR4 backing (blue and orange). When the grounding of the connector body is weakened, by removal of the narrow copper strip along the lip of the edge slot, we see large losses in transmission around certain frequencies, much like in the experimental data (black dots). FR4 thickness (t_{FR4}) in the manufactured PCBs is 1.2 mm, for which we see a drop in simulated transmission at around 35 GHz. Although this does not coincide with the fall at 26 GHz in the experimental data, pointing to a further disparity between the computational model and reality, this result effectively confirms connector grounding to be the issue. Varying the FR4 thickness changes the frequency of the resonance, the orange line in figure 5.6 denotes transmission for $t_{\mathrm{FR4}} = 1.4\,\mathrm{mm}$. This indicates that a parasitic mode is able to propagate in the FR4 layer when the SMPM connector is not perfectly connected to the R4003C ground. PCB substrate models in CST are often based on one data point at 10 GHz and consequently cannot always accurately model the behaviour of dielectric constant and the loss tangent at higher frequencies. A material like FR4 is not designed to work well at frequencies of tens of gigahertz. As such its dielectric constant and loss tangent are likely to

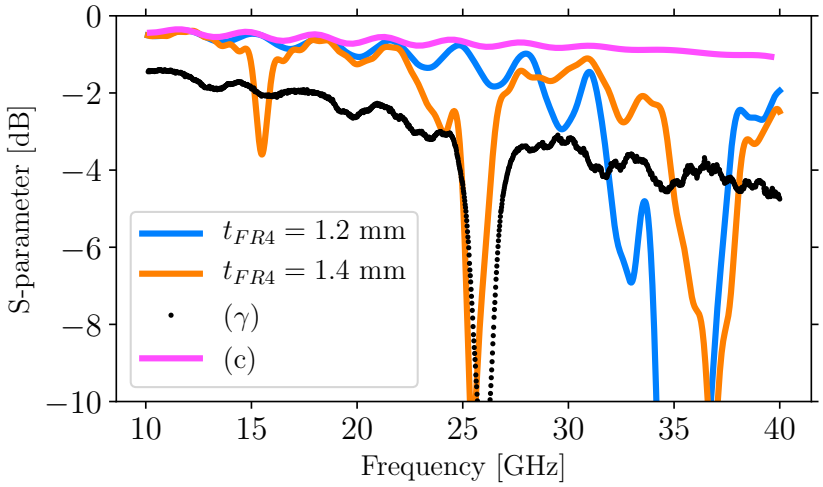

Figure 5.6: Comparison of simulated transmission (S21) from final optimised 0.203 mm R4003 launch (c) and experimentally measured transmission of identical design (γ). We see a large resonant fall in measured transmission at about 26 GHz. Blue and orange lines show more realistic simulated S21 with varied FR4 thickness (t_{FR4}) (after ground was cut away adjacent to SMPM connector on top copper). Manufactured PCB used 1.2 mm FR4 thickness. We see the parasitic mode change frequency with 1.4 mm FR4 thickness (orange).

change significantly above 10 GHz. As we mentioned in section 4.6.4, accurately modelling resonant behaviour requires the full wave propagation to be correct. This in turn requires the material model to be very accurate. For the purposes of this research we are not seeking to accurately model resonant modes like these, only to understand their cause and mitigate them.

It is likely that, given more time, we could prepare and solder a PCB using 925-169J-51P connector well enough to prevent this grounding issue. However, we would have to reliably repeat this four times per antenna in the SAMI-2 array. This is not worth the associated cost saving relative to other connectors.

5.4.2 Other candidate connectors

Two other connectors were investigated for suitability, the Hirose HK-LR-SR2 and the Amphenol SVK 1521-60051, both 2.92 mm end-launch connectors with a maximum frequency rating of 40 GHz. The HK-LR-SR2 connector can be used without soldering as it can be fixed to a PCB with two small screws, the SVK connector must be soldered. Two pass-through PCBs of our design were manufactured to test each of these connectors, both 41.5 mm long on Rogers 4003C substrate with 0.508 mm thickness. We used copper artwork for both connector launches from the recommended launch pattern given in their datasheets. Figure 5.7 shows the transmission (S21) measured for both types of connector, Hirose HK-LR-SR2 in black and Amphenol SVK 1521-60051 in orange. Each connector transmission exhibits significant oscillations and resonances throughout the frequency range, rendering it unsuitable for the broadband needs of SAMI-2.

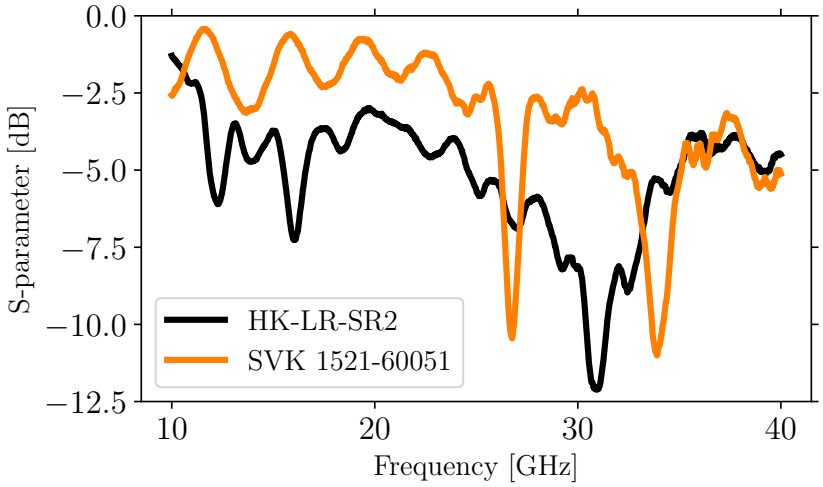

Figure 5.7: Experimentally measured transmission (S21) from two pass-through PCBs over 10-40 GHz: (black) Hirose HK-LR-SR2 solderless screw-down end-launch connector, 41.5 mm long and (orange) Amphenol SVK 1521-60051 soldered end-launch connector, also 41.5 mm long.

5.4.3 With-Wave

Released in September 2019, With Wave's narrow-body NE03FS001 2.92 mm connector was the fourth candidate tested. Experimental data was provided upon release for GCPW launch on 2-layer Rogers 4003C (0.203 mm) and 4350B (0.254 mm) substrates, along with pass-through PCBs for purchase with which to verify the data. SAMI-2's microwave up- and downconverters are 4-layer boards, so we performed simulations of these connectors from With-wave on 4-layer Rogers 4350B boards in CST, to ascertain whether changes to the launch pattern were required. A model of the male connector (NE03MS001) can be seen on the left hand side of figure 5.19, which screws onto the board by sandwiching the substrate with a backing mount plate.

We designed and simulated a pass-through model using 4-layer Rogers 4350B and the 3D models of the NE03FS001 connectors in CST. The resulting transmission is the pink line (w) in figure 5.8 over 10-40 GHz. Several units of this board were manufactured and we measured their S-parameters experimentally using a VNA. The blue ($\omega 1$) and orange ($\omega 2$) lines in figure 5.8 show the measured transmission through two identical custom pass-throughs. For comparison, we also tested the GCPW pass-through provided by With Wave. Its performance is given by the black line (Ω) and it has reasonably similar transmission to our pass-through PCBs. Our PCBs have a minimum S21 of −3.8 dB, compared to −3.4 dB for With-wave's board. Their mean S21's within 0.1 dB, at −3.0 dB and −2.9 dB, respectively. Minimum return losses (S11 and S22) for our custom boards are all below −15.6 dB and for With-wave's board are all below −16.2 dB. The custom PCBs are 30.81 mm long, whereas the test board sold by With Wave is 25.45 mm long, so the results are not precisely comparable. Our PCB performances are acceptable and they would fair slightly better if the transmission line lengths were the same, relative to With-wave's board. None of the connector signal pins were soldered to the PCB tracks in these experiments. Following these results, these connectors were selected for all RF PCB interconnections in SAMI-2: the Vivaldi and sinuous antenna launches, the down-converter inputs and the up-converter output.

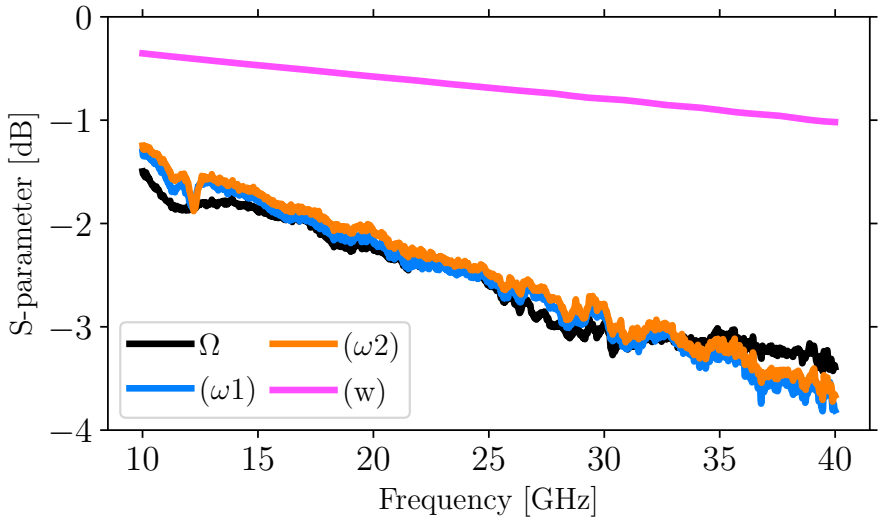

Figure 5.8: Experimental transmission (S21) measurements using With-wave NE03FS001 connectors, unsoldered, on GCPW transmission lines. Data ($\omega 1$ and $\omega 2$) from two custom 30.81 mm long pass-through 4-layer PCBs of Rogers 4350B, each core being 0.254 mm thick. Simulated transmission (w) in CST for the identical board, including connectors. Pass-through PCB provided by With-wave (Ω), 25.45 mm long, on 2-layer Rogers 4003C 0.203 mm thick, all over 10-40 GHz. Our PCBs perform well enough compared to With-wave's.

5.5 Local Oscillator connector

To provide the LO signal to the up- and downconversion PCBs a lower frequency connector is required for the 5-10.25 GHz LO range of the ADMV1013 and ADMV1014. Due to the topology issue with the downconversion board, outlined in section 5.3 and figure 5.2, this should be a vertical launch connector. We identified Molex's SMP 85305-0232 and experimentally tested its performance, by way of a straight GCPW pass-through of 30 mm length, using the manufacturer's recommended footprint; the transmission of which is given in figure 5.9. Minimum transmission is −2.43 dB at 10.12 GHz and the maximum ripple amplitude is 0.43 dB at 9.9 GHz.

5.5.1 Local oscillator supply

Due to the internal quadruplers in the ADMV1013 and ADMV1014 the local oscillator subsystem need only supply a signal between 5-10 GHz. We require two independent LO sources for dual-frequency imaging. These signals must each be sent to all the down-converter and up-converter boards, requiring 32-way division, which itself likely necessitates an amplification stage. This is because the recommended LO input power for both mixers is −6-+6 dBm, in which we will target a power in top half. The LMX2594 is a wideband frequency synthesizer produced by Texas Instruments, with widely variable output power, up to 7 dBm, over its 0.01-15 GHz frequency range. Its availability as an evaluation module greatly reduces the overhead for us to use it in the SAMI-2 system, given that only two are required.

The LMX2594 output is fed into a ZVA-183-S+ connectorised amplifier from Mini Circuits and

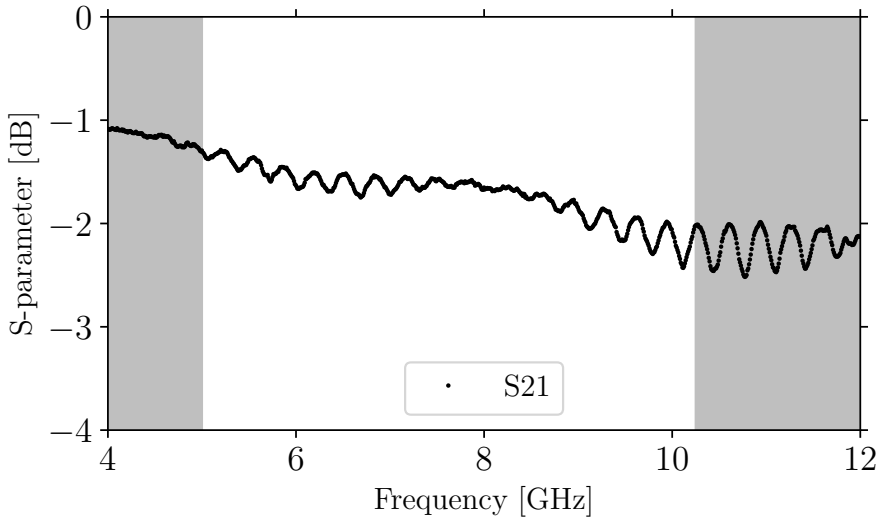

Figure 5.9: S-parameters from a pass-through PCB with a Molex SMP 85305-0232 connector on either end. The substrate is Rogers 4003C of thickness 0.508 mm and the track is 30 mm long. Two SMA-SMP cables were used to connect this board to the VNA so their effects on signal transmission are included in these data. Return losses (S11 and S22) are below −10 dB over the whole frequency range. The shaded regions indicate frequencies outside of the required range: 5-10.25 GHz.

then directly into a custom 32-way power divider from Atlantic Microwave, before transmission over SMA-SMP cables onto the up- and down-conversion PCBs. Output power from the synthesizer was flattened across the relevant band relative to the maximum output power at 10 GHz, with a span of 3.2 dBm between the maximum and minimum power. It was also systematically reduced to remain comfortably below the amplifier's maximum input of +4 dBm, the maximum output power from the LMX2594 used in this set up is +1 dBm. Using a spectrum analyser, the final power of this set up was measured over 5-10 GHz and is shown in figure 5.10. With a peak-to-peak span of 2.5 dB, the output is acceptably flat to remain within the recommended mixer input ranges, thus not being a detriment to their performance.

5.6 Components and other connectors

Three tiers of decoupling capacitors are required on the DC voltage inputs to the ADMV1014, to smooth out any fluctuations in the supply voltage. This is necessary to retain the integrity of the high frequency signal processing inside the IC. A digital-to-analogue converter is required to vary the RF gain voltage; we selected the AD5696R/AD5694R for this purpose. To measure the RF input voltage detector signal, sent out of the ADMV1014, an ADC is required, for which we chose the LTC2487.

An IF connector operable up to a few hundred megahertz is needed to transfer the eight differential signals off the board. The space demand of 16 individual connectors is large, so we sought a multi-pin solution. We initially selected RJ-45 Ethernet connectors (8-pin), however this choice would significantly impact the array placement as a shielded RJ-45 is 14 mm high, and 16 mm wide.

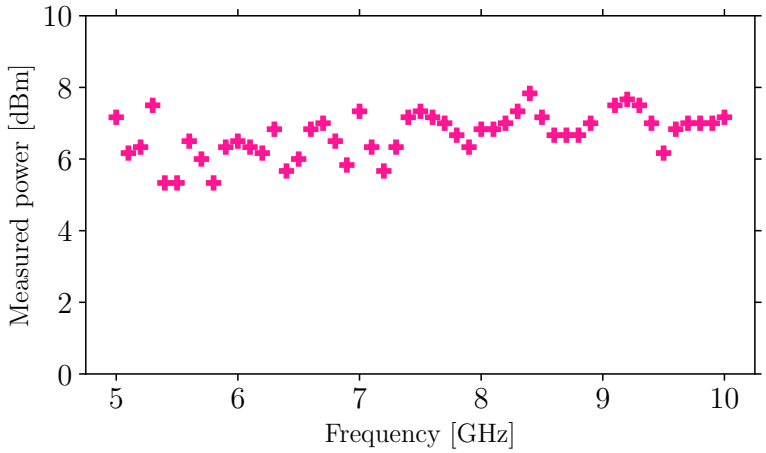

Figure 5.10: LMX output power flattened according to the maximum output at 10 GHz, amplified by the ZVA-183-S+ connectorised amplifier and sent through the 32-way LO power divider. Power output spans 2.5 dB between the maximum and minimum.

In addition two would be required for the eight differential IQ outputs, leaving no pins for power or control, calling for yet another connector. As a result, we chose Samtec's LSHM-120-01-L-DH-A-S-K right-angled 40-pin connector, which has a cross section approximately 4 mm in height and 15 mm in width. They are operable up to 11 GHz which comfortably encompasses the 50 MHz IF bandwidth. Individually shielded flat-tape cables are manufactured by Samtec to link between two LSHM connectors. We use these connectors on the other SAMI-2 PCB modules, which enables simple interlinking, with or without the flat-tape cable.

5.7 Board control

The ADMV1014 has a 4-wire SPI interface which is used to control a range of internal settings. For example, registers set via SPI choose the IF output mode, control the baseband I/Q amplifier, select the LO frequency band, change the RF input voltage detector settings and adjust the LO phase. As the board's width constraint limits the LSHM connector to 40-pins, and given that the eight differential IF outputs take up most of the available pins, the i2c protocol [119] was chosen to control the downconverter. I2C, interchangeably I^2C or IIC, is a 2-wire bus used for inter-IC control with bidirectional transfer speeds of up to 3.4 Mbps. The two lines are the serial data line (SDA) and the serial clock line (SCL).

5.8 Power

The highest voltage required by components on the downconverter is 3.3 V, which is also the voltage at which the lion's share of current is required. The bulk of the ADMV1014 current, 437 mA is supplied at 3.3 V and the I2C bus also operates at this voltage, while the HMC1040LP3 amplifier is driven at 2.5 V. A 1.8 V supply is required for the ADMV1014 gain control and level shifting SPI lines to control the mixers, while the mixers' internal LNAs are powered by 1.5 V supply. We gave

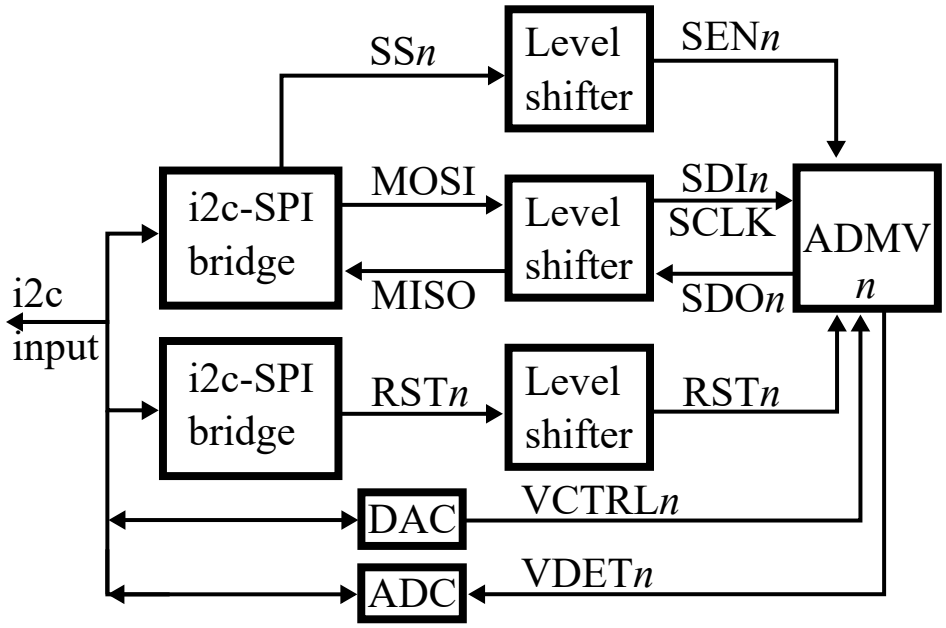

Figure 5.11: Block diagram of the i2c-SPI interface used to control the down-converter, where n ranges from $0-3$ over the four ADMV mixers. Each ADMVn in figure 5.2 receives and outputs the signals shown here. These mixers use 1.8 V for their SPI control, so level shifters are required to translate the outputs from the i2c-SPI bridges, as i2c operates at 3.3 V.

each mixer its own separate 3.3 V, 1.8 V and 1.5 V regulators to keep the mixer layouts modular and keep the voltage regulator power handling requirements, mainly for the 3.3 V regulator, to a reasonable level (below 2 A. We ran a 4 V power rail most of the length of the board, to feed each mixer's modular trio of regulators. Individual 3.3 V power planes are located under each ADMV1014. These provide low impedance feeds to each of the 3.3 V IC pins and disperse residual heat generated by the power supply. At the end of the power rail a 2.5 V regulator supplies the RF amplifiers. Separate 3.3 V and 1.8 V regulators power the control circuitry at the low frequency end of the board.

5.9 IF filtering

IQ output from the ADMV1014 is between 0-6 GHz, so must be low pass filtered to prevent anti-aliasing at the digitisation stage, as the bandwidth of interest is up to 50 MHz. Given the top end IQ output frequency it is advisable to perform this filtering in two stages. We set the first filtering stage directly adjacent to the mixers, using the LFCG-320+ from Mini Circuits, with a passband up to 320 MHz. Ideally a reflectionless filter would be used to prevent any signal returning into the mixer, which may reduce the signal to noise ratio. However, no reflectionless component was identified with a stopband extending up to 6 GHz. Therefore, we selected this reflective option, as preventing transmission of the IQ output above 50 MHz is most important.

5.10 Transmission line simulations

Due to the limited dimensions, topology and frequency of operation of the down-conversion PCB, careful routing and consideration of the transmission line losses was required In order to do this, we designed and simulated six different GCPW track geometries in CST; their copper layouts are shown in figure 5.12. These are as follows: a straight track with regular via fence (a) as a control model; two straight tracks with irregular via fences, (b) and (c) replicating those in the ongoing down-converter design; and three curved tracks also replicated from the PCB design, (d), (e) and (f). Vias running close alongside the tracks are duplicated from our preliminary down-converter design, while grids of vias covering the surrounding board areas are to provide good grounding and do not mirror the PCB design. All vias are modelled as solid conducting cylinders, as this produced results which were negligibly different to using cylindrical shells to model their plating. We simulated these models to ascertain if any part of their inherent impedance irregularities affected the transmission, not to measure their absolute transmission. Due to the lack of material model data above 10 GHz (aside from estimations), it is unrealistic to seek absolute performance values at higher frequencies. Simulated transmissions (S21) through all six tracks are displayed in figure 5.13 and the relevance of each track geometry will now be elaborated.

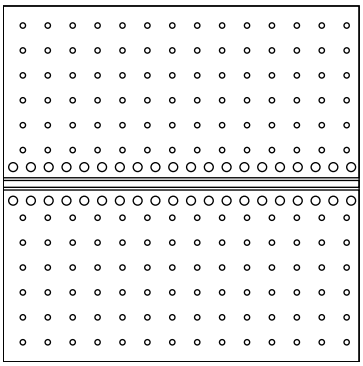

(a) Straight GCPW track (control).

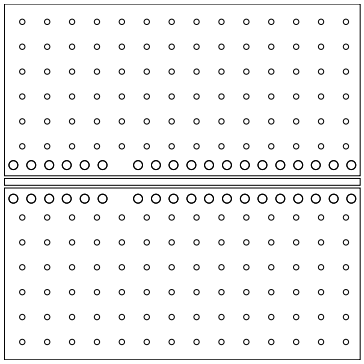

(b) Straight GCPW with irregular via fencing (RF).

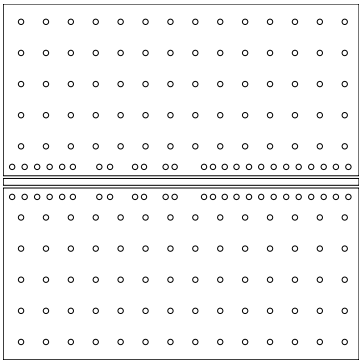

(c) Straight GCPW with irregular via fencing (LO).

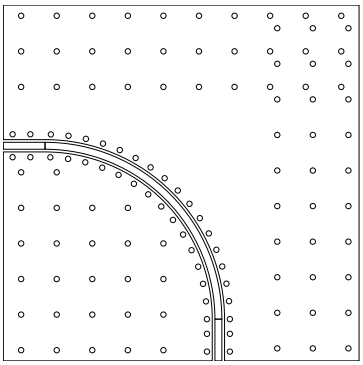

(d) Curved GCPW track with bend radius 9.75 mm.

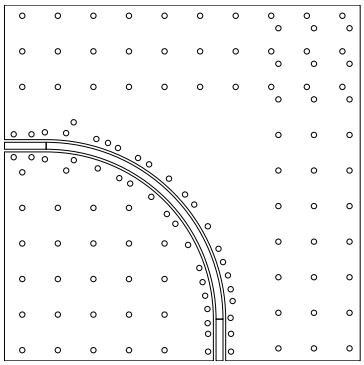

(e) Same as (c) with an irregular via fence.

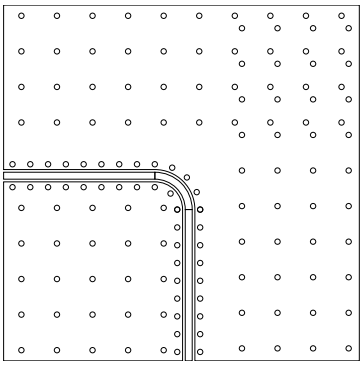

(f) Curved GCPW with bend radius 1.9 mm.

Figure 5.12: Top copper layouts of the six simulated GCPW transmission lines. All simulations used the time domain solver and open boundaries. They were all excited by waveguide ports and mostly used 0.3 mm diameter vias, except for a and b which used 0.5 mm vias in the track fence. All six models used 0.254 mm Rogers 4350B and have unbroken ground planes on the back side.

We had to route many of the differential IQ tracks underneath the high-frequency RF and LO tracks, on the opposite face of the board, to reach the LSHM connector. In addition, most DC or low-frequency control tracks have to cross beneath these high-frequency tracks (on the very back of the board, layer 4) in order to access the various control ICs. Due to the track widths and via fence-spacing, this forces non-uniformities in these fences in certain locations alongside the high-frequency tracks. Figures 5.12b, 5.12c and 5.12e show key examples of these irregular via fences for straight and curved RF tracks, which are exact replicas of via fence placements from our preliminary down-converter PCB design. Case (b) replicates a control line crossing underneath the RF path which, as shown by figure 5.13, has negligible effect on transmission. Geometry (c) mirrors a LO track crossed by multiple SPI lines, which only needs to transmit signals between 5-10 GHz. This exhibits flat transmission (S21) systematically offset from (a) and (b), due to its fence being made of vias with a smaller diameter.

When designing a high frequency signal path it is advisable to match impedance as closely as possible along its length, as discussed in section 3.1.2. The block diagram in figure 5.2 shows the need for several right angle bends in the RF tracks. Larger bend curvature radii allow smoother transition between different directions of propagation of the transmission line mode, so we designed the corners with the largest bend radii that the available space would reasonably contain. Given more time we would have modelled and tested mitred bends as a space saving measure. As the evaluation boards for the ADMV1013 and ADMV1014 both use curved tracks for their analogue signals, we decided to do the same. Figure 5.12d shows the copper layout for a curved bend of radius 9.75 mm, which fitted best into the RF signal component chain initial layout. The simulated transmission through this line is (d), the black line, in figure 5.13.

Geometry (e) models a RF trace with a set of four differential IQ mixer outputs passing beneath. Ripples in S21 above 30 GHz, figure 5.13 (e), are caused by the non-uniformaties in the via fence required to accommodate the transverse IQ traces, but are not significant enough to cause concern.

Due to the orientation of the divided output ports of the RF power divider (EP2KA+), which come out perpendicularly to the input, two RF tracks must go through a total turn of 180° to reach their mixer. The first 90° of this should be made as tightly as acceptably possible, as these turn radii directly impact the down-converter width. A rule of thumb for bend radii suggests the minimum be about five times the track width [120]. We chose a small bend radius of 1.9 mm, almost five times the 0.39 mm track width. This geometry is exhibited in figure 5.12f and the corresponding simulated S21 is shown by the blue dotted line in figure 5.13 (f).

If control signal lines run adjacent to RF and LO signal tracks, the down-converter can be made on a narrower PCB as this limits the extent of the co-planar ground area next to the track. Therefore, we investigated the transmission degradation for different track-track spacings and then chose the acceptable top ground width. Both RF and LO tracks have via fences running alongside them, making the furthest point of the via pads 1 mm from the edge of the co-planar ground adjacent to the track. This distance will be the minimum allowable width of ground area next to the tracks, as the via fence cannot be moved. GCPW tracks were simulated in CST with different widths of ground plane on one side and the transmission over these tracks; with finite ground planes of width 1 mm, 2 mm and 3 mm; are displayed in figure 5.14. No meaningful variation in transmission is observed as a result of these changes. This means that the propagating mode does not extend past

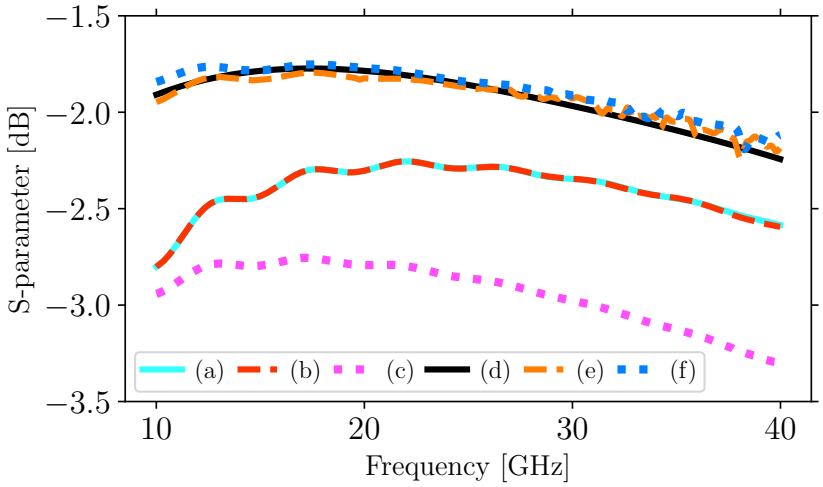

Figure 5.13: Simulated transmission (S21) through the six different model geometries laid out in figure 5.12. Curved track transmissions [(d), (e) and (f)] are very similar. Straight tracks (a) and (b) are almost identical and track (c) with the LO irregular via fence behaves somewhat worse, although it maintains relatively flat performance.

the via fence in the transverse direction in the plane of the substrate, and shows that the via fence is working as intended. As a result of these simulations, we ran the control tracks parallel to the RF and LO tracks with a 1 mm ground section between them.

5.11 Resulting printed circuit board

Following the process outlined in section 5.2, we designed a four-channel down-conversion PCB over two prototyping stages, all manufactured by Eurocircuits. The width of the resulting board is 51 mm, which sits asymmetrically behind each antenna, as the RF signals are launched side-by-side down the right hand half of the board. To convey why this width approaches the minimum width possible, for a four channel down-converter, using the ADMV1014, on a four layer PCB, a simultaneous view of all four copper layers is required. Figure 5.16 displays these copper layers to give an idea of the three dimensional complexity of the design. From left to right are the front RF signal copper, (a); the RF ground layer, (b), the power plane, (c) and the back miscellaneous layer, (d). The PCB is 183.2 mm in length, not including the protruding With-wave connectors, and just over 1 mm in thickness.

Most components are situated on the front layer of the downconverter, including the mixers, amplifiers, power dividers and connectors. After we roughly routed the RF, LO and IF signal paths, we compressed the components and tracks in the horizontal direction on the page, as much as was reasonable without significantly compromising signal integrity. We number the mixers from 0-3, with 0 being nearest the top of figure 5.16, closest to the With-wave connectors. Three competing bottlenecks to further reducing the board's width arose between each mixer and the next. Two pairs of LO and RF paths, a mixer and satellite components, the 4 V power rail and a set of IQ outputs must run parallel between ADMV0 and ADMV1. Between ADMV1 and ADMV2 the space

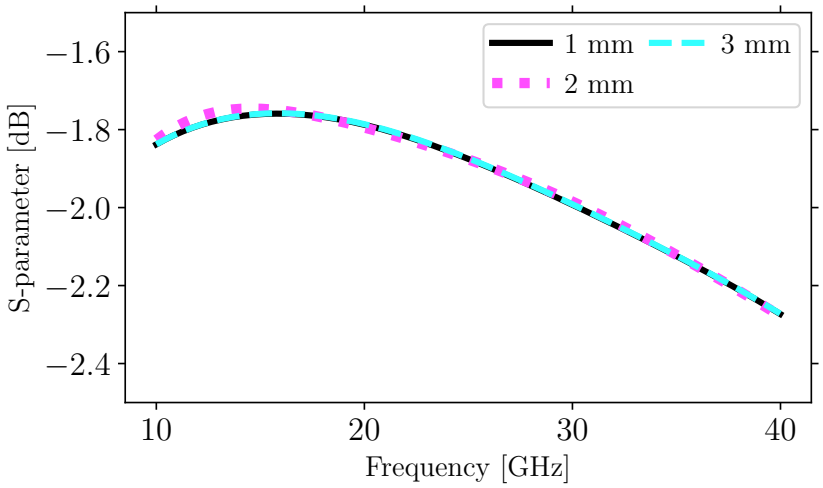

Figure 5.14: CST simulated transmission (S21) results for a 20 mm GCPW track with different widths of top ground plane to one side of the track. They are equivalent to the geometry in 5.12a, with the co-planar ground section nearer the bottom of the page truncated up to 1 mm, 2 mm or 3 mm from the edge near the GCPW track. We see a negligible change in transmission between the different cases. These simulations are set up in the same way as those described in figure 5.12.

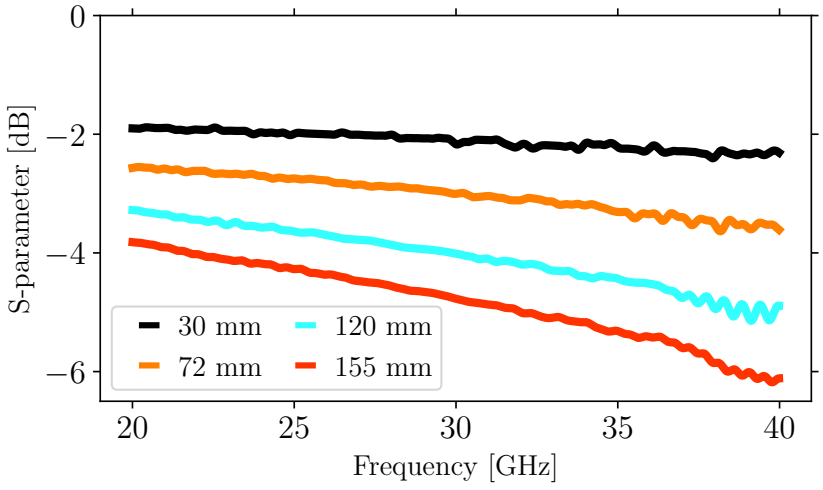

Figure 5.15: Simulated transmissions (S21) of four different lengths of GCPW line, approximately matching the RF track lengths to each mixer (shortest for channel 0, longest for channel 3). This shows that attenuation gradient versus frequency gets larger (in absolute terms) for longer tracks. These gradients are roughly linear.

opened up by one RF track leaving the throng is taken up by another set of IQ outputs and the LO connector and power divider. The third, between mixers 2 and 3, is probably the most competitive now that three IQ sets must pass alongside the second LO connector and power divider, the final RF track and final mixer.

Our optimal width target of 40 mm missed the real value by underestimating the space claimed by the differential IQ outputs, additional via fences and the power rail. Furthermore, additional width was required for the SPI lines to traverse the length of the board, as these were routed after the RF, LO, and IF and required more area than was left over. In spite of this underestimation, the final PCB is well compacted and already achieves some of the goals stated in section 2.3.2. We will make adjustments to the antenna array placement to account for the extra width. It has four-channels and IQ outputs. A separate low-pass filter module filters the downconverter's IF outputs to a 50 MHz bandwidth. Its cost of manufacture and assembly varies strongly with the order quantity, but even a single PCB costs under £1700, cheaper than one MMIQ-1040LS connectorised mixer (see Table 2.2).

5.12 Down-converter results

The down-converter prototypes were fed with single sideband output from the up-conversion module, described in section 5.13, and the LO signal, described in section 5.5.1. We initially checked the mixed-down IF outputs on an oscilloscope, before connecting them to the digitisation subsystem, as in the final diagnostic. We set the up-converter gain voltage to 0 V (minimum gain) and fed its output through a 20 dB attenuator, bringing the mean output power across the band to about −55 dBm. The HMC1040 amplifiers provide around 20 dB of gain, so the power entering the ADMV1014s will be between −30-−40 dBm. This is well below the P1dB compression point of the ADMV1014, at −10 dBm, and it is a similar input power to that used in the experiments described in the ADMV1014 datasheet, not including other losses. Sources of other loss on the board include RF track losses, the RF power divider (at least 3 dB), loss in the With Wave connector (see section 5.4.3), IF track and connector losses.

We measured the conversion gains of all four mixer channels over 20-40 GHz, using the experimental set up drawn in figure 5.17, and plotted them in figure 5.18. The ideal gain of the down-converter is shown by the grey circles, using the gains from the amplifier (HMC1040), power divider (EP2KA+) and mixer (ADMV1014) datasheets and ignoring any other losses. Single sideband RF input is received through a 20 dB attenuator from the up-converter module operating at a gain voltage of 0 V (minimum gain). The IF input frequencies transmitted to the two up-converter channels are 12.619 MHz and 17.837 MHz. We set the ADMV1014 output gain to maximum (which confusingly is achieved by setting the control pin to minimum voltage, 0 V). The down-converter output was processed by the digitisation and acquisition subsystems, giving IQ outputs in an arbitrary unit. To calibrate the measurement, a reference IF signal, at 19.123 MHz and 10.8 mV ± 0.1 mV peak-to-peak, from a signal generator was also measured by the digitisation and acquisition subsystems. We then scaled IF outputs from the down-converter to this known signal power. The uncertainty of the input signal's voltage results in a ±0.08 dB uncertainty in the IF power input to the up-converter. As we will see, this is several times lower than the standard deviation of multiple measurements of the down-converter conversion gain, therefore we will ignore it.

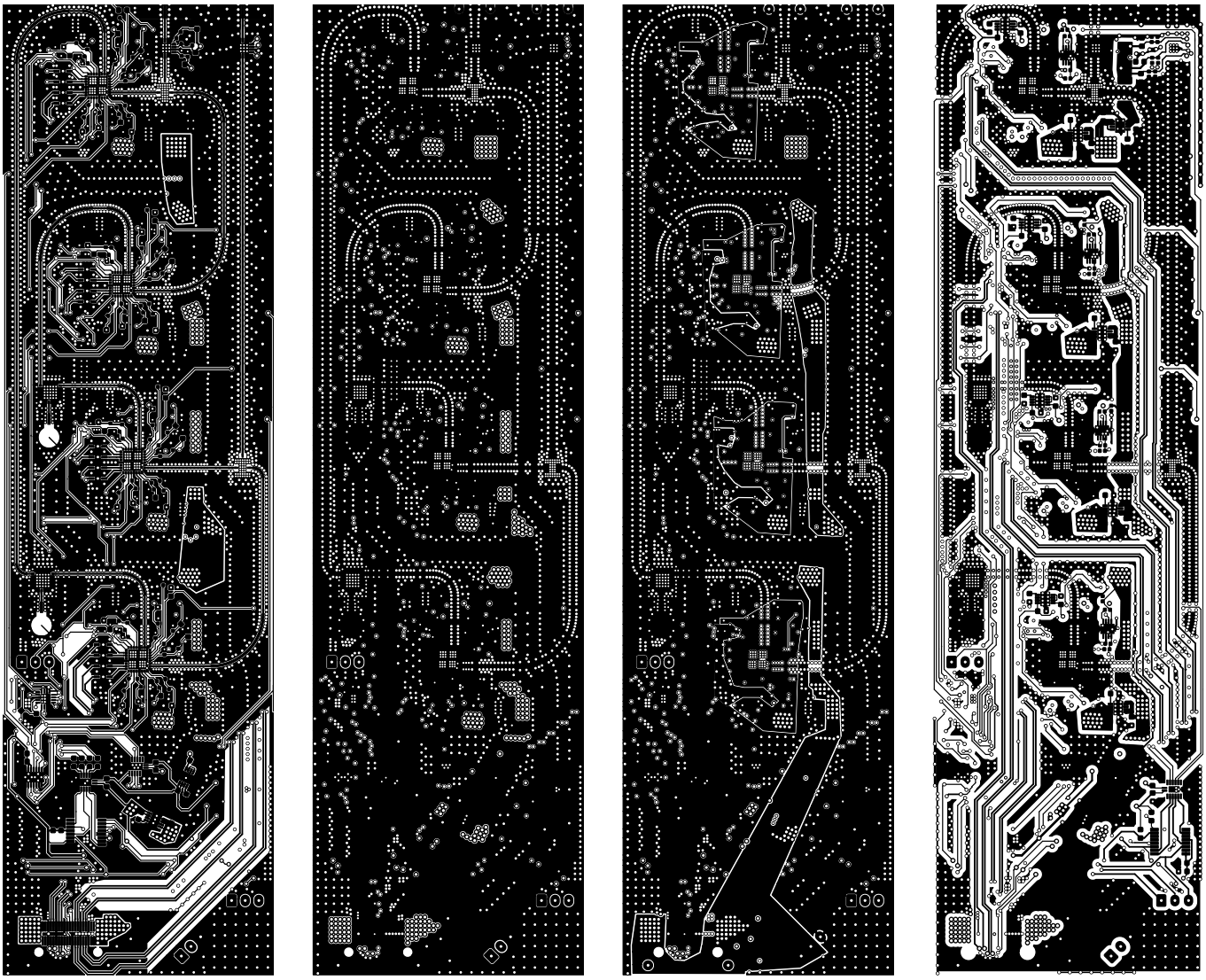

(a) Front - RF signal. (b) Internal 1 - RF ground. (c) Internal 2 - power. (d) Back - other.

Figure 5.16: Copper layer artwork of the final down-conversion module. Black denotes copper on each layer. The RF signals arrive from the direction of the antenna from the top of the page. The mixers are located at the centre of the four replicated nebulous arrangements situated periodically down the board's length (front layer).

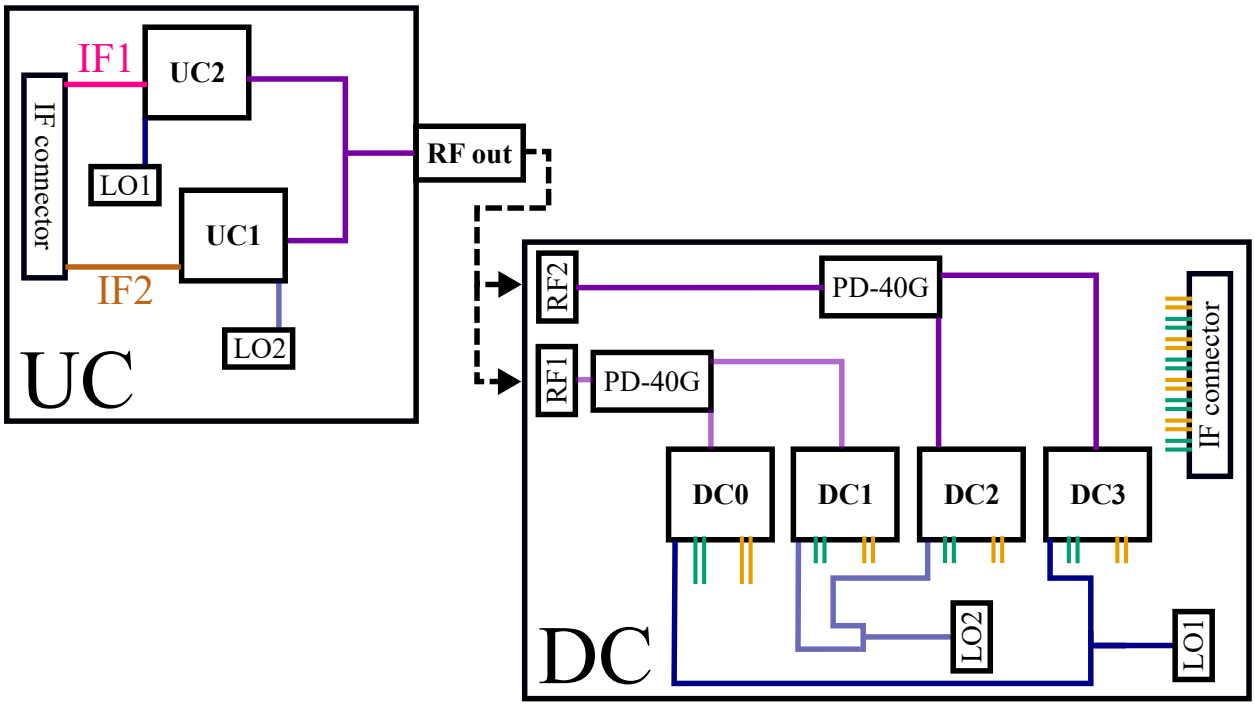

Figure 5.17: A block diagram of the down-converter conversion gain experimental set up. The two channels on the up-converter (UC) are supplied with different LOs and IFs signals, and the combined RF output is fed alternately into each down-converter (DC) input. The DC IF connector transmits the received IF signals to the digitisation subsystem, shown in figure 2.6.

A 26×26 grid of frequencies for the two LO channels was scanned, spanning 5-10 GHz in 0.2 GHz steps. Pairs of down-converter channels were measured independently, as further testing is required to measure all four simultaneously. Using a power divider, we were able to measure the up-converter output on a spectrum analyser at the same time as it was transmitted to one of the down-converter's RF inputs. We then used this measured up-converter output power to calculate the conversion gain of the down-converter channels. The labels "dc*" refer to the four ADMV1014s on the down-converter module, with dc0 being nearest the RF input. There is a rather large variation in conversion gain over the frequency range: of all four channels, the best gain is 40.2 dB and the worst is 11.8 dB. Generally, this means that SAMI-2 will have a much better signal-to-noise ratio at lower frequencies than higher frequencies. We expected this, as transmission line losses increase with frequency.

As the IF amplifier in the digitisation subsystem provides significant gain, we are confident SAMI-2 will be able to resolve signals (when installed on MAST-U) at frequencies where the down-converter has worse conversion gain. The largest error in the repeat measurements of all four channels is 3.6 dB (dc0 and dc1), while the largest for the other two channels is below 1.3 dB. Mean error for each channel is 0.7 dB or lower. This shows acceptable repeatability of the performance of all down-converter channels. The larger errors in channels dc0 and dc1 at 27.2 GHz are due to uncertainty in the measurement of the up-converter output power, used to calculated the conversion gain. The IF outputs from the down-converter have much lower uncertainties at this frequency.

As expected, the performance of dc3 is furthest from the ideal, with performance increasing with decreasing channel number (dc0 having best performance). This is because, as shown in

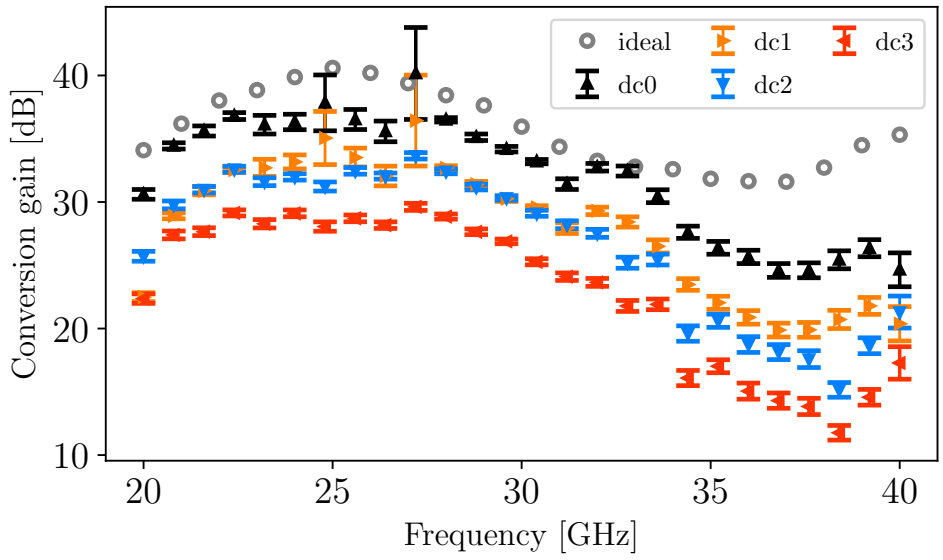

Figure 5.18: Down-converter gain over 20-40 GHz with 0.8 GHz spacing for all four channels, recorded separately in pairs (0 and 1, 2 and 3). ADMV1014 VCTRL gain voltage is set to 0 V (maximum gain) and LO input power from the LO supply is as described in section 5.5.1 and figure 5.10. RF input is from the up-converter module using IF frequencies 12.619 MHz and 17.837 MHz, with a power between −52.1-−64.6 dBm. The standard deviation from 26 repeat measurements at each frequency are included, the maximum being 3.4 dB (dc1). Grey circles show the ideal gain without losses, calculated using the amplifier, power divider and mixer datasheets.

figure 5.15, transmission line loss increases with increasing track length and dc3 is furthest from the RF connectors. Difference from the ideal gain increases with frequency, which we expected given that transmission line loss generally increases with frequency. At worst, we see an almost 20 dB difference to the ideal gain (dc3 at 38.4 GHz). Taking the worst transmissions in figure 5.15 to be −6 dB (GCPW loss) and figure 5.8 to be −3.8 dB (connector loss), we get a total loss of roughly 10 dB. This leaves an unexplained loss of another 10 dB, which is rather larger. However, if the *in situ* gains of the amplifiers, power dividers and mixers are, say, 1 dB or 2 dB lower than stated in their datasheets, this would reduce the observed discrepancy. The discrepancy is further reduced as the 155 mm simulation probably underestimates the transmission in figure 5.15 by over 2 dB at higher frequencies (given the difference between simulation and experiment in figure 5.8). There are likely to be other sources of loss, such as from manufacturing tolerances, substrate thickness and substrate permittivity variability, the inclusion of which will explain more of the difference between the ideal and measured gains. After considering track losses, connector losses and potential variability we conclude that, while not optimal, the conversion gains of all four down-converter channels are reasonable, when compared to the ideal gain, and very much large enough for use in SAMI-2.

Ideally, for simultaneous frequency performance the cross talk between channels at each frequency should be measured while all the mixer channels are active. Some changes are required to the experimental set up in order to measure the cross talk. We did not run these experiments in time for this thesis and so we leave cross talk measurements as further work. In experiments with

only two active channels, spurious signals recorded by the other channels were around 40 dB below the main signals, if any were observed at all.

In summary, we have designed and tested a four channel IQ down-converter PCB, which successfully operates over 20-40 GHz with a conversion gain of greater than 10 dB, as listed in the optimal module performance criteria (section 2.3.2). The IF bandwidth is set by the external IF filter module, which has a passband up to 50 MHz. Although its width (51 mm) exceeds the target width (40 mm) by some way, with hindsight this was unavoidable in order to satisfy the competing cost and deliverability constraints. We do not expect the larger width to greatly impact the antenna array placement. With more time, we would manufacture the RF transmission line to each mixer separately, with connectors on both ends, to try to narrow down the cause of the losses at higher frequency.

5.13 Up-converter printed circuit board design

In active-probing mode, SAMI-2 must illuminate the plasma with a broad microwave beam which backscatters from the plasma and is recorded by the receiving antennas in the array. We use two additional array elements as emitters for this purpose. This probing signal is in the form of a high frequency carrier, the LO, shifted by a much lower frequency offset, the IF. Measuring the Doppler shift of the IF with the receiving antennas and down-conversion mixers provides the information with which a 2D image of the plasma can be reconstructed. Generation of this probing signal can be achieved with essentially the reverse process used by the down-converter, described in section 5.1. Input LO and IF signals are mixed up, summed, to produce the output signal.

5.13.1 Up-converter specification

The SAMI-2 up-converter PCB subsystem must produce two simultaneous RF outputs to enable dual-frequency probing. Both these signals must illuminate the plasma in both horizontal and vertical polarisations to enable distinct measurement of the O- and X-mode cutoff surfaces. The output frequency range must match that of the down-converter as closely as possible, and provide sufficient output power to ensure an appropriate signal-to-noise ratio in the received backscattered signal.

In parallel with the ADMV1014 down-converter, Analog Devices produced the ADMV1013 up-converter integrated circuit which handily fulfils these specification criteria. It is available in a $6 \times 6\,\mathrm{mm}^2$ 40-pin package and has similar power and control requirements as the ADMV1014, making the design process very similar to the down-converter. The SAMI-2 up-converter does not necessarily need to be located directly behind the emitting antennas and therefore is not subject to stringent downward pressure on any of its dimensions, unlike the down-converter.

5.13.2 Final up-converter board

Many design choices for the up-converter were made previously for the down-converter, as we designed them in much the same way. Firstly, we arranged the two ADMV1013 chips, satellite resistors and decoupling capacitors. Secondly, we chose the orientation of RF (and corresponding power combiner), LO and IF I/O to the mixer, in that order. Thirdly, in the same order, the

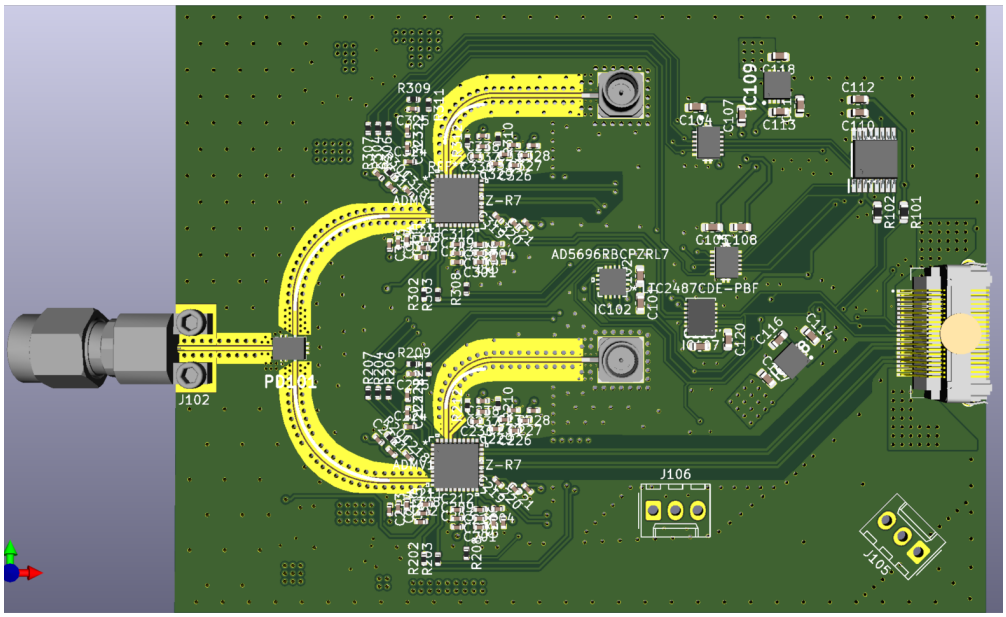

Figure 5.19: Top-down view of a 3D model of the final up-converter PCB.

signal tracks were laid to the same connectors used previously. For the GHz signals these included some curved right-angle bends (similar to those in figure 5.12d) in order to minimise any impedance discontinuities. No significant new effort was required for the IF connector, i2c control setup and power arrangements as they are all but identical to those of the down-converter. A 3D model of the final design is in figure 5.19, the RF outputs are combined by a Mini-circuits EP2KA+ chip and sent through the K-type With Wave connector on the left hand side. The LO inputs arrive through the two vertical SMP connectors in the middle of the board and the IF, control and power connections are fed through the high density, 40-pin LSHM connector on the right hand side.

5.13.3 Up-converter conversion gain

We measured the RF output power of the up-converter with the HP8564EC spectrum analyser, in steps of 400 MHz between 20-40 GHz. LO supply was as described in section 5.5.1, but here was fed through a 6 dB attenuator, to ensure the supply was always within the recommended −6-+6 dBm input range. We used IQ inputs of 6.1 MHz at −16 dBm power, and selected the lower sideband as the primary RF output signal. The experimental set up is similar to the block diagram in figure 5.17 with the down-converter removed and the up-converter output into the spectrum analyser. Figure 5.20 shows the gain of channel 1 versus output frequency, which is all greater than 10 dB. As with the down-converter, the gain decreases with increasing frequency. Again, this is to be expected, as losses are generally greater at higher frequency. Although we do not have comparable data for channel 2 at this time, we are highly confident that its conversion gain is very similar to that of channel 1.

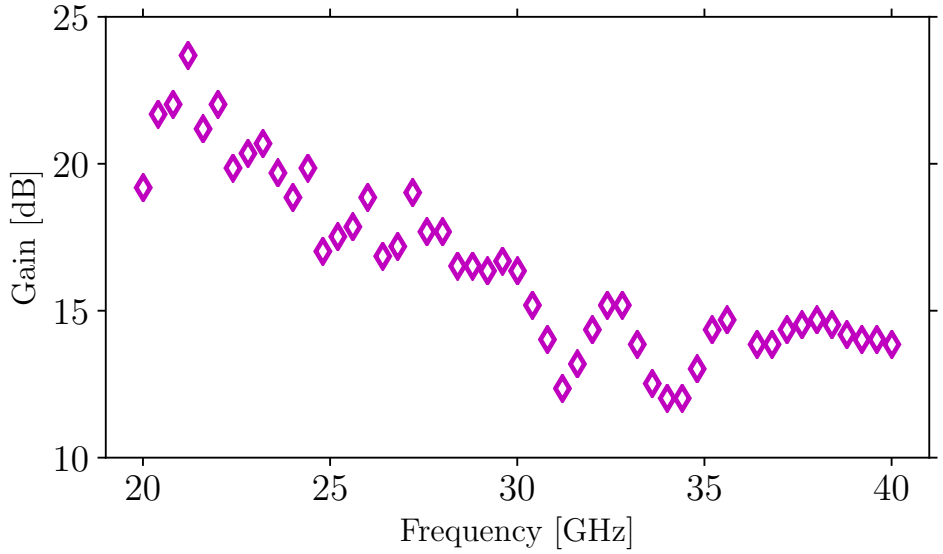

Figure 5.20: Up-converter channel-1 gain over 20-40 GHz with an IF input power of −16 dBm at 6.1 MHz, ADMV1013 VCTRL gain voltage set to 1.8 V (maximum) and LO input power from the LO supply, see section 5.5.1 and figure 5.10.

Chapter 6

Summary, conclusions and further work

The aim of this project was to design and build the microwave front end of a high quality 2D Doppler backscattering (DBS) tokamak diagnostic, to measure the edge current density on the the Mega-Ampere Spherical Tokamak Upgrade (MAST-U). We have successfully designed and tested the two main components of this front end system: antennas and mixer printed circuit boards (PCBs). First, we used knowledge of spherical tokamaks, edge plasma instabilities, the applications and behaviour of microwaves in magnetised plasmas, and phased arrays to draft specifications for the Synthetic Aperture Microwave Imager-2 (SAMI-2) diagnostic. Second, we applied techniques for antenna and microwave PCB design with associated simulation and experimental techniques, to fulfill those specifications.

We described the interrelations and trade offs between different aspects of the SAMI-2 diagnostic in chapter 2 and laid out its optimum specifications, with particular focus on the antennas and microwave circuitry, which make up the bulk of this thesis. Though the underlying motivation remains the same, SAMI-2 is a complete overhaul of the proof-of-principle diagnostic, the first SAMI. As a result, all of its subsystems were completely redesigned.

The sinuous antennas described in chapter 4 solve two inherent problems with the SAMI Vivaldi antennas: their lack of polarisation separation, which prevents separation of backscattered signal from the O- and X-mode cut offs, and their 3D structure, which causes internal reflections within a phased array. In addition, they nearly fulfill all of their other design criteria, operating over 20-40 GHz, with a $\pm 40^\circ$ field-of-view (as seen in figures 4.21 and 4.22), reproducible polarisation wobble and polarisation separation better than 10 dB over almost the whole frequency range (figure 4.18). However, our sinuous antennas have lower and more variable gain compared to the Vivaldis. Therefore, switching to sinuous antennas (as SAMI used Vivaldis) will increase the overall signal-to-noise ratio, and cause the variation in the signal-to-noise ratio to be larger over the frequency range. We have also shown that the performance of three sinuous antennas is repeatable to within acceptable uncertainties, in figure 4.9.

We have successfully designed and tested a four-channel down-conversion PCB, fulfilling all of its design criteria (described in section 2.3.2) save for the maximum width limit. This down-converter mixes gigahertz signals from the antennas with known local oscillator (LO) signals, producing intermediate frequency (IF) outputs in megahertz. Thirty of these circuit boards will be used in SAMI-2, one behind each receiving antenna in the array. Our selected mixer, the ADMV1014, operates over 20-40 GHz, has IQ outputs (essential for a phased array) and conveniently contains

an inbuilt LO quadrupler. The final down-converter we have designed has four channels per module, a total gain greater than 10 dB and a 320 MHz IF bandwidth (reduced to 50 MHz by the adjacent IF filter). Only by moving to a more costly eight-layer PCB would we have been able to produce a down-converter under the maximum width limit, while also satisfying the other criteria.

In addition to the down-converter, we have designed a two-channel up-converter PCB, effectively the reverse of the down-converter which produces radio frequency (RF) signals by mixing input LO and IF waves. Two up-converters will be used in SAMI-2, transmitting RF signals to the two emitting antennas which provide the active probing beams used in 2D DBS.

The up- and down-converter PCBs conversion gain tails off quite strongly towards the top end of the frequency range. We expect this is mainly due to increasing transmission line losses at higher frequency, but will not investigate further. Our two mixer PCBs work well enough for deployment on SAMI-2. This was our main goal at the outset, not necessarily to design and build optimum transmission lines and PCBs. We have lots of gain available in the digitisation subsystem, so will increase this to account for the falling down-converter gain.

6.1 Tokamak vessel integration

A reentrant port was installed on MAST-U in 2016 to give SAMI-2 a wider field-of-view (FOV) inside the machine. A scale drawing and model of the reentrant flange are shown in figure 6.1. Although the aperture in the 253 mm protruding flange is 200 mm, the window itself is 180 mm in diameter, as it is surrounded by a 10 mm rim. This flange is highlighted in pink in figure 2.3. Arcs of two poloidal field coils can be seen above and below the window: these would constrain SAMI-2's vertical view without the reentrant flange.

A CAD model of SAMI-2 bolted to the sector 5 midplane port is displayed in figure 6.2, the port flange is partially transparent. The diagnostic is mounted on sliding rails and is shown in its retracted position. The stationary mount is in light blue and is bolted to eight tapped holes surrounding the SAMI-2 port flange. The diagnostic weighs roughly 50 kg and the cuboidal frame measures $480 \times 480 \times 520\,\mathrm{mm}^3$. The RF front-end contained within the disc bulkheads will be about 25 mm long, and so their low frequency ends will protrude a short way from the mouth of the reentrant port. Some space is required between the frame and the front-end for the LO and IF cables. The LO cables have quite a small minimum bend radius (13 mm) however we will leave about 50 mm space between the frame and the first bulkhead, as at least 96 cables connect the two halves. Additional space may be added to ensure the array reaches the reentrant port window, depending how close the exoskeleton frame can get to the vessel.

6.2 Further work

Prior to deployment on MAST-U the SAMI-2 array response to a "point" source, will be tested in a laboratory setting. This will require the assembly of the rest of the digitisation and processing blades (ongoing), one of which is shown in figure 2.7. The full array of sinuous antennas may not work sufficiently well to provide the low noise image reconstructions we are aiming for. For example, in the available window diameter, it may not be possible to construct an array with the target sidelobe to main lobe power ratio of -15 dB over the whole frequency range. Additionally, we

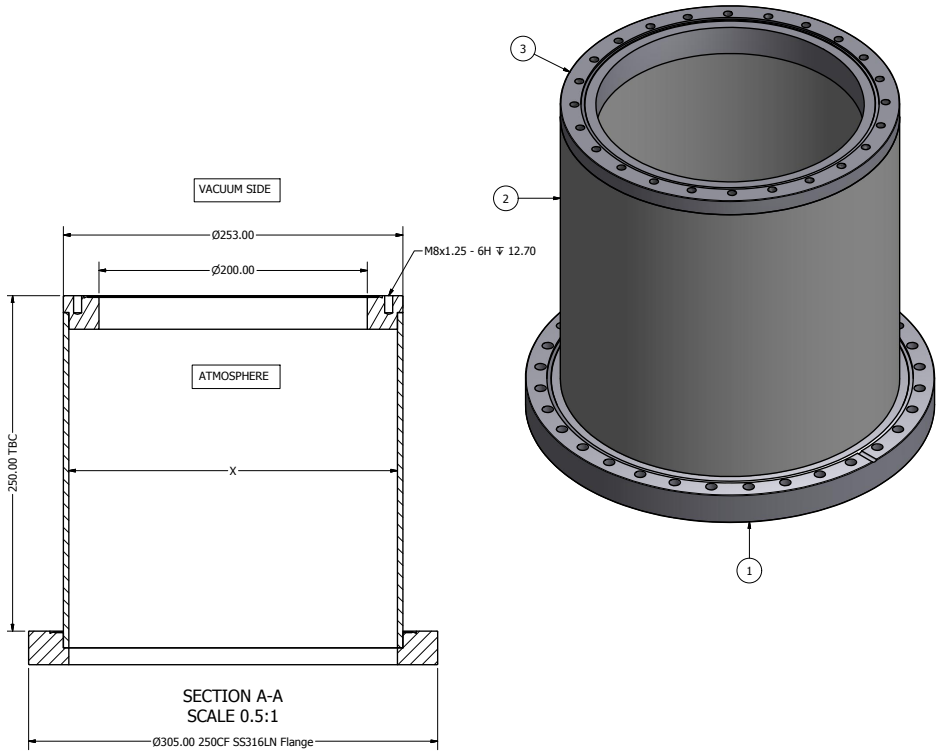

Figure 6.1: Scale drawing of SAMI-2's re-entrant midplane port on sector 5 of the MAST-U vessel, from the MAST-U Drawing Office.

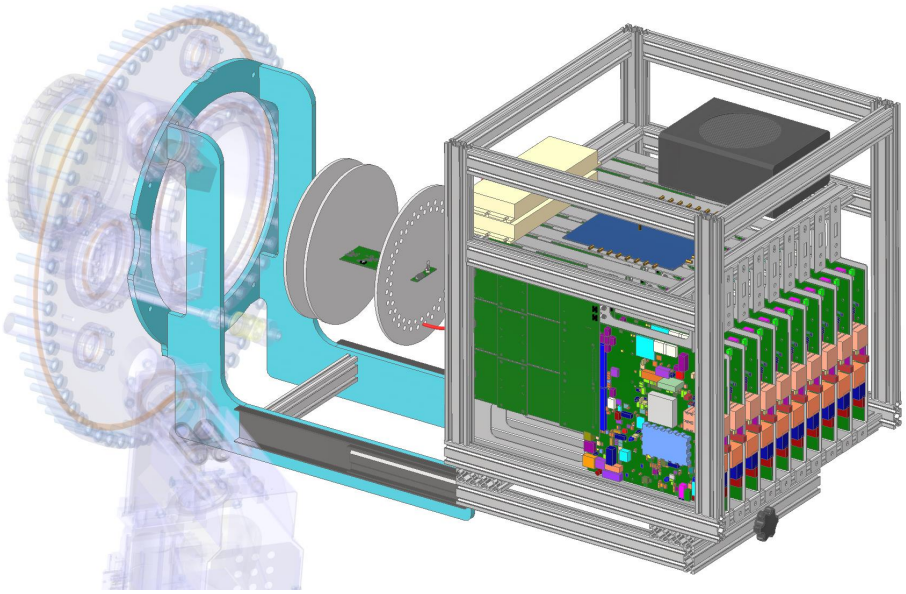

Figure 6.2: CAD model of the complete SAMI-2 frame attached to the sector 5 midplane port flange (partially transparent). The frame is in its extended position on the sliders. Three placeholder bulkheads (grey discs) to support the front end (downconverters and antenna array) are included, with one downconverter between them. Ten blades are stacked vertically in the bottom section of the frame. The frame's top section houses the LO power dividers (cream), the clocking module (blue) and the power supply (black).

know there will be some non-ideal inter-element interactions and it is not yet clear how significantly they will affect the noise threshold. If they are significant, the sinuous antennas can be redesigned (the isolated test of the balun may inform this) and meanwhile pairs of orthogonal Vivaldis may be used in the interim. Budget-wise, a new array of antennas is negligible.

When the diagnostic is complete it will be installed on the MAST-U vessel, on the midplane of sector 5 as shown in figure 6.2, and integrated with the experimental shot clock and data storage. An *in situ* calibration will be performed by beam forming reflected signal from the centre column and resolving its location. This will be carried out without plasma present in the tokamak.

After its installation, SAMI-2 will participate in the subsequent plasma shots. In the first instance, raw data from passive and active measurements will be sanity checked throughout the plasma lifetime. In doing so, the integrity of the four different frequency and polarisation channels will be assessed, in response to these passive and active signals. Following this, the data will be beam formed to produce 2D images of the plasma edge for the four channels. In doing so the integration window required for a smoothly varying signal will be ascertained. From these reconstructed images the SAMI Doppler shifted power analysis can be replicated to find magnetic pitch angle, a typical reconstructed image from SAMI is shown in figure 1.4. This will be performed for the four pairs of simultaneous active probing frequencies and antenna polarisations.

In the first instance SAMI-2 will measure the magnetic pitch angle at two simultaneous locations, corresponding to the two RF frequencies. If we are able to properly separate signals from the O- and X-mode cut offs, this may give us four independent radial pitch angle data points, however this may not be a straightforward measurement to make. It may be that if we are able to reliably launch a known mixture of O- and X-mode from the active elements, the polarisation separation will be easier. These multiple simultaneous pitch angle measurements will be compared to motional Stark effect (MSE) and EFIT. The quality of the match with different constraints on EFIT can be investigated: the SAMI-2-constrained EFIT can be compared to unconstrained and MSE-constrained EFIT.

SAMI-2's two frequency channels may be swept to build up a radial profile of the edge pitch angle. Doing so during a quiescent, stable part of the plasma shot then may give a full pitch angle profile, over the SAMI-2 radial view. Both active probing frequencies may be swept over 20-40 GHz as a pair and the backscattered signals radially correlated. Ampère's law may then be used to calculate the edge current density from the radial profile, as outlined in section 1.11.3. Following this calculation, a comparison can be made between the edge current density measured by the MAST-U MSE system and SAMI-2's measurement (we discuss the former MSE system on MAST [80] in section 1.11.4).

Passive acquisition mode will be used to measure a set of plasma shots, in addition to actively probing them as above. This data may be examined for emission from Bernstein mode conversion, with the view to localise the conversion location. The original SAMI was unable to resolve the backscattered emission well enough to measure $k_\perp$ spectra or specific turbulent velocities. SAMI-2's greatly enhanced relative resolution may enable it to measure these phenomena. Full-wave modelling of microwave propagation in plasmas is progressing at the University of York. The dual effort of experiment with simulation will be necessary to correctly interpret SAMI-2's passive measurements of mode converted emission, especially.

A key benefit of the modular approach we have taken in the SAMI-2 design is that it enables

relatively cheap upgrades and fault replacements. For instance, we may decide to alter the stopband of the IF filter, or to increase the sample rate of the analogue to digital converter (ADC). Alternatively a down-converter PCB may become faulty. As each stage in the signal path is fabricated on its own PCB, so it is simple and relatively inexpensive to make any of these changes. With a view to better understanding the sinuous antenna performance, the balun could be experimentally tested in isolation, using the end-to-end described in section 4.5.1 which has been fabricated. Finally, for completeness, the two-axis emission pattern of our Vivaldi antenna could be measured.

6.3 Final summary

The goal of this work was to design components which perform sufficiently well to enable the SAMI-2 diagnostic to work as intended, not necessarily to be optimised. Here we have applied antenna and microwave PCB design techniques to this end, rather than in and of themselves. In doing so, we have achieved nearly all of the original specifications for the SAMI-2 RF front end. We have shown that our dual-polarisation sinuous antennas almost completely fulfill their targets for their emission pattern, polarisation separation and polarisation wobble over 20-40 GHz. For the mixer modules, we have demonstrated that our four-channel in-phase and quadrature (IQ) down-converter has a width which is acceptably close to the target width, along with greater than 10 dB gain over the frequency range of the antennas.

Bibliography

[1] J.O. Allen, C.H. Vincent, and R.G.L. Vann. "Design of the Synthetic Aperture Microwave Imager Upgrade for measurement of the edge current density on MAST-U". Ed. by E. Poli, H. Laqua, and J. Oosterbeek. Vol. 203. EDP Sciences, 2019, p. 03004. DOI: 10.1051/epjconf/201920303004.

[2] J.O. Allen et al. "Dual-polarisation broadband sinuous antenna and microstrip power design for the Synthetic Aperture Microwave Imager-2 diagnostic". *Proceedings of the 14th International Reflectometry Workshop - IRW14* (Ecole Polytechnique Federale de Lausanne). Ed. by G.D. Conway (IPP Garching). Lausanne, Switzerland, 2019. URL: http://www.aug.ipp.mpg.de/IRW/IRW14/proceedings.html.

[3] *Fusion Technology 1996 Proceedings*. Elsevier, 1997. DOI: 10.1016/c2009-0-13289-0.

[4] M Keilhacker et al. "High fusion performance from deuterium-tritium plasmas in JET". *Nuclear Fusion* 39 (1999), pp. 209–234. DOI: 10.1088/0029-5515/39/2/306.

[5] ITER Organisation. *ITER Research Plan within the Staged Approach ITR-18-003*. Tech. rep. 2018.

[6] EUROfusion. *European Research Roadmap to the Realisation of Fusion Energy*. Tech. rep. 2018.

[7] CCFE. *Mast Upgrade Research Plan*. Tech. rep. 2019.

[8] Jeffrey P Freidberg. *Plasma Physics and Fusion Energy*. eng. Vol. 9780521851077. 2007. ISBN: 9780521851077.

[9] A Sykes et al. "High- performance of the START spherical tokamak". en. *Plasma Physics and Controlled Fusion* 39 (1997), B247–B260. ISSN: 0741-3335, 1361-6587. DOI: 10.1088/0741-3335/39/12B/019.

[10] United Kingdom Atomic Energy Authority. *The Spherical Tokamak for Energy Production*. Available at https://ccfe.ukaea.uk/research/step/ (2020-07-20).

[11] A. Sykes et al. "First results from MAST". *Nuclear Fusion* 41 (2001), pp. 1423–1433.

[12] F. Wagner et al. "Development of an Edge Transport Barrier at the H-Mode Transition of ASDEX". *Phys. Rev. Lett.* 53 (15 1984), pp. 1453–1456. DOI: 10.1103/PhysRevLett.53.1453.

[13] P A Schneider et al. "Differences in the H-mode pedestal width of temperature and density". en. *Plasma Physics and Controlled Fusion* 54 (2012), p. 105009. ISSN: 0741-3335, 1361-6587. DOI: 10.1088/0741-3335/54/10/105009.

[14] M Shimada et al. "Chapter 1: Overview and summary". en. *Nuclear Fusion* 47 (2007), S1–S17. ISSN: 0029-5515, 1741-4326. DOI: 10.1088/0029-5515/47/6/S01.

[15] F Wagner. "A quarter-century of H-mode studies". en. *Plasma Physics and Controlled Fusion* 49 (2007), B1–B33. ISSN: 0741-3335, 1361-6587. DOI: 10.1088/0741-3335/49/12B/S01.

[16] A. W. Leonard et al. "Influence of global beta, shape, and rotation on the H-mode pedestal structure in DIII-D". en. *Physics of Plasmas* 15 (2008), p. 056114. ISSN: 1070-664X, 1089-7674. DOI: 10.1063/1.2894214.

[17] H Zohm. "Edge localized modes (ELMs)". *Plasma Physics and Controlled Fusion* 38 (1996), pp. 105–128. DOI: 10.1088/0741-3335/38/2/001.

[18] A Loarte et al. "Characteristics of type I ELM energy and particle losses in existing devices and their extrapolation to ITER". *Plasma Physics and Controlled Fusion* 45 (2003), pp. 1549–1569. DOI: 10.1088/0741-3335/45/9/302.

[19] G Federici, A Loarte, and G Strohmayer. "Assessment of erosion of the ITER divertor targets during type I ELMs". *Plasma Physics and Controlled Fusion* 45 (2003), pp. 1523–1547. ISSN: 0741-3335. DOI: 10.1088/0741-3335/45/9/301.

[20] P. B. Snyder et al. "Edge localized modes and the pedestal: A model based on coupled peeling–ballooning modes". *Physics of Plasmas* 9 (2002), pp. 2037–2043. DOI: 10.1063/1.1449463.

[21] K J Gibson et al. "New physics capabilities from the upgraded Thomson scattering diagnostic on MAST". en. *Plasma Physics and Controlled Fusion* 52 (2010), p. 124041. ISSN: 0741-3335, 1361-6587. DOI: 10.1088/0741-3335/52/12/124041.

[22] H. Arnichand et al. "New capabilities of the incoherent Thomson scattering diagnostics in the TCV tokamak: divertor and real-time measurements". en. *Journal of Instrumentation* 14 (2019), pp. C09013–C09013. ISSN: 1748-0221. DOI: 10.1088/1748-0221/14/09/C09013.

[23] L. Frassinetti et al. "Spatial resolution of the JET Thomson scattering system". en. *Review of Scientific Instruments* 83 (2012), p. 013506. ISSN: 0034-6748, 1089-7623. DOI: 10.1063/1.3673467. URL: http://aip.scitation.org/doi/10.1063/1.3673467.

[24] J. Adamek et al. "Profile measurements of the electron temperature on the ASDEX Upgrade, COMPASS, and ISTTOK tokamak using Thomson scattering, triple, and ball-pen probes". en. *Review of Scientific Instruments* 87 (2016), p. 043510. ISSN: 0034-6748, 1089-7623. DOI: 10.1063/1.4945797.

[25] O. Sauter, C. Angioni, and Y. R. Lin-Liu. "Neoclassical conductivity and bootstrap current formulas for general axisymmetric equilibria and arbitrary collisionality regime". *Physics of Plasmas* 6 (1999), p. 2834. DOI: 10.1063/1.873240.

[26] H. Park et al. "Recent advancements in microwave imaging plasma diagnostics". *Review of Scientific Instruments* 74 (2003), pp. 4239–4262. DOI: 10.1063/1.1610781.

[27] J Stober et al. "Exploring fusion-reactor physics with high-power electron cyclotron resonance heating on ASDEX Upgrade". *Plasma Physics and Controlled Fusion* 62 (2020), p. 024012. DOI: 10.1088/1361-6587/ab512b.

[28] B A Hennen et al. "Real-time control of tearing modes using a line-of-sight electron cyclotron emission diagnostic". *Plasma Physics and Controlled Fusion* 52 (2010), p. 104006. DOI: 10.1088/0741-3335/52/10/104006.

[29] E Mazzucato. "Microwave reflectometry for magnetically confined plasmas". *Review of Scientific Instruments* 69 (1998), p. 18.

[30] F A Volpe. "Prospects for a dominantly microwave-diagnosed magnetically confined fusion reactor". en. *4th International Conference Frontiers in Diagnostics Technologies*. Frascati, Rome, Italy: Journal of Instrumentation, 2017, p. 20.

[31] R. Prater. "Heating and current drive by electron cyclotron waves". *Physics of Plasmas* 11 (2004), pp. 2349–2376. DOI: 10.1063/1.1690762.

[32] T.H. Stix. *The Theory of Plasma Waves*. McGraw-Hill, 1962.

[33] F. F. Chen. *Introduction to plasma physics*. New York: Plenum Press, 1974.

[34] K. Wiesemann. "A Short Introduction to Plasma Physics". *CAS-CERN Accelerator School: Ion Sources - Proceedings* (2014). DOI: 10.5170/CERN--2013--007.85.

[35] Heinrich Peter Laqua. "Electron Bernstein wave heating and diagnostic". en. *Plasma Physics and Controlled Fusion* 49 (2007), R1–R42. ISSN: 0741-3335, 1361-6587. DOI: 10.1088/0741-3335/49/4/R01.

[36] Ira B. Bernstein. "Waves in a Plasma in a Magnetic Field". *Phys. Rev.* 109 (1 1958), pp. 10–21. DOI: 10.1103/PhysRev.109.10.

[37] S J Zweben et al. "Edge turbulence measurements in toroidal fusion devices". en. *Plasma Physics and Controlled Fusion* 49 (2007), S1–S23. ISSN: 0741-3335, 1361-6587. DOI: 10.1088/0741-3335/49/7/S01.

[38] J W Conner and H R Wilson. "Survey of theories of anomalous transport". en. *Plasma Physics and Controlled Fusion* 36 (1994), pp. 719–795. ISSN: 0741-3335, 1361-6587. DOI: 10.1088/0741-3335/36/5/002.

[39] G D Conway. "Turbulence measurements in fusion plasmas". *Plasma Physics and Controlled Fusion* 50 (2008), p. 124026. DOI: 10.1088/0741-3335/50/12/124026.

[40] Robert H. Kraichnan. "Inertial Ranges in Two-Dimensional Turbulence". *Physics of Fluids* 10 (1967), pp. 1417–1423. DOI: 10.1063/1.1762301.

[41] L. Vermare et al. "Wavenumber spectrum of micro-turbulence in tokamak plasmas". en. *Comptes Rendus Physique* 12 (2011), pp. 115–122. ISSN: 16310705. DOI: 10.1016/j.crhy.2010.11.003.

[42] J.C. Hillesheim et al. "Doppler backscattering for spherical tokamaks and measurement of high- k density fluctuation wavenumber spectrum in MAST". en. *Nuclear Fusion* 55 (2015), p. 073024. ISSN: 0029-5515, 1741-4326. DOI: 10.1088/0029-5515/55/7/073024.

[43] A.R. Field et al. "Plasma rotation and transport in MAST spherical tokamak". *Nuclear Fusion* 51 (2011), p. 063006. DOI: 10.1088/0029-5515/51/6/063006.

[44] J Ruiz Ruiz et al. "Quantitative comparisons of electron-scale turbulence measurements in NSTX via synthetic diagnostics for high-k scattering". *Plasma Physics and Controlled Fusion* 62 (2020), p. 075001. DOI: 10.1088/1361-6587/ab82de.

[45] Pascale Hennequin. "Scaling laws of density fluctuations in tokamak plasmas". *Comptes Rendus Physique* 7 (2006), pp. 670–678. ISSN: 1631-0705. DOI: https://doi.org/10.1016/j.crhy.2006.08.001.

[46] Josef Preinhaelter et al. "Electron Bernstein wave-X–O mode conversion and electron cyclotron emission in MAST". en. *Review of Scientific Instruments* 74 (2003), pp. 1437–1440. ISSN: 0034-6748, 1089-7623. DOI: 10.1063/1.1530383.

[47] P. C. Efthimion et al. "New electron cyclotron emission diagnostic for measurement of temperature based upon the electron Bernstein wave". en. *Review of Scientific Instruments* 70 (1999), pp. 1018–1020. ISSN: 0034-6748, 1089-7623. DOI: 10.1063/1.1149464.

[48] J. Preinhaelter and V. Kopecký. "Penetration of high-frequency waves into a weakly inhomogeneous magnetized plasma at oblique incidence and their transformation to Bernstein modes". en. *Journal of Plasma Physics* 10 (1973), pp. 1–12. ISSN: 0022-3778, 1469-7807. DOI: 10.1017/S0022377800007649.

[49] A K Ram et al. "Heating and Current Drive by Electron Bernstein Waves in NSTX and MAST-Type Plasmas". en (2000), p. 4.

[50] Jakub Urban et al. "A survey of electron Bernstein wave heating and current drive potential for spherical tokamaks". en. *Nucl. Fusion* (2011), p. 16.

[51] V. Shevchenko et al. "Generation of Noninductive Current by Electron-Bernstein Waves on the COMPASS-D Tokamak". *Phys. Rev. Lett.* 89 (26 2002), p. 265005. DOI: 10.1103/PhysRevLett.89.265005.

[52] Josef Preinhaelter et al. "EBW power deposition and current drive in WEGA—comparison of simulation with experiment". *Plasma Physics and Controlled Fusion* 51 (2009), p. 125008. DOI: 10.1088/0741-3335/51/12/125008.

[53] Hiroshi IDEI et al. "ECW/EBW Heating and Current Drive Experiment Results and Prospects for CW Operation in QUEST". *Plasma and Fusion Research* 7 (2012), pp. 2402112–2402112. DOI: 10.1585/pfr.7.2402112.

[54] V.F. Shevchenko et al. "Electron Bernstein wave assisted plasma current start-up in MAST". *Nuclear Fusion* 50 (2010), p. 022004. DOI: 10.1088/0029-5515/50/2/022004.

[55] E Mazzucato. "Microwave imaging reflectometry for the visualization of turbulence in tokamaks". en. *Nuclear Fusion* 41 (2001), p. 12.

[56] C. M. Muscatello et al. "Technical overview of the millimeter-wave imaging reflectometer on the DIII-D tokamak (invited)". *Review of Scientific Instruments* 85 (2014), p. 11D702. DOI: 10.1063/1.4889735.

[57] W. Lee et al. "Microwave imaging reflectometry for density fluctuation measurement on KSTAR". *Nuclear Fusion* 54 (2014), p. 023012. DOI: 10.1088/0029-5515/54/2/023012.

[58] G D Conway et al. "Plasma rotation profile measurements using Doppler reflectometry". en. *Plasma Physics and Controlled Fusion* 46 (2004), pp. 951–970. ISSN: 0741-3335, 1361-6587. DOI: 10.1088/0741-3335/46/6/003.

[59] V. V. Bulanin et al. "Observation of geodesic acoustic modes in the Globus-M spherical Tokamak". *Technical Physics Letters* 40 (2014), pp. 375–377. DOI: 10.1134/S106378501405006X.

[60] A.Yu. Yashin et al. "Geodesic acoustic mode observations in the Globus-M spherical tokamak". *Nuclear Fusion* 54 (2014), p. 114015. ISSN: 0029-5515. DOI: 10.1088/0029-5515/54/11/114015.

[61] E Z Gusakov and A V Surkov. "Spatial and wavenumber resolution of Doppler reflectometry". *Plasma Physics and Controlled Fusion* 46 (2004), pp. 1143–1162. DOI: 10.1088/0741-3335/46/7/012.

[62] E Blanco, T Estrada, and J Sánchez. "Doppler reflectometry studies using a two-dimensional full-wave code". *Plasma Physics and Controlled Fusion* 48 (2006), pp. 699–714. DOI: 10.1088/0741-3335/48/5/014.

[63] Ernesto Mazzucato. *Electromagnetic Waves for Thermonuclear Fusion Research.* eng. 2014. ISBN: 9789814571814.

[64] Katsumi Ida. "Experimental studies of the physical mechanism determining the radial electric field and its radial structure in a toroidal plasma". *Plasma Physics and Controlled Fusion* 40 (1998), pp. 1429–1488. DOI: 10.1088/0741-3335/40/8/002.

[65] Glen Fields. "Phased Array Radar At the Intersection of Military and Commercial Innovation". *Microwave Journal* 57 (2014), pp. 2–3. ISSN: 01926225.

[66] P. E. Dewdney et al. "The Square Kilometre Array". *Proceedings of the IEEE* 97 (2009), pp. 1482–1496. ISSN: 0018-9219. DOI: 10.1109/JPROC.2009.2021005.

[67] O. M. Bucci et al. "On the Design of Phased Arrays for Medical Applications". *Proceedings of the IEEE* 104 (2016), pp. 633–648. DOI: 10.1109/JPROC.2015.2504266.

[68] R van der Linden and H J Visser. "Analysis, Design and Realization of a Near-Field Focused RF Power Transfer System". *Journal of Physics: Conference Series* 476 (2013), p. 012118. DOI: 10.1088/1742-6596/476/1/012118.

[69] J. Notaros et al. "Near-Field-Focusing Integrated Optical Phased Arrays". *Journal of Lightwave Technology* 36 (2018), pp. 5912–5920. DOI: 10.1109/JLT.2018.2880462.

[70] David A Thomas. "Phased array imaging of two dimensional Doppler microwave backscattering from spherical tokamak edge plasmas". PhD thesis. University of York, 2016.

[71] DA Thomas et al. "2D Doppler backscattering using synthetic aperture microwave imaging of MAST edge plasmas". *Nuclear fusion* 56 (2016), p. 026013. DOI: 10.1088/0029-5515/56/2/026013.

[72] SJ Freethy et al. "Lensless passive and active microwave imaging on MAST". *Plasma Physics and Controlled Fusion* 55 (2013), p. 124010.

[73] R. Scannell et al. "A 130 point Nd:YAG Thomson scattering diagnostic on MAST". *Review of Scientific Instruments* 81 (2010), p. 10D520. DOI: 10.1063/1.3460628.

[74] L.L. Lao et al. "Reconstruction of current profile parameters and plasma shapes in tokamaks". *Nuclear Fusion* 25 (1985), pp. 1611–1622. DOI: 10.1088/0029-5515/25/11/007.

[75] S. J. Freethy, V. F. Shevchenko, and R. G. L. Vann. "Optimization of Wide Field Interferometric Arrays via Simulated Annealing of a Beam Efficiency Function". *IEEE Transactions on Antennas and Propagation* 60 (2012), pp. 5442–5446. DOI: 10.1109/TAP.2012.2207936.

[76] R.G.L. Vann et al. "Preliminary measurements of the edge magnetic field pitch from 2-D Doppler backscattering in MAST and NSTX-U". *Review of Scientific Instruments* 87 (2016), p. 11D902.

[77] N. J. Conway et al. "The MAST motional Stark effect diagnostic". *Review of Scientific Instruments* 81 (2010). ISSN: 00346748. DOI: 10.1063/1.3494254.

[78] Simon Freethy. "Synthetic aperture imaging of BXO mode conversion". PhD thesis. University of York, 2012.

[79] K. J. Brunner et al. "Modifications to the synthetic aperture microwave imaging diagnostic". *Review of Scientific Instruments* 87 (2016), 11E129. ISSN: 0034-6748, 1089-7623. DOI: 10.1063/1.4961283.

[80] M F M De Bock et al. "Measurements of the edge current evolution and comparison with neoclassical calculations during MAST H-modes using motional Stark effect". *Plasma Physics and Controlled Fusion* 54 (2012), p. 025001. ISSN: 0741-3335. DOI: 10.1088/0741-3335/54/2/025001.

[81] D. M. Thomas, A. W. Leonard, and H. W. Mueller. "Calculation of edge toroidal current density distributions from DIII-D lithium beam measurements using Ampere's law". *Review of Scientific Instruments* 75 (2004), pp. 4109–4111. ISSN: 00346748. DOI: 10.1063/1.1787146.

[82] D. M. Thomas et al. "Measurement of edge currents in DIII-D and their implication for pedestal stability". *Physics of Plasmas* 12 (2005), pp. 1–9. ISSN: 1070664X. DOI: 10.1063/1.1879992.

[83] A Kirk et al. "Structure of ELMs in MAST and the implications for energy deposition". *Plasma Physics and Controlled Fusion* 47 (2005), pp. 315–333. DOI: 10.1088/0741-3335/47/2/008. URL: https://doi.org/10.1088/0741-3335/47/2/008.

[84] E. Viezzer, R. Dux, and M.G. Dunne. "A new beam emission polarimetry diagnostic for measuring the magnetic field line angle at the plasma edge of ASDEX Upgrade". *Review of Scientific Instruments* 87 (2016), 11E528. ISSN: 0034-6748. DOI: 10.1063/1.4959952.

[85] O Meneghini, M Choi, and F Volpe. "Full-wave feasibility study of magnetic diagnostic based on O-X mode conversion and oblique reflectometry imaging". *Review of Scientific Instruments* 87 (2016). ISSN: 15517616. DOI: 10.1063/1.4864604.

[86] Alberto Bottino et al. "Global Nonlinear Electromagnetic Simulations of Tokamak Turbulence". *IEEE Transactions on Plasma Science* 38 (2010), pp. 2129–2135. DOI: 10.1109/TPS.2010.2055583.

[87] A. R. Field et al. "Beam emission spectroscopy for density turbulence measurements on the MAST spherical tokamak". *Review of Scientific Instruments* 80 (2009), p. 073503. DOI: 10.1063/1.3170034.

[88] Charles H Vincent. "FPGA based diagnostics for the Mega-Amp Spherical Tokamak Upgrade". PhD thesis. Durham University, 2021.

[89] D.M. Pozar. *Microwave Engineering, 4th Edition*. Wiley, 2011. ISBN: 9781118213636. URL: https://books.google.co.uk/books?id=JegbAAAAQBAJ.

[90] SamacSys. *Component Search Engine*. URL: https://componentsearchengine.com/ (visited on 09/21/2020).

[91] *Gerber Format*. Ucamco. URL: https://www.ucamco.com/en/gerber.

[92] P. J. Gibson. "The Vivaldi Aerial". *1979 9th European Microwave Conference*. 1979, pp. 101–105. DOI: 10.1109/EUMA.1979.332681.

[93] J.D.S. Langley, P.S. Hall, and P. Newham. "Balanced antipodal Vivaldi antenna for wide bandwidth phased arrays". *IEE Proceedings - Microwaves, Antennas and Propagation* 143 (1996), p. 97. DOI: 10.1049/ip-map:19960260.

[94] Ehud Gazit. "Improved design of the Vivaldi antenna". *IEE Proceedings H Microwaves, Antennas and Propagation* 135 (1988), p. 89. DOI: 10.1049/ip-h-2.1988.0020.

[95] Jeremie Bourqui, Michal Okoniewski, and Elise C Fear. "Balanced Antipodal Vivaldi Antenna With Dielectric Director for Near-Field Microwave Imaging". en. *IEEE Transactions on Antennas and Propagation* 58 (2010), pp. 2318–2326. ISSN: 0018-926X, 1558-2221. DOI: 10.1109/TAP.2010.2048844.

[96] Alexandre M. De Oliveira et al. "A Palm Tree Antipodal Vivaldi Antenna With Exponential Slot Edge for Improved Radiation Pattern". en. *IEEE Antennas and Wireless Propagation Letters* 14 (2015), pp. 1334–1337. ISSN: 1536-1225, 1548-5757. DOI: 10.1109/LAWP.2015.2404875.

[97] Marek Dvorsky, Harihara S. Ganesh, and S. Sadhish Prabhu. "Design and Validation of an Antipodal Vivaldi Antenna with Additional Slots". en. *International Journal of Antennas and Propagation* 2019 (2019), pp. 1–10. ISSN: 1687-5869, 1687-5877. DOI: 10.1155/2019/7472186.

[98] Raymond H. DuHamel. "Dual polarised sinuous antennas". US patent 4658262A. 1987.

[99] K S Saini. "THE SINUOUS ANTENNA A DUAL POLARIZED ELEMENT FOR WIDEBAND PHASED ARRAY FEED APPLICATION". en (1996), p. 20.

[100] Prafulla Deo et al. "W-band planar antennas for next generation sub-millimeter focal plane arrays". en. SPIE ASTRONOMICAL TELESCOPES and INSTRUMENTATION, 2016, 99143P. DOI: 10.1117/12.2232496.

[101] R. P. Ortega, N. M. Christensen, and S. N. Tabet. "Cavity-Backed Dual-Sinuous Antenna Modeling". *2020 International Applied Computational Electromagnetics Society Symposium (ACES)*. 2020, pp. 1–2. DOI: 10.23919/ACES49320.2020.9196040.

[102] Jennifer M. Edwards et al. "Dual-Polarized Sinuous Antennas on Extended Hemispherical Silicon Lenses". en. *IEEE Transactions on Antennas and Propagation* 60 (2012), pp. 4082–4091. ISSN: 0018-926X, 1558-2221. DOI: 10.1109/TAP.2012.2207048.

[103] K. M. P. Aghdam, R. Faraji-Dana, and J. Rashed-Mohassel. "Compact dual-polarisation planar log-periodic antennas with integrated feed circuit". English. *IEE Proceedings - Microwaves, Antennas and Propagation* 152 (2005), 359–366(7). ISSN: 1350-2417.

[104] Ph. Gonnet et al. "Feeding networks for sinuous antennas". *Microwave and Optical Technology Letters* 20 (1999), pp. 195–200. DOI: 10.1002/(SICI)1098-2760(19990205)20:3<195::AID-MOP15>3.0.CO;2-C.

[105] J Edwards R O'Brient. "Sinuous antennas for cosmic microwave background polarimetry". Vol. 7020. SPIE Astronomical Telescopes + Instrumentation 2008, 2008. DOI: 10.1117/12.788526.

[106] Amir Jafargholi and Manouchehr Kamyab. "A new approach for feeding sinuous antenna". en. *AEU - International Journal of Electronics and Communications* 65 (2011), pp. 312–319. ISSN: 14348411. DOI: 10.1016/j.aeue.2010.03.010.

[107] D A Crocker. "Numerical and experimental evaluation of sinuous antennas for remote sensing applications". PhD thesis. Georgia Institute of Technology, 2019.

[108] Yasuto Mushiake. *Impedance Relationships for Complementary Planar Structures*. eng. 1996. ISBN: 978-1-4471-1255-6.

[109] Victor H Rumsey. *Frequency Independent Antennas*. eng. 1966. ISBN: 978-1-4832-2969-0.

[110] S.A. Maas. *The RF and Microwave Circuit Design Cookbook*. Artech House Mobile Communicat. Artech House, 1998. ISBN: 9780890069738. URL: https://books.google.co.uk/books?id=crJgQgAACAAJ.

[111] R. W. Klopfenstein. "A Transmission Line Taper of Improved Design". *Proceedings of the IRE* 44 (1956), pp. 31–35.

[112] Jiri Svacina. "New method for analysis of microstrip with finite-width ground plane". en. *Microwave and Optical Technology Letters* 48 (2006), pp. 396–399. ISSN: 0895-2477, 1098-2760. DOI: 10.1002/mop.21361.

[113] G Dash. *How RF Anechoic Chambers Work*. Tech. rep. Ampyx LLC, 1999. URL: http://www.glendash.com/Dash%5C_of%5C_EMC/Anechoic%5C_Chambers/Anechoic%5C_Chambers.pdf.

[114] John B Schneider. *Understanding the Finite-Difference Time-Domain Method*. eng. 2020. URL: https://eecs.wsu.edu/~schneidj/ufdtd/.

[115] Kane Yee. "Numerical solution of initial boundary value problems involving maxwell's equations in isotropic media". en. *IEEE Transactions on Antennas and Propagation* 14 (1966), pp. 302–307. ISSN: 0018-926X. DOI: 10.1109/TAP.1966.1138693.

[116] *CST Studio Suite*. Dassault Systèmes. URL: https://www.3ds.com/products-services/simulia/products/cst-studio-suite/.

[117] M. VAHDANI and X. BEGAUD. "Sinuous antenna fed by a microstrip to CPS balun". *2009 3rd European Conference on Antennas and Propagation*. 2009, pp. 1622–1626.

[118] *End Launch 2.92 mm Narrow Block Connector Datasheet*. NE03 Series. Rev. 2. With Wave. 2020. URL: https://6c6ad001-2899-452f-b6ad-d96838fae489.filesusr.com/ugd/39c61f_2b9ba7f5f8234f03b3608736e6f0f937.pdf.

[119] *I2C-bus specification and user manual*. UM10204. Rev. 6. NXP. 2014. URL: https://www.nxp.com/docs/en/user-guide/UM10204.pdf.

[120] Microwaves101. *Microwave Rules of Thumb*. URL: https://www.microwaves101.com/encyclopedias/microwave-rules-of-thumb (visited on 09/24/2020).

List of Abbreviations

ADC analogue to digital converter

DAC digital to analogue converter

DBS Doppler backscattering

DUT device under test

EBW electron Bernstein wave

ECE electron cyclotron emission

ELM edge-localised mode

EM electromagnetic

FDTD finite-difference time-domain

FOV field-of-view

FPGA Field-Programmable Gate Array

GCPW grounded co-planar waveguide

H&CD heating and current drive

IC integrated circuit

IF intermediate frequency

IQ in-phase and quadrature

LNA low noise amplifier

LO local oscillator

MAST the Mega-Ampere Spherical Tokamak

MAST-U the Mega-Ampere Spherical Tokamak Upgrade

MSE motional Stark effect

NSTX-U the National Spherical Torus eXperiment Upgrade

PCB printed circuit board

PS polarisation separation

RF radio frequency

SAMI Synthetic Aperture Microwave Imager

SAMI-2 Synthetic Aperture Microwave Imager-2

VNA Vector Network analyser